

Dissertation

submitted to the
Combined Faculties for the Natural Sciences and for Mathematics
of the
Ruperto-Carola University of Heidelberg, Germany
for the degree of
Doctor of Natural Sciences

Put forward by
Dipl.-Phys. Henry Lauro Lopez Carrera
born in Quito, Ecuador

Date of oral examination: July 25th, 2018

Sympathetic cooling and rotational quenching
of molecular anions in a hybrid atom ion trap

Referees: Prof. Dr. Matthias Weidemüller
Apl. Prof. Dr. Andreas Wolf

Abstract

This dissertation reports sympathetic cooling of the molecular hydroxyl anion (OH^-) via collisions with ultra cold rubidium (Rb) atoms. The anion's translational and rotational degrees of freedom were cooled simultaneously. A new-generation hybrid atom-ion trap (HAITrap) has been set up, combining an octupole radio frequency (rf) trap for ion storage and a dark-spontaneous force optical trap (darkSPOT) for Rb atoms. While the octupole rf-trap provides a large rf-field-free region decreasing rf-induced collisional heating, the darkSPOT reinforces this effect by locating the atom cloud in the center of the ion trap. The darkSPOT also enables to generate large dark state fractions, suppressing associative detachment and thus ion losses. Evidence on translational sympathetic cooling in the HAITrap was provided using two methods of kinetic thermometry: photodetachment tomography (PD) and measurements of the time of flight (ToF) distribution. The ToF analysis has shown to be more conclusive and numerical simulations validated the experimental findings qualitatively. Based on a one dimensional ToF-temperature mapping, the narrowest measured energy spread would correspond to a temperature of 35 ± 5 K. Deviations from thermal distributions were observed, as predicted from a theoretical model developed by our group. Rotational sympathetic cooling was observed via state selective photodetachment (SSPD). This was performed by pre-cooling the atoms with helium buffer gas at 295 K and further cooling the ions with Rb at $300 \mu\text{K}$. SSPD thermometry yielded a 70% decrease of the anions rotational temperature after interaction with Rb. These experimental findings could have direct applications in cold collision studies, quantum control of chemical reactions or sympathetic cooling of anti-protons.

Zusammenfassung

Diese Dissertation berichtet über sympathische Abkühlung des molekularen Hydroxyl-Anions (OH^-) durch Stöße mit ultrakalten Rubidium (Rb) Atomen. Die Translations- und Rotationsfreiheitsgrade des Anions wurden dabei gleichzeitig gekühlt. Eine hybride Atom-Ionenfalle (HAITrap) wurde aufgebaut, die eine Oktupol-Radiofrequenzfalle für die Ionenspeicherung und eine dunkle magneto-optische Falle (darkSPOT) für Rb-Atome kombiniert. Während die Oktupol-RF-Falle eine große RF-Feld-freie Region bereitstellt, die RF-induzierte Kollisionheizung verringert, verstärkt die DarkSPOT diesen Effekt, indem die Atomwolke in der Mitte der Ionenfalle lokalisiert wird. In der darkSPOT können eine große Anzahl der Atome in der Dunkelzustand präpariert werden, wodurch assoziative Reaktionen und damit Ionenverluste unterdrückt werden. Experimentelle Hinweise über translatorische sympathische Kühlung in der HAITrap wurden mit zwei Methoden der kinetischen Thermometrie geliefert: Photodetachment Tomographie (PD) und Messungen der Flugzeitverteilung (ToF). Die ToF-Analyse hat sich als schlüssiger erwiesen und numerische Simulationen validierten die experimentellen Ergebnisse auf qualitative Art und Weise. Basierend auf einer eindimensionalen ToF-Temperatur-Abbildung würde die engste gemessene Energieverteilung einer Temperatur von 35 ± 5 K entsprechen. Abweichungen von thermischen Verteilungen wurden beobachtet, wie aus einem von unserer Gruppe entwickelten theoretischen Modell vorhergesagt wurde. Sympathetische Rotationskühlung wurde mittels zustandsselektiver Photodetachment (SSPD) beobachtet. Dies erfolgte durch Vorkühlung der Atome mit Helium-Puffergas bei 295 K und weitere Abkühlung der Ionen mit Rb bei $300 \mu\text{K}$. SSPD-Thermometrie ergab eine Abnahme der Rotationstemperatur von 70% aufgrund inelastischer Kollisionen mit dem ultrakalten Puffergas. Diese experimentellen Ergebnisse könnten direkte Anwendungen in Kalkollisionsuntersuchungen, der Quantenkontrolle von chemischen Reaktionen oder der sympathischen Abkühlung von Antiprotonen haben.

Contents

1	Introduction	1
2	Hybrid Atom-Ion Trap (HAITrap)	6
2.1	Ions	9
2.1.1	Fundamentals: from Paul to multipole rf traps	9
2.1.2	Ion source	14
2.1.3	Thin wire octupole ion trap	18
2.1.4	Characterization of the ion trap	23
2.2	Atoms	28
2.2.1	Fundamentals: From optical molasses to a darkSPOT	28
2.2.2	darkSPOT setup	29
2.2.3	Atom cloud characterization	31
3	Sympathetic cooling of anions by ultra-cold atoms	39
3.1	Neutral-ion collisions inside a hybrid trap	40
3.1.1	Reactive collisions	42
3.1.2	Elastic atom-ion collision dynamics	46
3.1.3	Final energy distributions	51
3.2	Thermometry via photodetachment tomography	56
3.2.1	Ion density simulations	56
3.2.2	Ion cloud imaging via PD tomography	59
3.2.3	Experimental evidence of sympathetic cooling	65
3.3	Thermometry via Time of Flight	68
3.3.1	Trajectory simulations	68
3.3.2	Experimental demonstration of sympathetic cooling	77
3.3.3	Emergence of non-thermal distributions	83
4	Rotational quenching of molecular anions by ultra cold atoms	88
4.1	Internal structure of OH^-	91
4.1.1	Rotational structure of OH^- and OH	93
4.1.2	OH^- photodetachment spectrum	96
4.1.3	Interaction of OH^- with black-body radiation	100
4.2	Rotational thermometry via state selective photodetachment	105
4.2.1	State selective photodetachment	105
4.2.2	Room-temperature buffer gas: $\text{OH}^- + \text{He}$	111
4.2.3	Ultra cold buffer gas: $\text{OH}^- + \text{Rb}$	114
5	Conclusion and Outlook	117
5.1	Conclusion	117

Contents

5.2 Outlook	121
A Bibliography	124
Acknowledgments	137

1 Introduction

Cooling of particles has been of great importance in fundamental physical research since decades. Within this vast field of atomic and molecular physics, the study of collisional processes below 1 K is of particular interest because the particles' wave nature defines the collision dynamics: the de-Broglie-wavelength becomes comparable to the classical impact parameter, leading for instance to non-classical stochastic reaction effects [1, 2]. However, studies on *atom-ion* interactions in this temperature regime have become experimentally accessible only recently [3, 4].

In order to perform experiments in this temperature regime, the development of ion and atom traps as well as of innovative cooling techniques has been crucial. The 'workhorse' method for cooling matter in gas phase has been laser cooling, which allows atoms, molecules and positive ions to be successfully brought to temperatures near the absolute zero, the so called ultra cold regime [5, 6]. Additionally, ions can be stored in radio frequency (rf) traps independently of their specific internal structure, offering extensive experimental advantages and applications [7, 3].

Though laser cooling also the preparation of ro-vibrational cold molecular ions confined in a Paul trap [8], this technique cannot be applied to every particle because a closed optical cycle is needed. This often requires the use of many laser wavelengths, leading to very complicated laser cooling schemes and systems [9]. Consequently, alternative methods have been developed in order to cool ions and other particles where laser cooling is not possible.

One of this methods is sympathetic cooling. It is based on using a cold sample of particles as buffer gas to cool particles of another type. A typical gas used for sympathetic cooling is cryogenic Helium due to its chemical neutrality and its high gas density at a few Kelvin [7]. By cooling stored ions via collisions with such a cold buffer gas, the ions internal and external degrees of freedom can be cooled down simultaneously [10]. However, there are two main limitations of this technique: i) the relatively high temperature of the buffer gas and ii) in the case of ionic systems, a further heating effect of ions in radio frequency traps called rf-collision induced heating. This effect is linked to the ions intrinsic motion inside a rf trap and how it is affected by atom-ion collisions. For achieving lower temperatures, colder gases are required. For example, laser cooled ions can be used to sympathetically cool a vast variety of other atomic or molecular ions. However, due to the long-range Coulomb interaction, the internal degrees of freedom of the molecular ions are not cooled down.

In order to overcome these limitations, the advantages from both trapping and cooling methods can be combined: laser cooling can provide atoms at ultra low temperatures, which can be used as an ultracold buffer gas to cool ions stored

1 Introduction

in rf-traps. The idea of cooling ions in this way goes back to Gerlich in 1995 when he reported results on a cryogenic rf trap system. In his words: "...an interesting aspect of collisional relaxation of stored ions is to use a cloud of laser cooled atoms (sympathetic cooling) as buffer gas. This effect becomes especially efficient if the atom cloud is localized in the central part of the ion trap, i.e. in the near field-free region." [7]

The use of an ion trap overlapped with an atom trap has been called in the literature a hybrid trap [11]. These systems offer an outstanding tool to study different atom-ion collision processes, and have therefore triggered an increasing number of experimental proposals [12], theoretical works [13], computer simulations [14] and experimental realizations [15, 16]. Further applications and prospects of hybrid trap systems can be found in the review articles [17, 18, 19].

In order to investigate the prospects for sympathetic cooling in hybrid traps, theoretical studies on atom-ion elastic collision dynamics has been of special interest. These studies found that, due to collisional induced rf heating, the atom-ion mass ratio m_a/m_I sets a natural limit for sympathetic cooling in ion traps, which was estimated to be $m_a/m_I \approx 1$ [14, 20, 21, 22, 23]. However, our group has theoretically shown that this limit can be overcome using a localized buffer gas and a multipole ion trap [24, 25].

The first experimental realization of an atom-ion hybrid trap appears in 2005 [26], where it was shown that both technologies can be combined without major influences on the atom cloud. About 5 years later, first experimental evidence of translational sympathetic cooling in a hybrid trap was reported for a single $^{174}\text{Yb}^+$ ion immersed in a Rb BEC [27]. Successively, various systems have provided experimental information on sympathetic cooling of the translational energy of ions in a hybrid trap: $\text{Na}^+ + \text{Na}$ [28], $\text{Rb} + \text{Rb}^+$ [29], $^{39}\text{K}^+ + ^{85}\text{Rb}$ and $^{85}\text{Rb}^+ + ^{133}\text{Cs}$ [30], $\text{Ca}^+ + \text{Li}$ [31].

Despite the huge technological and conceptional advances in cold physics over many decades, *negative ions* (anions) remain till date experimentally unexplored in the cold and ultra cold regime. The cooling of such particles into the ultra cold regime could trigger a similar impact as was the case for atoms, molecules or cations. In astrophysics for example, anions play a bigger role in interstellar medium than it was thought a few years ago [32, 33]. Furthermore, for atomic and molecular physics, the creation of an ultra-cold anion sample would allow to sympathetically cool any other anion species. This is of special interest in antimatter physics, where a cold anion cloud is still needed in order to sympathetically cool anti-protons, which can be later used for efficient production of anti-hydrogen [34].

In order to create ultra-cold anion samples, researchers have proposed laser cooling schemes for different anionic species [35, 36, 37]. Yet, the experimental realization of such proposed schemes is to date still missing. Other methods, for instance cryogenic storage rings [38, 39], electron cooling [40], supersonic expansion beams [41, 32] or buffer gas cooling in cryogenic ion traps [7, 42], have allowed the study of anions at effective temperatures of a few kelvin.

To extend the existing tools for the preparation of cold anion samples, a

1 Introduction

new generation hybrid trap has been built during the course of this doctoral work. This hybrid Atom-Ion Trap (HAITrap) has been developed within the scope of an international collaboration between the research groups of Prof. Matthias Weidemüller at the University of Heidelberg, Germany, and Prof. Roland Wester at the University of Innsbruck, Austria, and has benefited from the experience of former experiments realized within this collaboration [15].

The HAITrap combines an octupole rf trap for ions with a magneto optical trap (MOT) for rubidium atoms. The use of an octupole trap was preferred due to the large rf-free-field region, which attenuates the effects of rf-induced collisional heating. The rf electrodes are made of thin wires, allowing optical access to the trap's center. In this way the lasers, needed to cool the atoms and to probe the ions, have enough space to access the trap's inner region. The rf trap was set up in the group of Prof. Roland Wester and has been already used for other experiments [43, 44]. To laser cool the rubidium atoms, a special design of a MOT was used, the so called dark spontaneous-force optical trap (darkSPOT) [45]. The darkSPOT offers three main experimental advantages for sympathetic cooling: i) it allows to prepare atom clouds at higher atom densities in comparison with a standard MOT, thus increasing the atom-ion collision rates, ii) the internal state distribution of the atom cloud can be controlled, which allows the suppression of associative detachment in the system $\text{OH}^- + \text{Rb}$ and, iii) when located in the center of the ion trap, the small spatial spread of the atom cloud further suppresses rf-induced collisional heating.

Among many interesting molecular ions, the hydroxyl anion OH^- was chosen for this work. Besides playing a central role in organic, inorganic and atmospheric chemistry, OH^- has been since decades a well-established test system for studying fundamental questions in numerous publications [46, 47, 48, 49, 50, 51, 52, 53, 38, 39]. Therefore, there exists plenty of experimental data about this anion, facilitating the comparison of our results with these available references. Furthermore, its mass, charge, rotational structure and chemical open channels with rubidium are of particular interest for our experiment:

- *Charge.* The most trivial but a very important argument for choosing OH^- is that it is a negatively charged ion. As stated before, anions remain unstudied in the ultra cold regime and cooling this anion would serve as a bridge towards this direction.
- *Mass.* The system $\text{Rb} + \text{OH}^-$ has a mass ratio of $m_a/m_i = 85/17 = 5$. Cooling of OH^- with rubidium as a localized buffer gas would experimentally verify our theoretical predictions. Furthermore, it would be the highest atom-ion mass ratio reported to date for sympathetic cooling of ions stored in rf traps.
- *Chemical reactions with rubidium.* In the system $\text{OH}^- + \text{Rb}$, the chemical interactions depend critically on the internal state of the neutral partner. Atoms being in their electronic ground state have a chemical reaction cross section much lower than those in excited state. Therefore, by increasing

1 Introduction

the internal state population of the atom cloud, the rate of reactive collisions in our atom-ion system can be suppressed. In our hybrid trap this is achieved by controlling the dark state fraction of the atoms in the dark-SPOT. The highest dark state population achievable in our trap is $\approx 95\%$. As a consequence, in our hybrid trap elastic collisions rates exceed the ion loss rate due to chemical reactions. This makes OH^- a good candidate for being sympathetically cooled by Rb.

- *Rotational Structure.* The rotational structure of OH^- can be effectively modeled as a two-dimensional quantum rotor [38], therefore making it a well-established test system for studying experimental and theoretical questions. Additionally, its rotational detachment thresholds are easily accessible in the experiment due to its large rotational parameter [54]. Furthermore, theoretical calculations have shown that the system $\text{OH}^- + \text{Rb}$ is advantageous for sympathetic cooling of the anions' internal degrees of freedom, as it is expected to show large de-excitation rates [55, 56, 57].

This dissertation describes the experimental realization and demonstration of sympathetic cooling of OH^- along its translational and rotational degrees of freedom simultaneously, via collisions with an ultra-cold cloud of Rb atoms. Furthermore, it is shown that trapped samples of kinetically cold OH^- can be prepared in their rotational ground state.

This dissertation is organized as follows. The experimental setup of the HAITrap is described in chapter 2. The fundamental working principles, technical details and characterization of both ion and atom traps are presented in section 2.1 and 2.2 respectively.

The sympathetic cooling along motional degrees of freedom of OH^- is described in chapter 3. For this aim, the types of collisions that can take place in hybrid traps, namely reactive, elastic and/or inelastic collisions between ions and atoms, are described in section 3.1 with special scope on the system $\text{OH}^- + \text{Rb}$. Specifically, the characterization and experimental control of reactive collisions in this system are discussed in section 3.1.1. Afterwards the elastic collision dynamics of single ions with atoms inside a hybrid trap with different ion trap geometries and mass ratios is analyzed in section 3.1.2. Based on this, the expected final ion energy distributions for different ion trap geometries, mass ratios and specifically for our HAITrap are described in section 3.1.3.

In this work, two different motional thermometry techniques are described and compared them to each other. The first method, presented in section 3.2, is based on tomography measurements of the ion cloud using photodetachment of the anion's electron. The second method, presented in section 3.3, is based on precise measurements of the ion time of flight distributions.

The rotational quenching of OH^- via collisions with ultracold rubidium atoms is shown in chapter 4. For this aim, an overview on the ro-vibrational structure of OH^- is described in section 4.1. Specifically, a model for its rotational structure is presented in section 4.1.1. Here, the model introduced in [38] (supplemental material) is applied, which makes an excellent review on the models available

1 Introduction

in the literature. This model allows the prediction of anions' interaction with photons of energy near the photodetachment threshold (section 4.1.2) and the black body field in the experimental apparatus (section 4.1.3).

In section 4.2 evidence on sympathetic cooling of the anion's rotational degrees of freedom is reported. The method used for probing the rotational temperature of the ions is discussed in section 4.2.1. Based on this, thermometry measurements for ions that interacted with a buffer gas at room temperature are shown in section 4.2.2). The experimental results on rotational quenching of OH^- with rubidium as buffer gas are presented in section 4.2.3.

To conclude in chapter 5, the experimental observations reported in this dissertation are summarized in section 5.1 and future goals and perspectives of the experiment are discussed in section 5.2.

This dissertation is partially based on results which have been already published by our group [58, 24, 25, 59, 60]. Furthermore, relevant topics from bachelor and master theses advised during the course of this doctoral work are also included [61, 62, 63, 64, 65, 66, 67, 68]. The most recent outcomes of our experiment, which are the core of this work, are currently in preparation for publication.

2 Hybrid Atom-Ion Trap (HAITrap)

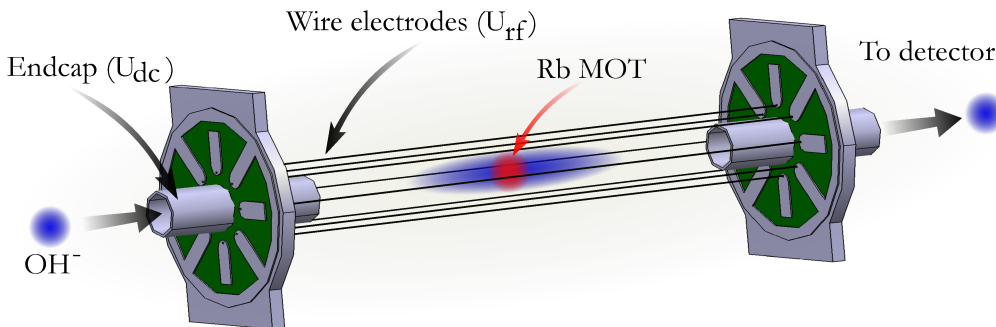


Figure 2.1: Schematics of the hybrid atom-ion trap (HAITrap). OH^- is created in a plasma-discharge ion source, mass selected via ToF and accelerated towards the ion trap. Once the ions pass through the hollow end-cap electrode, a potential U_{dc} is applied for axial confinement. For radial confinement an rf-voltage with amplitude U_{rf} is applied to the thin wire electrodes with neighboring opposite polarization. Once the ions are trapped, the Rb darkSPOT is loaded. After a variable interaction time, the ions are extracted and counted using a channeltron detector.

Hybrid atom-ion traps are an ideal tool for performing experiments on fundamental collision processes between atoms and ions. Theoretical discussions as well as experimental realizations, applications and prospects of these systems can be found in the review articles [17, 18, 19].

Our hybrid Atom-Ion Trap (HAITrap) is a unique system since, in contrast other experiments to date, it combines a multipole rf trap with a magneto optical trap. Furthermore it is able to overlap ions irrespective of their charge with the ultracold cloud of Rb atoms. As stated in the introduction, this setup was planned and constructed during the course of this doctoral work within the scope of an international collaboration between the research groups of Prof. Matthias Weidemüller in the University of Heidelberg, Germany, and Prof. Roland Wester the University of Innsbruck, Austria. This experiment has taken advantage from former experiments realized within this collaboration [15]. The rf trap itself was set up in the group of Roland Wester and has been already used for other experiments [43, 44], whereas the darkSPOT setup was developed in the group of Matthias Weidemüller [69]. During the course of this doctoral work, both traps were hybridized while considering the technicalities of both systems.

In this chapter, an overview of the most important components of the hybrid

2 Hybrid Atom-Ion Trap (HAITrap)

atom-ion trap (HAITrap) is presented. The experimental control and data acquisition in the experiment are computer controlled with a custom made LabView software, details of which can be found in [61]. This software allows automatized sequences of experimental cycles by simultaneously controlling several electronic devices needed for a specific measurement. The main electronic hardware for controlling this sequences are the so called Logic Boxes, which were developed in the electronic workshop from our Institute. These electronic devices are able to output timed sequences of digital and analog signals with a timing output resolution of 100 ns.

A schematic picture of our HAITrap with its main components is presented in figure 2.1, whereas a more detailed schematic description of the setup is depicted in figure 2.2. The HAITrap consist of three different vacuum chambers (atom source, ion source and science chamber) separated by differential pumping stages. The science chamber is kept at a pressure of 10^{-9} mbar using a turbo pump with pumping speed of 685l/s. It is connected with the ion source chamber via a differential pumping hole of 5 mm diameter. The ion source chamber must to be constantly pumped out since the ion source is seeded by a carrier gas for ion creation. This seed gas is pumped out by a further turbo pump of speed 70l/s, keeping the ion source chamber at a pressure of 10^{-7} mbar. The atom source (not depicted in the picture) is connected to the main chamber via a differential pumping hole of 0.8 mm diameter. This chamber is kept at a pressure of about 10^{-6} mbar and is not actively pumped out for an optimal use of the rubidium vapor.

The ion trapping system is presented in more detail in section 2.1. The fundamental principles of radio frequency trapping are discussed in section 2.1.1. In our setup, the OH^- ions are created in a plasma-discharge ion source (see figure 2.2), details of which are described in section 2.1.2. After they exit the source, the ions are mass selected via ToF. For optimizing the ion trap loading, a set of ion optics has been installed between the mass spectrometer and the ion trap. Once inside the trapping volume of the rf-trap, the ions can be stored for several minutes. Specific details of these components, with special focus on the octupole ion trap, are described in section 2.1.3. After a variable storage time, the ions are extracted and counted by a channeltron detector. A characterization of the ion storage and detection process is presented in section 2.1.4.

The setup for trapping rubidium atoms is presented in section 2.2. The fundamental principles of atom trapping via laser light and magnetic fields are presented in section 2.2.1. Specific details on the laser light preparation in our experiment as well as the atom source and optics design for our darkSPOT is presented in 2.2.2. To conclude, a characterization of the atom cloud inside the ion trap is presented in section 2.2.3.

2 Hybrid Atom-Ion Trap (HAITrap)

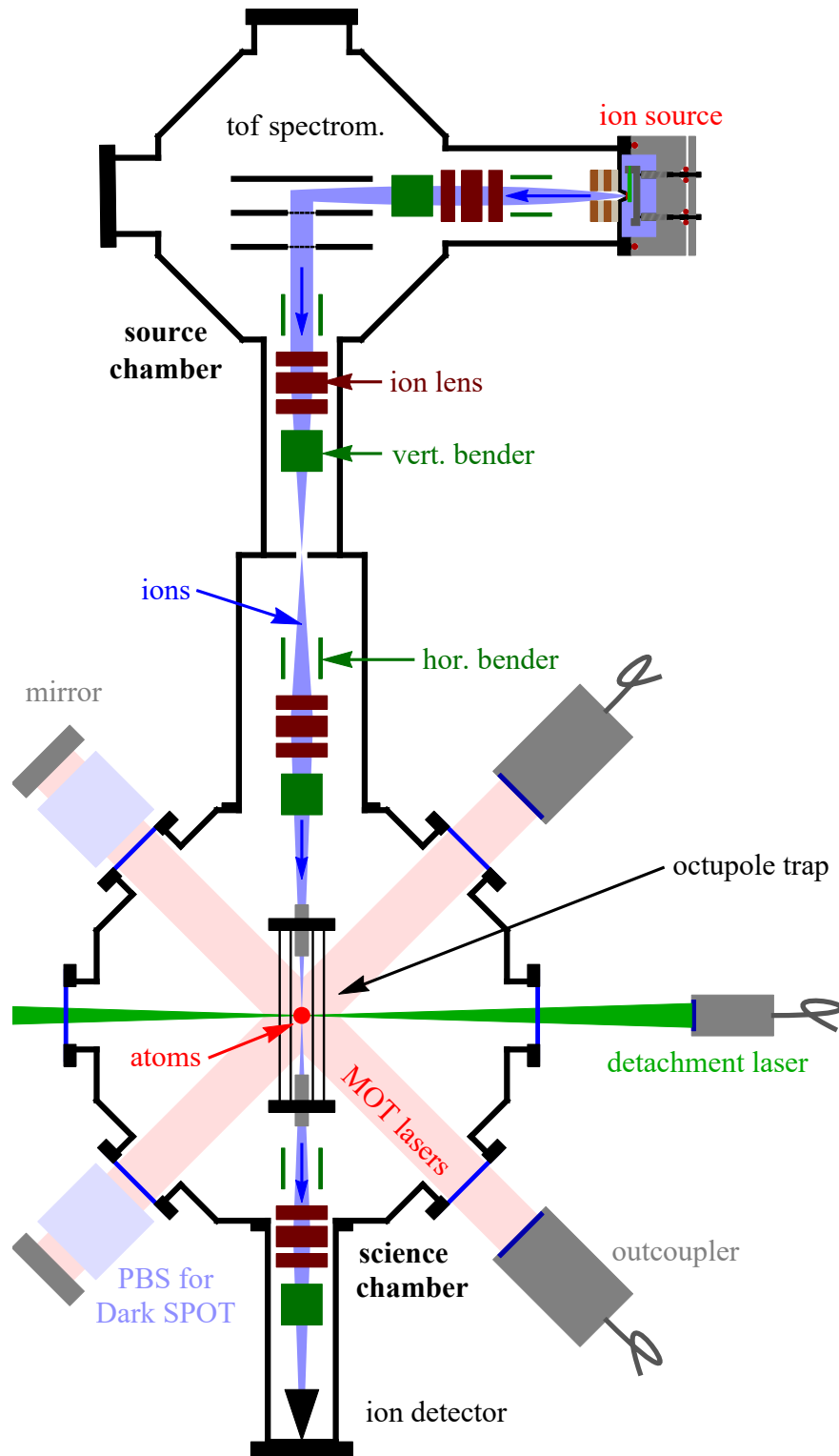


Figure 2.2: Schematics of the hybrid atom-ion trap (HAITrap). See text for details.

2.1 Ions

This section is aimed to describe the elements for ion control in our HAITrap. For this purpose, an overview of the fundamental working principle of a radio frequency ion trap is presented. Additionally, the specific experimental components for ion control in the HAITrap are described. For this, the ion source for the generation of negative charged ions, the ion optics, the ion trap, its components, its loading, the ion extraction procedure and ion detection as well as a characterization of the ion trap are presented.

2.1.1 Fundamentals: from Paul to multipole rf traps

Wolfgang Paul and Hans Dehmelt obtained the Nobel Prize in physics *for the development of the ion trap technique* [70]. Before the invention of such traps, Earnshaw postulated in 1842 that it would be impossible to store an electric charged particle in free space because, it is not possible to create an electrostatic potential minimum in a free 3D region due to the consequent violation of the Laplace equation $\nabla^2 V = 0$. For solving this problem, Dehmelt combine of a strong magnetic field with a static magnetic field [71], whereas Paul used radio frequency fast oscillating electric fields [72].

Paul traps

The invention of radio frequency traps was a consequent development from the existing methods at that time in order to manipulate ion trajectories through multiple pole field landscapes, which were primarily used to perform precision mass spectroscopy [72]. Although there are several possible geometric configurations for the experimental realization of such traps, all of them are based on the same principle.

Consider a charged particle surrounded by a set of $2 * n$ electrodes ordered in such a way, that opposing electrodes have the same polarity at a given voltage U_0 but neighboring electrodes have opposite polarity with voltage $\pm U_0$ (see figure 2.3). Here, n stands for the trap order and first the Paul trap which uses four electrodes ($n = 2$) will be presented. The electrodes' surfaces are formed in a hyperbolic fashion, marked as gray zones in the figure. In such a geometrical configuration, the resulting static electric field is that of a quadrupole field (marked with gray arrows) and the ions would be attracted by the electrodes that have its opposite charge. Nevertheless, applying an alternating voltage with amplitude U_0 , starting with the same polarity as above, and an angular frequency Ω on the electrodes, the electric potential φ is time dependent. In such potential, a charged particle experiences an effective force in the plane perpendicular to the electrodes that pushes it towards the center.

As a mechanical analogy, Paul suggested the model of a ball on a saddle surface, which would simply fall in the static case. If the saddle is rotated, the ball can be hold in its center [72]. Although this mechanical analogy is not entirely true for the electric potential as at a given time the potential is zero in the

2 Hybrid Atom-Ion Trap (HAITrap)

total volume, it gives an intuitive picture of the trapping principle. Surprisingly, the equation of motion of a charged particle inside such an alternating field can be analytically solved using a set of differential equations that were known about one century earlier, nowadays known as the Mathieu equations [72, 73]:

$$\begin{aligned} \frac{d^2 x_i}{d\tau^2} - q_{x_i} \cos(2\tau) \cdot x_i &= 0; \quad \text{where} \\ q_{x_1} = -q_{x_2} &= \frac{4eU_0}{mr_0^2\Omega^2}; \quad \tau = \frac{\Omega t}{2}; \end{aligned} \tag{2.1}$$

with $x_i = \{x_1, x_2\}$ \rightarrow space coordinates perpendicular to electrodes,
 q_{x_i} \rightarrow AC stability parameter,
 r_0 \rightarrow trap's radius, i.e. lowest distance from the
 \rightarrow electrodes to the trap's center,
 e elementary charge,
 m \rightarrow particle's mass,

Equations 2.1 can be divided in two types of solutions: stable and unstable trajectories. The stable solutions are given for low ratios of voltage amplitude and radio frequency. These solutions describe a particle oscillation with limited amplitude in the $\{x_1, x_2\}$ plane and are always closed trajectories. The unstable solutions describe particle trajectories in which the oscillation amplitude increases with time, leading to escape of the particle from the trapping volume. Note that these equations can be solved when a DC potential offset is applied at the electrodes, leading to the so called DC stability parameter. Nevertheless, this is only relevant for mass selectors and most of the traps do not use this configuration.

An example of a stable trajectory is depicted in the upper left graph of figure 2.3. As can be observed, a closed trajectory is depicted in the figure. For describing this trajectory as a function of time, a 1D projection is more suitable. The charged particles carry out movements that are composed of a slow secular oscillation with a certain frequency, called *macromotion*. This is modulated by a fast motion, called *micromotion*, which follows the applied alternating voltage.

The macromotion can be described by the movement of a particle in an effective harmonic potential, also called ponderomotive potential or pseudopotential. This defines the space in which the particles are stored.

If the electrodes are elongated perpendicular to the $\{x_1, x_2\}$ plane (the axial axis), then this geometry is called a linear Paul trap. In this case, for axial confinement the use of further electrodes are needed (commonly called end cap electrodes), which are set to a static potential with the same polarity as the charge of the particle to be trapped.

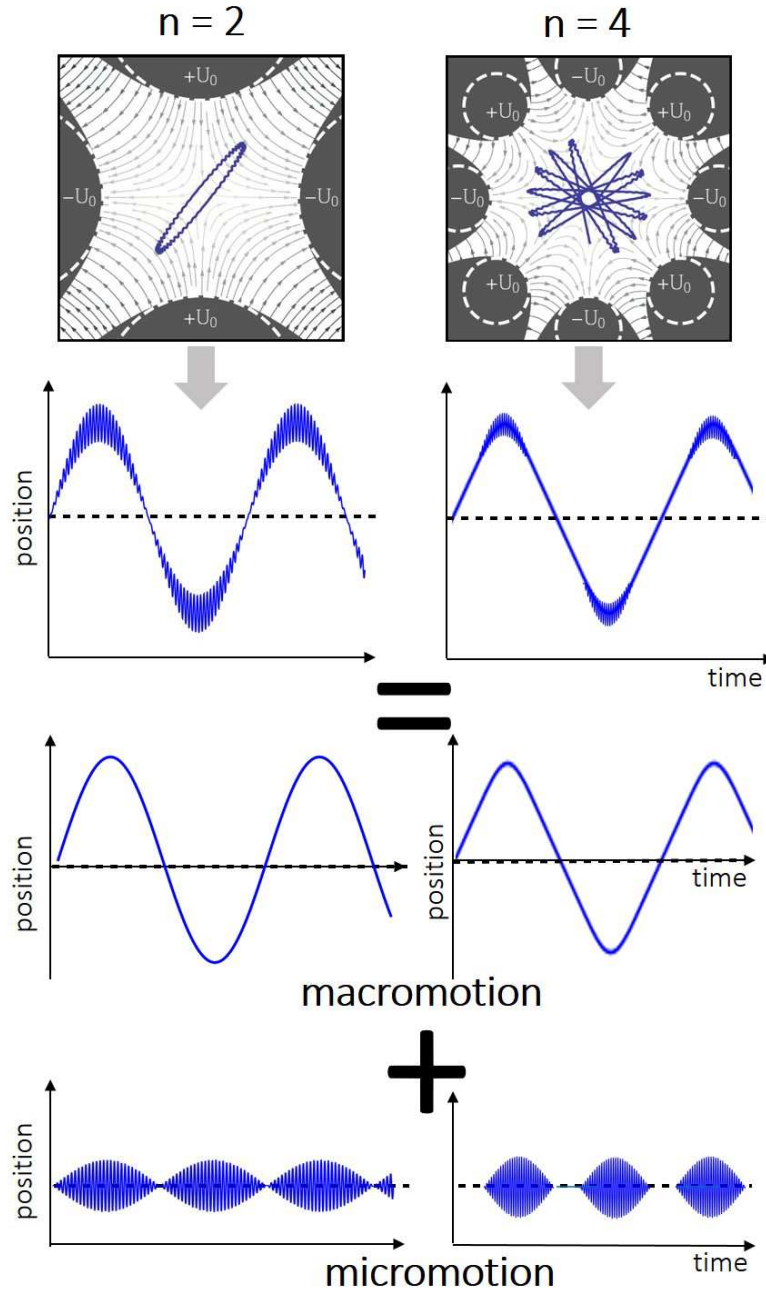


Figure 2.3: Ion motion inside a radiofrequency trap. Visualization of the macro and micromotion for different trap orders: a Paul trap ($n = 2$) and an octupole trap ($n = 4$). For $n = 2$ the trajectory is described by a closed orbit and the macromotion is harmonic. For $n = 4$ the trajectory is not a closed orbit, the macromotion is anharmonic and one observes a large region near the trap's center where the ions micromotion nearly disappears.

Multipole traps

In the case of a trapped particle surrounded by more than 4 electrodes ($n > 2$), the so called multipole traps, the static field at U_0 is given by a $2n$ -pole field. An octupole field (trap order $n = 4$) is depicted in figure 2.3. For an ideal configuration, the electrodes have to be shaped such that their surfaces coincide with an equipotential line from the octupole potential.

Unfortunately, for multipole trap configurations the exact ion trajectories cannot be solved analytically, because the equation of ion motion in the position coordinates is not separable, unlike the case of Paul trap. However, if the micromotion $\vec{x}(t)$ is much faster than the macromotion $\vec{R}(t)$, the time scales of micro- and macromotion can be separated, i.e. $\vec{r}(t) = \vec{R}(t) + \vec{x}(t)$ and the so called adiabatic approximation can be applied [74, 10]. In this case, the micromotion in the oscillating field is expressed by

$$\vec{x}(t) = -\frac{e\vec{E}(\vec{R}, t)}{m\Omega^2} \sin \Omega t \quad (2.2)$$

with $\vec{E}(\vec{R}, t) \rightarrow$ electric field in \vec{R} at time t ,
 e elementary charge,
 m particle's mass,

For practical reasons, in most of the experiments the use of round cylindrical rods are preferred over the hyperbolic electrodes [7]. In this case it can be shown that there is a radius of the rods for which the resulting electric field can be well approximated to a n -pole field [74]. This radius is given by $R_0/(n - 1)$ and is also depicted in figure 2.3 as dashed white lines. Here, the macromotion can be interpreted as a motion within an effective conservative, cylindrically symmetric potential of the form

$$V_{\text{eff}}(\vec{R}) = \frac{(e n U_0)^2}{4m\Omega^2 R_0^2} \left(\frac{R}{R_0}\right)^{(2n-2)}. \quad (2.3)$$

This equation is plotted in figure 2.4 for different trap orders. This effective potential has the property that with increasing pole order n , the central region of the trap becomes almost field-free and the confining potential in the outer parts is steeper. Moreover, the effective potential is closely related to the ion's micromotion. This can be clearly seen by comparing equation 2.2 with 2.3, noticing that the micromotion's time-averaged kinetic energy can be interpreted as the effective potential:

$$V_{\text{eff}}(\vec{R}) = \left\langle \frac{1}{2} m \dot{\vec{x}}^2 \right\rangle. \quad (2.4)$$

In conclusion, within this approximation, the ion confinement in radial direction can be interpreted as a transformation of the macromotion's kinetic energy

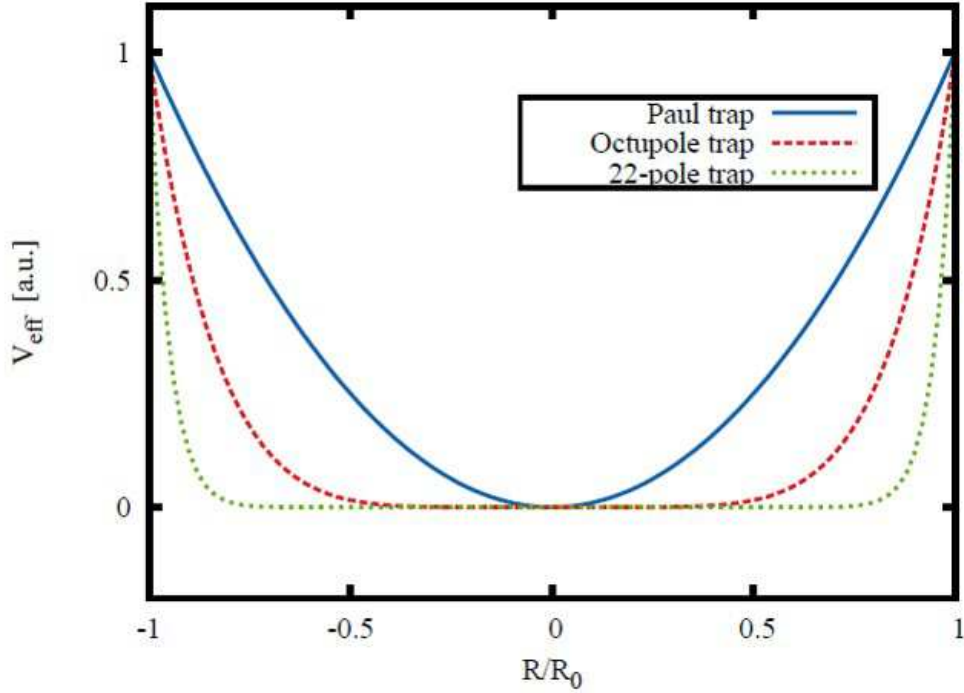


Figure 2.4: Effective potential for different pole orders. The effective potential is plotted as a function of the trap’s radial position R in units of its radius R_0 . The cases for a Paul trap ($n = 2$), an octupole trap ($n = 4$) as is the case of our experiment, and the widely used 22 pole trap ($n = 11$) are depicted with different colors. One observes, the higher the pole order, the flatter is the effective potential at its center.

into kinetic energy of the micromotion, leading to a maximum radius R_{\max} of the ions macromotion. For a comparison of the resulting motions in the case of a Paul trap and an octupole trap see figure 2.3.

2.1.2 Ion source

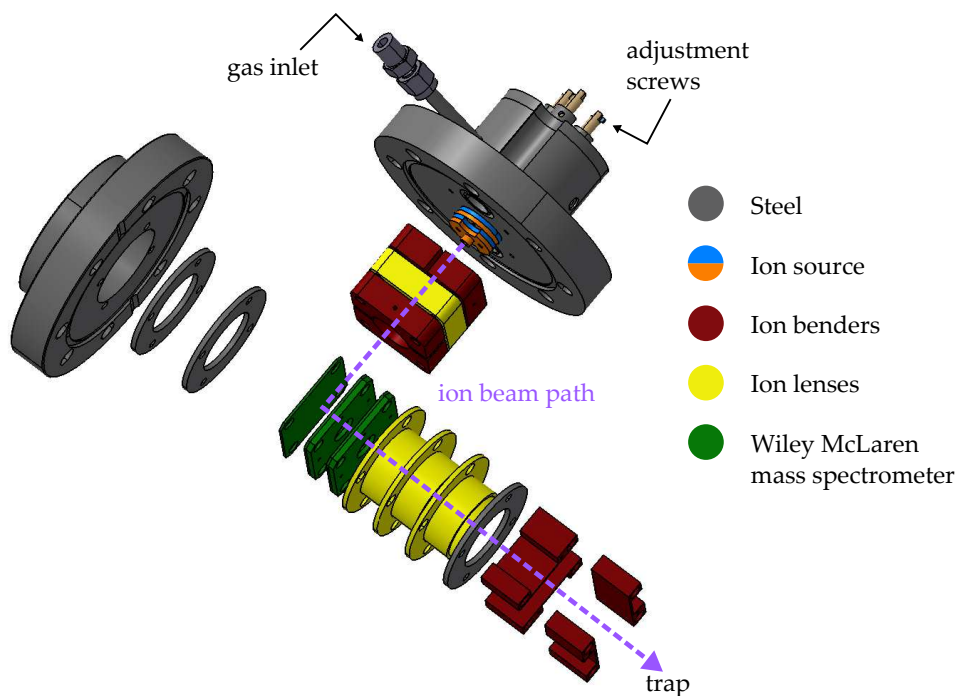


Figure 2.5: 3D model of the ion source chamber. After the ions are created in the plasma discharge ion source (see figure 2.6), they are guided onto the spectrometer electrodes where the ions are mass-selected and accelerated towards the ion trap. Further ion optics are used to guide them to efficiently pass the differential pumping stage between this and the science chamber.

In order to generate OH^- , a custom design of a plasma discharge ion source was developed in the course of this work, based on the design introduced in [75] and the further developments from our collaboration group [76, 43]. These kind of ion sources are widely used due to their versatility for the production of a wide range of negative ion species (e.g. OH^- water clusters [77]) with a relatively cold internal temperature. Some technical details from the design have been already reported in [59] and a more detailed characterization of the source was done in the scope of a Bachelor thesis [68].

Design

The generation of the ions is based on the ignition of a glow discharge via ionization of a mixture of gases. A glow discharge is a type of plasma which is created by applying a voltage of several hundreds of volts between two electrodes, where a low-pressure gas is stored. While the voltage is applied, any free moving charged particle is accelerated and it can ionize a neutral particle.

2 Hybrid Atom-Ion Trap (HAITrap)

The resulting ionic products are again accelerated and eventually ionize further particles, leading to a domino effect. The ionization becomes self-sustaining for a certain voltage value, at which point the gas glows with a colored light that depends on the gases used.

Figure 2.6 shows the most important components of our ion source, known in our laboratory as the Lopez source. It consists of a gas container, a valve which separates the gas reservoir from the vacuum, and the plasma generation electrodes placed inside the vacuum. The gas container (marked as a blue area) can be filled out with a mixture of gases, which determine the creation of the desired ion species. In our experiment, argon gas at about 1 bar mixed with water vapor for the creation of OH^- is used. For prevention of gas leaks, sealing rings (marked with dark red) are used at each flange connector.

The valve that controls the gas flow into the vacuum consists of a $200\ \mu\text{m}$ diameter hole which is closed by a hard rubber. The rubber itself is glued on the surface of a biomorph piezo element, which can be bent up or down by applying a voltage of a given polarity on one of its surfaces and ground to the other. In this way, by controlling the voltages applied to the piezo, the gas can expand supersonically through the small hole into the vacuum (see inset in figure 2.6).

Since the maximum displacement of the used piezos is on the order of $100\ \mu\text{m}$, all mechanical parts have to be stable to a fraction of this distance. Therefore, placing it at the right position is usually the most challenging part for adjusting the piezo system. For this aim, the piezo is mounted in a mechanical system which is based on typical optomechanical designs for precision positioning, such as laser mirror holders. The piezo holder is pulled by three mechanical springs (not shown in the figure) mounted between lid B and the piezo holder, pressing the piezo holder onto the three adjustment screws, two of them schematically shown in the figure. For preventing gas leaks, another lid is installed on top of lid B, pressing the sealing rings around the top of the adjustment screws.

On this way, the total distance from the rubber to the valve hole as well as slight angles for compensating mechanical imperfections, can be precisely adjusted. Furthermore, the piezo holder can be adjusted from the outside of the gas container while the valve is in operation (see also figure 2.5). This is of great advantage in many stages of the valve operation: for instance, to compensate unwanted displacements of the piezo, unavoidable deformations of the rubber and to optimize the gas flow into the chamber for optimal plasma ignition. This is in contrast to previous designs, where, for maintenance or adjustment, the valve has to be removed from the chamber, leading to the breaking of the vacuum, which further implies a time-consuming procedure of the restore it. Furthermore, in previous designs the piezo adjustment had to be done in a separated test chamber without the possibility of using different gas mixtures or the pressures wanted for the current experiment.

2 Hybrid Atom-Ion Trap (HAITrap)

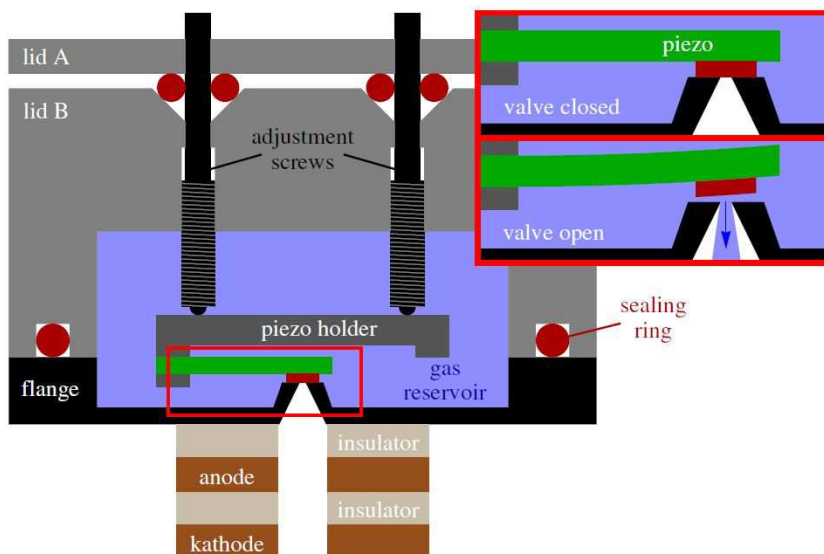


Figure 2.6: Schematic cut through the custom designed ion source.

The ion source consists of a gas container, a valve which separates the gas reservoir from the vacuum, and the plasma generation electrodes placed inside the vacuum. The opening of the valve for gas flow into the chamber is controlled by a bimorph piezo element, as shown in the inset. The expanding gas is ignited to a glow discharge inside the electrodes in the vacuum chamber, generating the desired ions.

Glow discharge ignition

When the piezo valve is open, the gas expands inside a cylindrical tube consisting of the ignition electrodes and insulators between them, as depicted in figure 2.6. About $150 \mu\text{s}$ after the opening of the valve, the gas reaches the ignition electrodes. At this point, an $80 \mu\text{s}$ pulse of about -800 V is generated by a fast high voltage Belke switch, which is connected via a ballast series resistor to the cathode, while the anode is grounded. The strong field generated in this way ignites the glow plasma as explained above.

For monitoring the plasma ignition, the voltage between the anode and the cathode is measured by means of a high voltage probe. If a glow plasma is generated, a net current flows from anode to cathode, leading to a reduction of the measured voltage during breakdown of the gas.

After the high voltage pulse, the (positively and negatively charged) generated ions expand further until they reach the spectrometer electrodes, from where they can be separated by charge and mass.

Time of flight spectrometer

In order to extract the ions from the ion source chamber, we use a time of flight (ToF) mass spectrometer based on the design introduced by Wiley and McLaren [78]. It consists of three plate electrodes as depicted as green electrodes in figure 2.5. A simplified version of the setup is shown in figure 2.7.

The acceleration of the charged particles is done in two stages. The right electrode (ground plate) is set to ground potential, the middle electrode (back plate) is set at a voltage V_2 and the left electrode (front plate) is set to $V_1 + V_2$, creating two different constant field gradients, as depicted in figure 2.7. The distance between the plates is d_1 and d_2 respectively. The ions arriving from the source are placed between the front and the back plates. In such a configuration, this spectrometer allows the separation of different ionic species in such a way, that the spatial point L at which the ions of one species arrive simultaneously (e.g. a detector, or in our case the ion trap) can be arbitrarily chosen by [78]

$$L = 2sk_0^{3/2} \left(1 - \frac{1}{k_0 + k_0^{1/2}} \frac{d_2}{s} \right) \quad \text{with} \quad k_0 = 1 + \frac{d_2}{s} \frac{V_2}{V_1}. \quad (2.5)$$

This means, that a space focusing of the ions can be achieved for an arbitrary position L by adjusting the voltage ratio $\frac{V_1}{V_2}$. Furthermore, the ions ToF to the position L is given by

$$t_{\text{total}} \propto \sqrt{\frac{m}{q}}. \quad (2.6)$$

In this way, the ions arriving from the source can be either focused into the ion trap, or to the detector for the characterization of the ion species created in the source. Our setup is made of three quadratic metal plates of length 51 mm and thickness of 1.1 mm. The plates are separated by the distances $d_1 = d_2 = 11$ mm. The back and ground electrode plates have centered circular apertures of diameter 12 mm covered by thin metal wire meshes for reducing field inhomogeneities at high ion transmission.

For allowing the ions to enter the acceleration region of the ToF spectrometer, the front and back plates are simultaneously switched from ground to the needed high negative voltages. In order to focus them into the trap, voltages of typically $V_1 = 250$ V and $V_2 = 16$ V were chosen. These voltages are switched on by means of fast high voltage Belke switches, which are triggered after a delay of typically $60 \mu\text{s}$.

2 Hybrid Atom-Ion Trap (HAITrap)

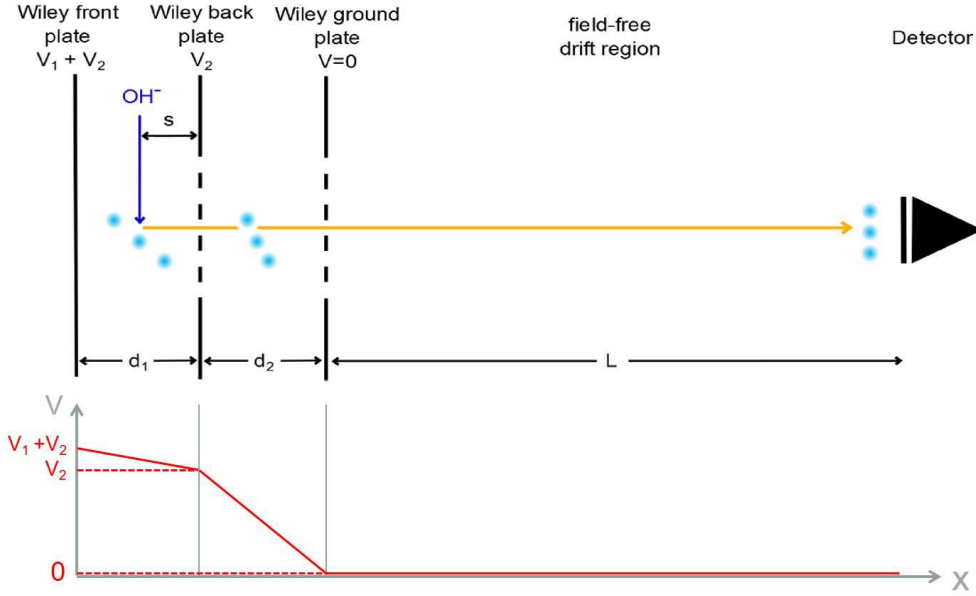


Figure 2.7: Working principle of the time of flight spectrometer. Three electrode plates at different voltages create two different acceleration regions with constant field gradients. This leads to a spatial focusing of the ions at an arbitrary position L by choosing the right ratio between the voltages $\frac{V_1}{V_2}$ (equation 2.5).

2.1.3 Thin wire octupole ion trap

The thin wire ion trap was set up in the group of Prof. Roland Wester and has been already used for other experiments [44, 43]. For our experiment, the mounting design was modified in order to integrate it into our vacuum chamber. The most important criterion for the design of this trap is the good optical access, which is an advantage over traditional multipole configurations. In those traditional traps the electrode rods obstruct the view of the ion cloud, and the needed laser for atom cooling can not reach the inner region of the trap. In contrast, the octupole arrangement features a compromise between the trap potential requirements mentioned above and provides optical access in a very wide solid angle range.

Figure 2.8 shows a 3D model of the ion trap and its surrounding compensation electrodes as well as ion optics. These components are all mounted in a cage made of four threaded rods fixed into a single CF160 vacuum flange. In the same flange the needed electrical feedthroughs as well as the buffer gas connection are installed, such that the different elements could be assembled and checked before the integration of the setup into the vacuum chamber.

The octupole rf-trap has a diameter of 6 mm and is 34 mm long. The wires are made of gold coated molybdenum and have a diameter of $100 \mu\text{m}$. It is surrounded by several electrodes for compensating possible external fields and

2 Hybrid Atom-Ion Trap (HAITrap)

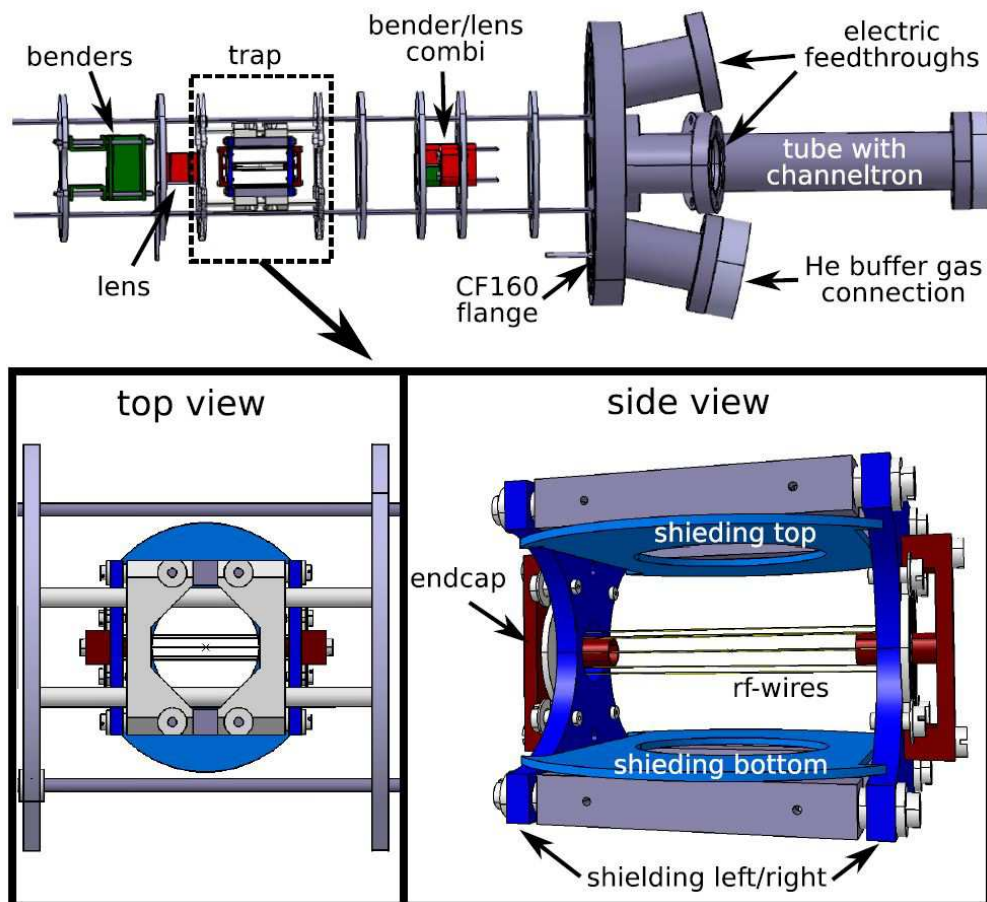


Figure 2.8: 3D model of the ion trap with its surrounding compensation electrodes and ion optics. The top graph shows the mounting cage of the whole system. The bottom figures show a more detailed view of the radio frequency trap.

for optimizing the ion loading procedure.

To generate the radio frequency needed for radial confinement, a frequency generator based on the design introduced by Anderson was used [79, 80]. This provides two sinusoidal radio frequency signals, which are shifted by 180 degrees from each other. Furthermore, the voltage amplitude can be varied manually as well as digitally and can be turned off by means of a digital trigger.

The voltage of each single electrode can be controlled digitally by the control software. The voltage supplies from the Iseg company provides a maximum of ± 500 V. Furthermore, the required high voltage fast switching of many electrodes, e.g. for ion loading or extraction, is done via MOSFET switches from the company Belke.

Loading procedure

By using an ion lens, which is mounted few centimeters in front of the first end cap electrode, the ions are focused and guided onto the center of the trap.

For decelerating the ions arriving from the mass spectrometer, which have a kinetic energy on the order of 250 eV, different DC voltages need to be applied to the compensation electrodes as well as to the rf wires.

The wire electrodes are set at a DC potential of 250 V such that the ions lose their kinetic energy when climbing onto this potential landscape. At the beginning, to allow the ions to enter the trapping volume, the first hollow end cap electrode is set to a potential of 125 V, which acts as a further guide for the ions. The second end cap electrode is set to 260 V in order to avoid the escape of the ions through this hollow end cap. Once the ions have reached the center of the trap, the end cap electrode is switched to the same potential as the other end cap electrode (260 V), providing an axial confinement of the ions.

For radial confinement an rf-voltage with typical amplitude of $U_{rf} = 200$ V and frequency of $\Omega_{rf} = 2\pi \cdot 7.8$ MHz is applied to the thin wire electrodes with neighboring opposite polarity. Furthermore, during the loading procedure, a Helium buffer gas pulse is applied, which flows into the trapping region via a pulsed valve. In this way the ions thermalize with this gas, making the loading procedure more effective. After the pulse, the pressure in the chamber increases for a short time up to 10^{-5} mbar. The gas is pumped out within a few seconds by the turbo pump.

Furthermore, stable trapping conditions are only possible by applying adequate voltages to the further shielding electrodes. This is because the DC offset at the wires causes an axial deconfinement which cannot be compensated by the end cap electrodes (see figure 2.10). For compensating this, a voltage of typically 280 V needs to be applied at the axial shielding electrodes. Nevertheless, this electrodes as well as the end cap electrodes cause a radial deconfinement, which need to be compensated by the radial shielding electrodes. Though this allows an efficient trapping of the ions, this potential landscape leads to radial potential pockets. A detailed optimization of the loading procedure was made in the scope of a Bachelor thesis [63]. For a better understanding of the potential landscapes, we have performed numerical simulations using the program SIMION.

SIMION

The performed simulations in this work are based on the software SIMION [81]. This computer program allows to calculate electrostatic fields and ion trajectories for a given configuration of electrodes at a given voltage. For each electrode, the geometry of all the loaded electrodes is set as boundary condition for numerically solving the Laplace equation

$$\nabla^2 V(\vec{r}) = 0, \tag{2.7}$$

with ∇ being the nabla operator and $V(\vec{r})$ the electrostatic potential. In this way, the numerical algorithm tries to find a constant electrostatic potential on

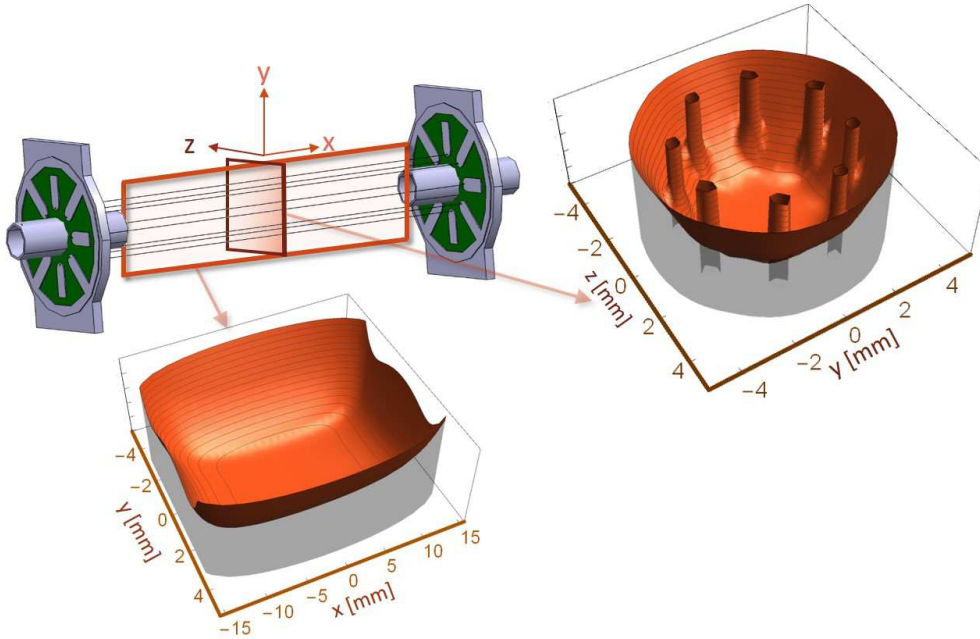


Figure 2.9: 2D cuts of the potential landscape calculated in SIMION.

For these calculations, all DC compensation electrodes (shown in figure 2.8) as well as the effective potential in radial direction are taken into account. On the top-left side of the graph the schematics of the thin wire rf-ion trap is shown. The orange rectangles show the planes used in order to probe the trapping potential for the further analysis. To the right an example is shown, where the total radial trapping potential is plotted as a function of both radial positions (y, z). The potential probing is done at the center of the trap ($x = 0$). Similarly, the bottom graph shows a potential cut through the radial center at $z = 0$.

the electrodes' surface. Similarly, the electric field is subject to be perpendicular to the electrodes' surface. Furthermore, in the numeric method implemented in SIMION, the volume of the potential to be calculated is divided in discrete cubic grids. Each grid contains the information of the electric potential caused by the electrode for the 3 cartesian axes. The resulting potential calculated for each electrode is stored as an array of the grids values at each grid position.

Based on the superposition principle of electric fields, i.e. they obey additivity and homogeneity, it is possible to add up all the calculated fields for each electrode, resulting in the final electric potential $V(\vec{r})$ the ions are subject to. This potential allows to numerically simulate particle trajectories by solving the equation of motion

$$m\ddot{\vec{r}} = -q\nabla V(\vec{r}) \quad (2.8)$$

for a given ion mass m and charge q . The numerical accuracy is limited only by the potential grid size and the time steps for solving this differential equation.

2 Hybrid Atom-Ion Trap (HAITrap)

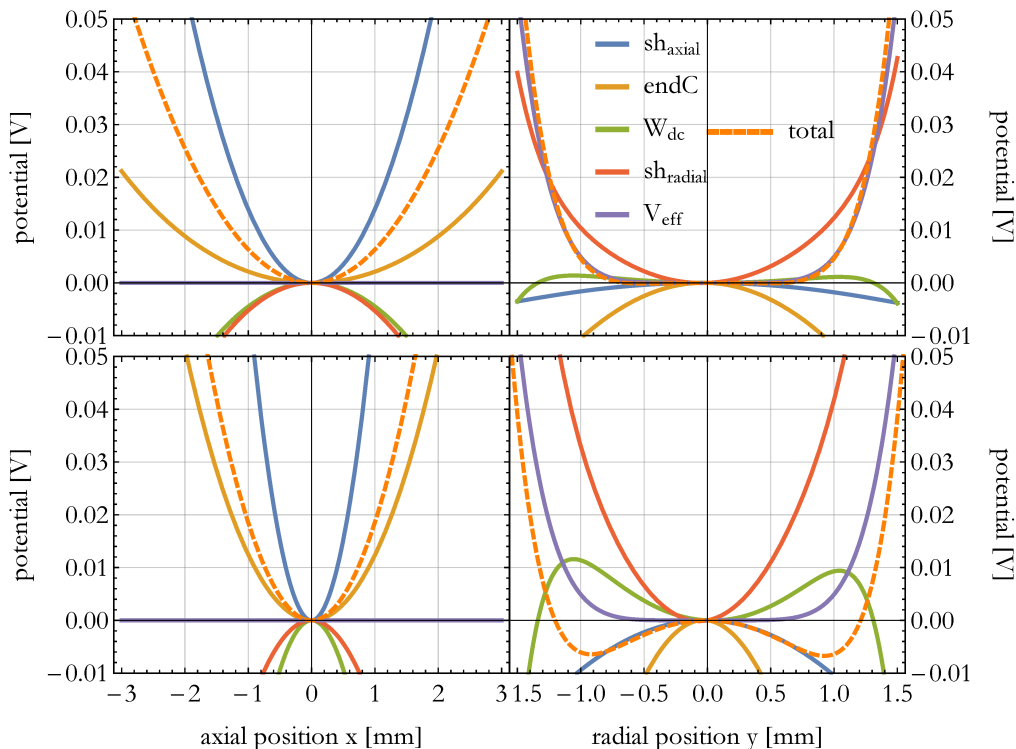


Figure 2.10: Comparison of the axial and radial landscapes at low and high voltages. The potential created by each electrode (color coded) as well as the effective and total potentials are plotted as a function of the axial (left graphs) and radial (right graphs) position. The upper/bottom graphs show the resulting potentials at low/high voltages. For the low voltage case, the radial pockets in the total potential nearly disappear.

For a better analysis of the total potential, the potential of each electrode i is calculated separately by setting it in SIMION at $V_i(\vec{r} = S_i) = 1$ V, i.e. at the surface S_i of the electrode geometry, and all others to 0 V. Afterwards, these potentials are exported and additivity and homogeneity of electric fields are used to calculate the total potential by the sum of each electrode set at a voltage a_i :

$$V(\vec{r}) = \sum_i a_i * V_i(\vec{r}). \quad (2.9)$$

As an example, two different 2D cuts of the resultant potential landscape are shown in figure 2.9. As discussed above for the ion loading procedure of the rf trap, the potential landscape produced by each electrode in our trap is critical for stable trapping conditions. The loading of the ions into the trap needs to be made at high voltages on the electrodes, which are required for decelerating the ions arriving from the ToF spectrometer.

The resulting potentials calculated in SIMION for the initial trapping conditions are shown in figure 2.10 (lower graphs). These are axial shieldings: 350 V;

2 Hybrid Atom-Ion Trap (HAITrap)

end cap electrodes: 270 V; DC offset at the wires 250 V; radial shieldings: 280 V; radial effective potential with rf voltage at 200 V; Thereby, the resulting potential generated by each of the electrodes is plotted as a function of the axial as well as the radial position. For a better comparison, the resulting potentials are related to the center of the trap. In axial direction, the axial shieldings as well as the end cap electrodes are confining potentials, whereas the wires' DC offset and the radial shieldings introduce deconfinement. In this direction the effective potential does not have any influence. In contrast, in radial direction the axial shieldings and the end cap electrodes are deconfining, whereas the wires' DC offset and the radial shieldings are confining potentials in the 1D cut chosen. In radial direction, the effective potential compensates for every resulting deconfinement, but the total trapping potential in this direction show local minima, also called radial pockets, the position of which are unfortunately exactly behind the rf wires. This is a disadvantage for the later experiments on sympathetic cooling, since cold ions will tend to be localized in such pockets. As a consequence, optical probing of the ions would be impossible in such conditions, as has been previously reported in [59].

As mentioned above, the control software was updated for controlling digitally each of the compensation electrodes. In this way, after the loading procedure, the voltages on the different electrodes can adiabatically ramped in order to avoid such pockets. To confirm this, the resulting potentials at relatively low electrode voltages are calculated: (see upper graphs of figure 2.10). The same analysis for each electrode can be done in this situation, i.e. all electrodes act in the same way regarding their confining properties. Nevertheless, for the resulting total potential in radial direction, the pockets are still present but their effect is negligible.

2.1.4 Characterization of the ion trap

After every experimental cycle, the ions are extracted from the trap by subjecting simultaneously the right end cap electrode to ground and the left axial shielding to about 100 V higher than its value during trapping. In this way, a potential gradient along the axial direction accelerate the stored ions out of the trap, which are then led to the ion detector. A more detailed analysis on the extraction dynamics will be presented in 3.3.1.

This section is intended to provide an overview of the ion detection procedure and its limitations. The radio frequency trap is characterized in terms of the cleaning procedure of O^- impurities and the ion losses of the rf trap due to background collisions.

Single ion detection

For detecting the ions in our experiment, a channel electron multiplier (CEM) from the company Sjuts is used. In such a detector, the incoming particles are accelerated by a high voltage onto its interior, creating an avalanche of secondary electrons. In this avalanche, about 10^8 electrons are generated, which

are collected by an anode. This results in a pulsed signal, which is amplified and recorded by a fast digital oscilloscope and afterward stored by the LabView control software for later analysis. More details on the electronic components used in our experiment can be found in [67].

A typical raw signal obtained after the extraction of trapped ions is shown in figure 2.11. The most important information from this signal is the arrival time of the ions. The software processes the signal in several steps. A moving average of the signal is computed in order to get rid of slow variations of the background noise. A threshold value is added to the moving average, which is used as a reference for peak detection. The threshold is chosen such that the background noise remains below it. When a peak from the raw signal overpass the cut threshold, the software stores the peak's mean time and count it as a detected ion (red points in figure 2.11). This is done for the whole trace, resulting in an array of time values at which such peaks were found by the algorithm.

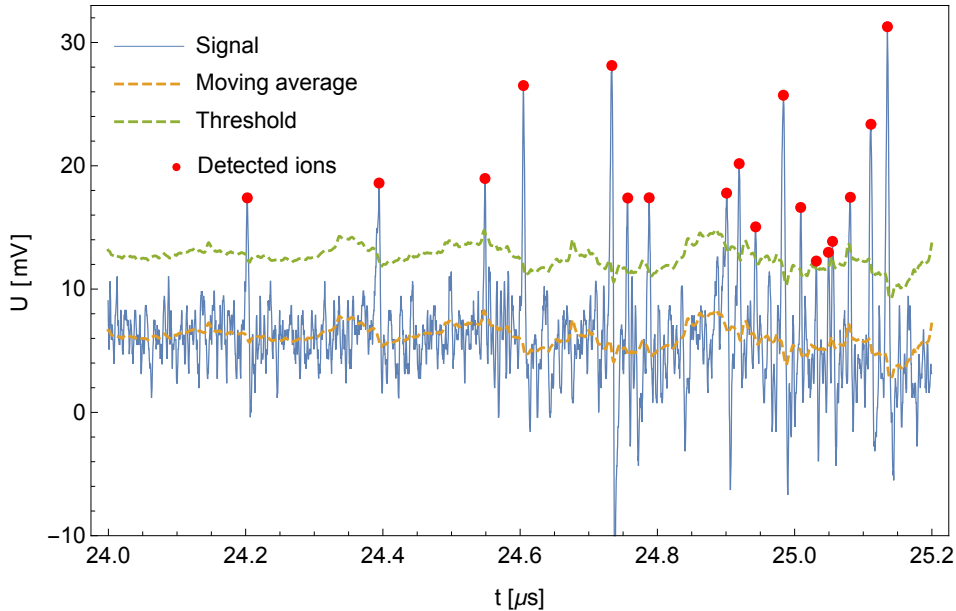


Figure 2.11: Algorithm for ion counting. Shown in blue is the amplified raw signal obtained from the channeltron as a function of time. For ion detection, a moving average of the raw signal is calculated and a threshold (here 6.5 mV) is added to it. If the signal raises over the threshold, a single ion is counted and its time of flight recorded.

Detector saturation

If two or more ions arrive within a few nanoseconds at the CEM ion detector, it can only detect one of these particles, in which case the detector is saturated [82]. In order to characterize a possible saturation of the detector, following

experiment is performed. By regulating the voltages on one of the ion lenses between the spectrometer and the trap, the mean number of ions loaded into the trap can be controlled. This happens because the loading efficiency of the trap depends critically on the ion guiding optics.

For this experiment, the maximum mean number of detected ions was set in the order of 40 ions per cycle. The ions are trapped and stored under the same experimental conditions in the rf-trap for a few seconds, and finally extracted towards the detector. The measured time of flight values are stored for each experimental run as explained above. This was repeated several times until a total number of about $2 \cdot 10^5$ ions were detected. The histogram of the ion arrival times is the resulting time of flight distribution.

To verify the detector saturation effects, the data is sorted by the mean number of ions detected in a single run and grouped together in three different ranges: 10 to 20, 20 to 30 and 30 to 40 detected ions. The resulting time of flight distributions for these groups are shown in figure 2.12. For each group, about $4 \cdot 10^4$ ions contribute to the obtained distributions.

On the left graph, no significant difference on the resultant time of flight distributions between the two groups (10 to 20 and 20 to 30) is observed. However, on the right graph the distributions are very similar at its wings, but the height of the distribution is significantly lower for higher ion counts. This is because at the maximum of their distribution, too many ions arrive in a very narrow time window, such that the CEM is saturated. As a consequence, for the following experiments, this effect limits the number of ions that can be detected within a single experimental run to a maximum of 30.

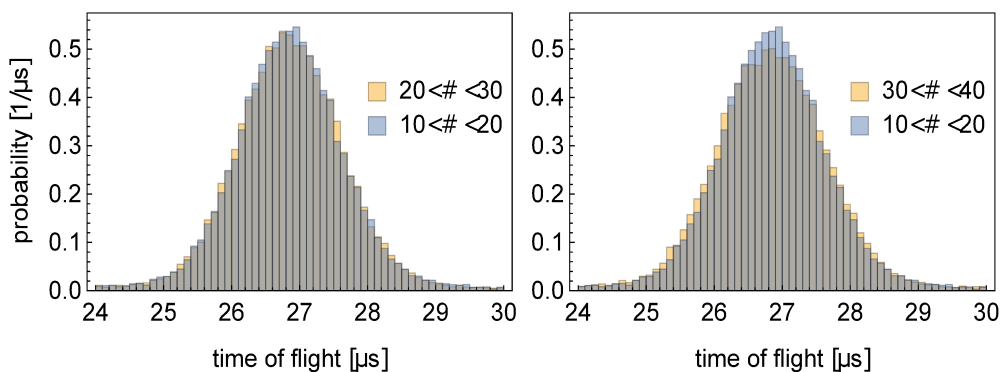


Figure 2.12: Saturation of the channeltron ion detector. Shown is the resulting time of flight distributions for different number of ions detected during a run. For these measurements, about $4 \cdot 10^4$ ions contribute to the obtained distributions. In gray, the overlap between the two histograms is shown. Saturation of the detector can be observed, as the height of the distribution is lower for higher ion counts.

$O^- + OH^-$ in the trap

Though the spectrometer discussed in section 2.1.2 allows for mass separation, during the loading procedure a significant amount of oxygen anions generated in the chamber are also trapped. Fortunately, the O^- photodetachment threshold (1.49 eV) is lower than the photon energy of the cooling lasers (≈ 1.59 eV) used for trapping Rubidium atoms in a MOT. Therefore, for cleaning O^- impurities in the trapped ion cloud, the cooling laser is shined into the trap and these anions are lost due to photodetachment.

For characterizing the time needed in order to get rid of the oxygen anions that were trapped during loading, following measurement is performed. The ions are loaded in the trap as explained earlier. The ion cloud interacts with the MOT laser for a certain amount of time and subsequently the ions are extracted and counted. This is repeated several times for different interaction times.

The results of this procedure are shown in figure 2.13. On the left graph, the mean number of ions is plotted as a function of the interaction time with the MOT lasers. The solid line represents a fit to the data using an exponential function with an offset. The fitting algorithm provides a decay rate of 1.06 s^{-1} , meaning that after 4 seconds, $\approx 1\%$ of the oxygen anions initially loaded remain in the trap.

The right graph shows the resulting ion time of flight distributions for no interaction (blue) and 6 seconds interaction time (orange) with the MOT laser. From this data, the O^- part of the distribution can be inferred.

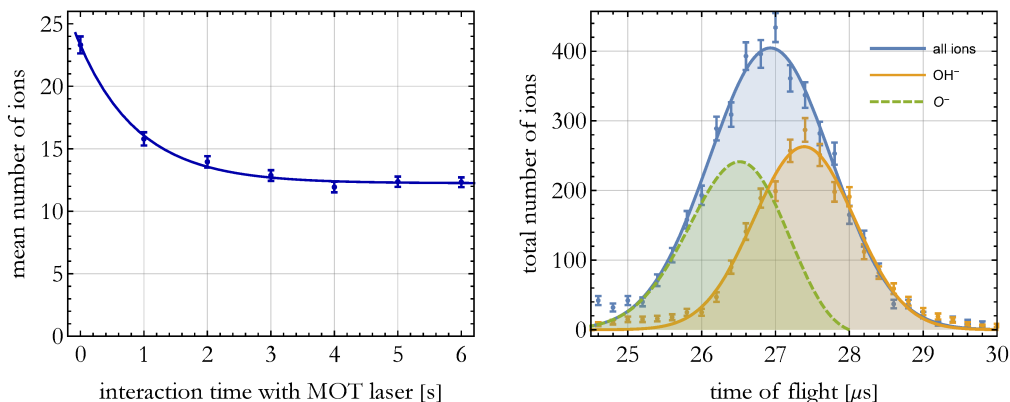


Figure 2.13: Photodetachment of O^- with the MOT lasers.

Left graph. The mean number of measured ions is plotted as a function of the interaction time with the MOT lasers. After 4 s about 1% of O^- remains in the trap.

Right graph. Resulting ToF distributions for all ions and only OH^- . From both curves the contribution of O^- to the total distribution can be inferred (green dashed curve).

Background losses

Once it is assured that only OH^- remains in the trap and the detector is not saturated, one important characterization is to determine the time anions can be stored in the radio frequency trap without any other influence. To measure this, once the ion cloud is prepared in the trap as explained before, the ions are extracted after a certain storage time.

In figure 2.14 the mean ion count is plotted as a function of the storage time. A fit to the data using a simple exponential equation provides a decay rate of $\kappa = 0.013\text{s}^{-1}$. This means that the ions have a mean life time in the trap of $\tau = 76.9\text{s}$.

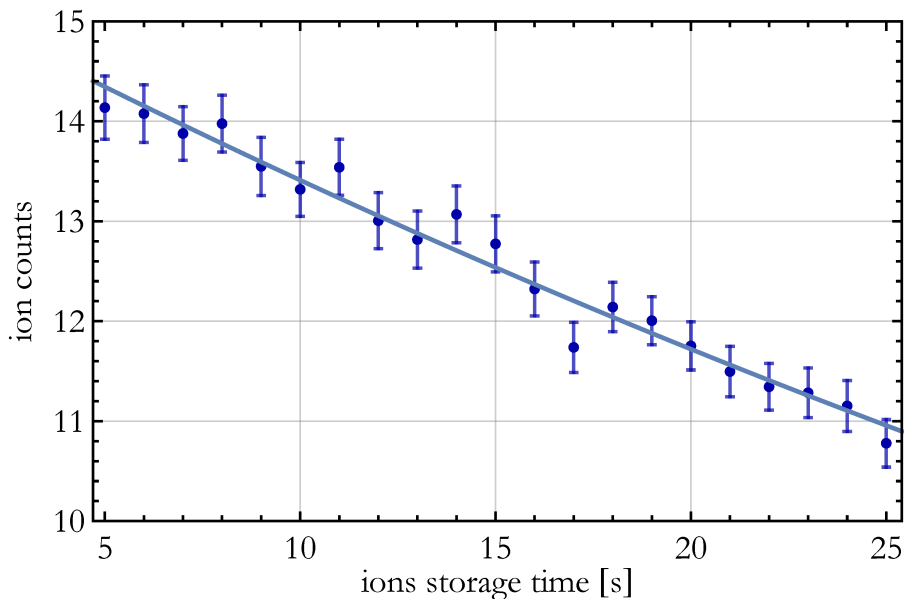


Figure 2.14: Ion trap background losses. The mean number of ions detected are marked with a dot. Their errors are calculated as the standard deviation weighted with the number of measurements. The blue line corresponds to an exponential fit with a decay rate of $\kappa = 0.013\text{s}^{-1}$

2.2 Atoms

In this section the atom cloud control elements in our HAITrap will be described. The methods used in the HAITrap for characterizing the atom cloud have been published by our group in [60]. Further technical and conceptional details can be found in [59, 61], where the atom cloud was characterized independently of the ion trap. An overview of the working principles of laser cooling and a darkSPOT and is presented in section 2.2.1. The implementation of a dark spontaneous-force optical trap (darkSPOT) for rubidium in our HAITrap is described in section 2.2.2. A characterization of our atom cloud is presented in section 2.2.3.

2.2.1 Fundamentals: From optical molasses to a darkSPOT

Laser cooling in combination with magnetic fields is a well established method to generate ultra cold samples of particles and has been described in several books and publications [6, 83, 84, 85]. In this section, a brief summary of this method is presented.

Consider a two-level atom moving against the propagation of a laser field with frequency tuned slightly below the electronic transition in the atom. Due to the Doppler effect, the atom absorbs eventually a photon from this laser field and the momentum of the photon is transmitted to the atom. Since the atom is excited to the higher state, it decays subsequently into its initial state either via spontaneous or induced photon emission. In the case of stimulated emission, the direction of the absorbed and emitted photons are the same, therefore no momentum transfer takes place. In the case of spontaneous emission, the direction of the emitted photon is independent of that of the absorbed photon and the atom receives a momentum kick in the other direction. After many absorption-spontaneous-emission processes, the recoil momenta average to zero for the mean velocity. This leads to a decrease of the atom's momentum in its initial direction of movement. If six pairs of opposing rays are used, the atom can be slowed down in all spatial directions. This results in a velocity-dependent force that acts on all atoms with velocity different from zero and slows them down. When a big ensemble of atoms is cooled down in this way, the resulting gas is called an optical molasses.

As real atoms usually have more than one state into which the excited atom can decay, the states that do not interact with the cooling light are called dark states. Depending on the atomic species, one or more lasers are used to optically repump the atoms into the cooling process, preventing the atoms from being lost by such decays.

Though this method is able to produce cold atoms, they might diffuse out of the range of cooling because there is only a velocity-dependent, but no position-dependent force. If a linear magnetic field gradient is superimposed to the cooling region (e.g. with an anti-Helmholtz arrangement of coils), then a position-dependent force arises. This is due to the Zeeman splitting of the atomic states, which is proportional to the magnetic field. Due to the selection rules of the Zeeman effect, it is necessary to irradiate circularly polarized light, since other-

2 Hybrid Atom-Ion Trap (HAITrap)

wise no interaction with the atomic states would be possible. This arraignment is called a magneto optical trap (MOT).

However, there are two main limitations regarding the achievable atom density in a MOT: i) when the density of an atom cloud is high enough, it becomes possible for the atom-emitted secondary photons to be re-absorbed by other atoms leading to a repulsive force between them. ii) when an atom collides with another excited atom, its excitation energy is transferred to the other atom as kinetic energy. This leads to losses from the trap, as the trap depth of a MOT is typically smaller than kinetic energy gained from such inelastic collisions. Both effects limit the maximum achievable densities in a MOT to a few 10^{10} atoms/cm³.

In order to avoid this, Ketterle introduced an alternative design for the optical system of a MOT, calling it darkSPOT [45, 86]. The main component of such atom trap is a repumping beam with a hollow core. With this optical setup most atoms within the "dark region" of the repumper beam decay into the dark state. They are only pumped back to the cooling transition once they reach the outer parts of the trap where repumping light is present. As a consequence, atoms being in the "dark region" are less probable to be in the bright state and scatter fewer photons, which are the main factors limiting the density. The atom density achievable in such traps is about one order of magnitude higher than in a normal MOT.

2.2.2 darkSPOT setup

In the HAITrap, ⁸⁵Rb is used as a buffer gas for cooling the ions. A schematic picture of the optical system used in the HAITrap for trapping and cooling the atoms is shown in figure 2.15. All relevant laser frequencies used in the setup are shown in the inset of the figure. A pair of anti-Helmholtz coils placed inside the vacuum chamber generate a magnetic field gradient of 60 G/cm. Additionally, in each space direction a set of Helmholtz coils are placed in order to slightly displace the zero position of the magnetic gradient for controlling the final position of the atom cloud and optimize the overlap between the ion and the atom clouds. The optical setup allows the generation of either a MOT or a darkSPOT, depending on the requirements of the experiment.

In order to laser-cool ⁸⁵Rb, two laser frequencies are needed. The

$$5^2S_{1/2} (F = 3) \rightarrow 5^2P_{3/2} (F' = 4)$$

transition is a closed cooling cycle (see inset on figure 2.15). Unfortunately, due to the small separation of the $5^2P_{3/2}$ ($F' = 4$) and ($F' = 3$) states the atoms can be excited to the ($F = 3$) state from where they can fall into the $5^2S_{1/2}$ ($F = 2$) or to the $5^2S_{1/2}$ ($F = 3$) state. As the cooling lasers do not interact with the $5^2S_{1/2}$ ($F = 2$) state, the

$$5^2S_{1/2} (F = 2) \rightarrow 5^2P_{3/2} (F' = 3)$$

transition has to be pumped as well in order to repump these atoms back into the cooling cycle.

2 Hybrid Atom-Ion Trap (HAITrap)

Typical capture velocities for rubidium atoms entering a magneto-optical trap are on the order of 30-40m/s which is about an order of magnitude smaller than typical velocities of thermal atoms at room temperature. To achieve fast loading times of the atom trap, we use a 2D MOT with an atomic flux of 10^9 atoms per second and a beam divergence of less than 50mrad. The mean velocity of the precooled beam from the 2D MOT matches the trapping velocity of the dark SPOT, increasing the trapping efficiency. Experimental details and the characterization of this source can be found in [87].

The laser beams are prepared in a separate optical table and are transferred to the experiment via polarization-maintaining single-mode optical fibers. Three fiber outcouplers provide beams with a diameter of 24 mm ($1/e^2$). The beams are circular polarized with a $\lambda/4$ waveplate and are retro-reflected after passing the vacuum chamber. Every beam contains light on the cooling transition. Additionally, the vertical beam contains light on the imaging transition which is used to probe the atom cloud. Both horizontal beams include light on the "fill-in" transition. These beams are used for re-pump atoms into the $5^2S_{1/2}(F = 3)$ in order to either generate a MOT or prior to the imaging sequence in a dardSPOT (section 2.2.3).

Additional repumping light is required for the darkSPOT, which is provided by two additional fibers. These beams pass a glass plate with a circular spot, which is imaged to the center of the trap using two lenses, creating a beam with a hollow core. An extinction ratio of about 1:200 has been measured outside the vacuum chamber, however this might be reduced due to reflections from the wires of the ion trap. The hollow repumping beams are overlapped with the horizontal trapping beams using polarization beam splitter cubes placed between the chamber and the cooling light. In this configuration, any trapped atoms in the dark region fall into the dark state $5^2S_{1/2}(F = 2)$. Most of these atoms are already cold enough to remain trapped and as soon as they reach the outer parts of the cloud, they are pumped back into the cooling cycle. This way, both mentioned limitations are overcome.

2 Hybrid Atom-Ion Trap (HAITrap)

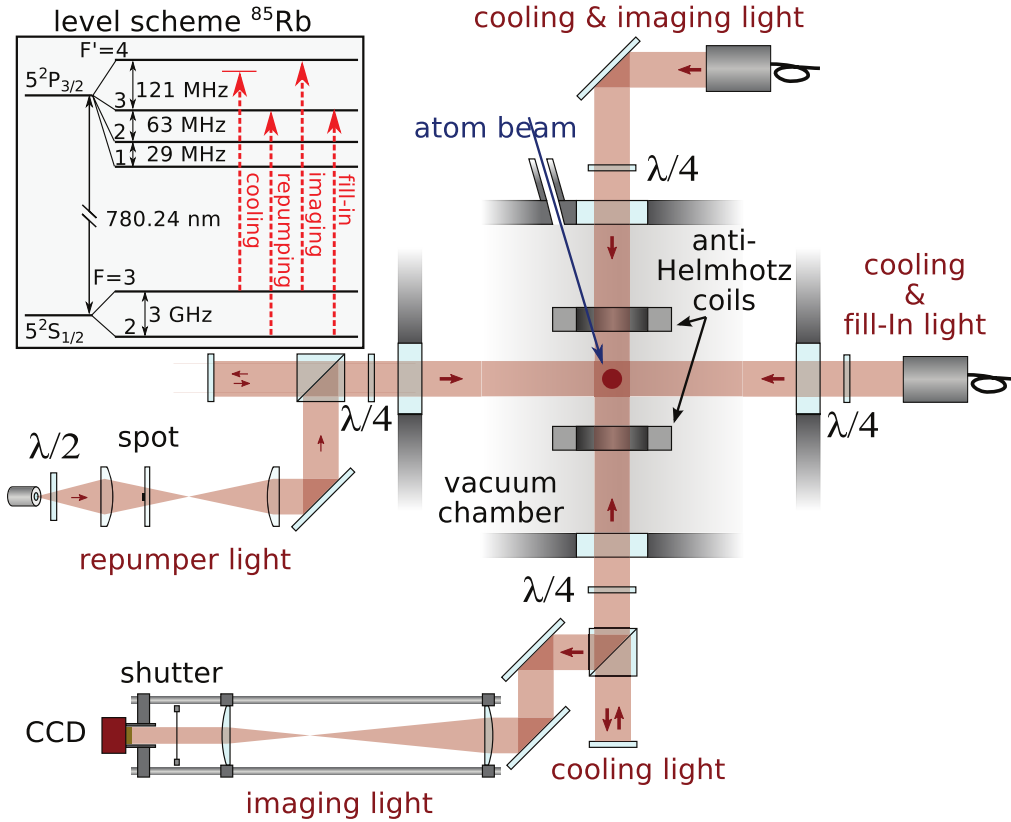


Figure 2.15: Optical setup of the Dark SPOT setup and the imaging system. See text for details.

2.2.3 Atom cloud characterization

For a hybrid trap experiment it is important to track the atom cloud characteristics (atom number, density, size, etc) in a single shot for every experimental run. In our experiment this is done by using a technique called *absorption imaging*, which is introduced in this section.

Absorption model

When a light beam with intensity $I(z)$ propagates in z direction through a medium, the light is attenuated along its path depending on the interaction type and strength with the medium. When the light's intensity drops after the interaction with the medium, it is assumed to be *absorbed*. The infinitesimal intensity change along the propagation direction is in such a case proportional to the beam's intensity on every point. This can be modeled by the following differential equation

$$\frac{dI(z)}{dz} = -\kappa_{\text{abs}} \cdot I(z). \quad (2.10)$$

2 Hybrid Atom-Ion Trap (HAITrap)

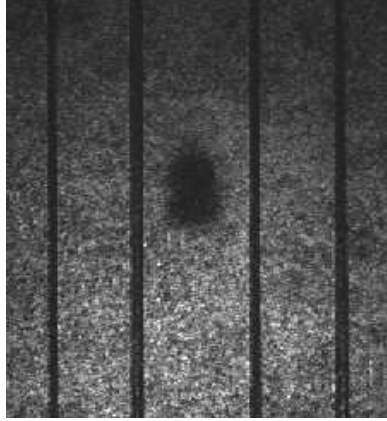


Figure 2.16: Example of an absorption image. Shown is a typical absorption image of the rubidium atom cloud. The vertical shadows are caused by the ion trap radio frequency wires whereas the shadow in the middle is caused by absorption of the imaging beam by the trapped atoms.

The proportional factor κ_{abs} in the former differential equation is called *absorption coefficient* and describes the interaction strength between the light beam and the medium¹. In the case where this medium is an atom gas cloud, the absorption coefficient becomes

$$\kappa_{\text{abs}} = \sigma_{\text{abs}} \cdot n(z) \quad (2.12)$$

where σ_{abs} and $n(z)$ denote the photon-atom-interaction cross section and the atom density distribution along the light propagation path respectively. Assuming a two-level atom, the absorption cross section can be calculated from the optical Bloch equations to be [88]:

$$\sigma_{\text{abs}} = \frac{\sigma_0}{1 + 4 \left(\frac{\omega - \omega_0}{\Gamma} \right)^2 + \frac{I}{I_{\text{sat}}}}, \quad (2.13)$$

with ω	\rightarrow	photon's angular frequency,
ω_0	\rightarrow	photon's angular frequency at resonance,
$\Delta \equiv \omega - \omega_0$	\rightarrow	laser detuning from the atomic resonance,
$\Gamma = \tau^{-1}$	\rightarrow	natural decay rate of the excited state; often referred to as natural linewidth,
I_{sat}	\rightarrow	atomic transition's saturation intensity,
$\sigma_0 = \frac{\hbar\omega\Gamma}{2I_{\text{sat}}}$	\rightarrow	on resonance cross section.

¹ Integrating 2.10 gives the solution of the differential equation which is known as Lambert-Beer's law:

$$I(z) = I_0 \cdot e^{-\kappa_{\text{abs}} \cdot z} \quad (2.11)$$

2 Hybrid Atom-Ion Trap (HAITrap)

Replacing 2.13 and 2.12 in 2.10 and solving the differential equation leads to

$$\left(1 + 4 \left(\frac{\Delta}{\Gamma}\right)^2\right) \cdot \ln\left(\frac{I_f}{I_0}\right) + \frac{I_f - I_0}{I_{sat}} = -\sigma_0 \cdot \int n(z) dz \quad (2.14)$$

where I_0 and I_f are the light intensities before and after its interaction with the medium.

The integral in the right part of equation 2.14 carries the information about the atoms spatial distribution. It is called atom column density distribution and is interpreted as the total number of atoms projected in a given area. Knowledge of the atom spatial distribution ρ_z makes possible the integration of this term. This gives the total atom number N_z along the light path. In the case of e.g. an harmonic potential, ρ_z is well described by a normalized Boltzmann distribution.

In the experiment, the parameters I_0 and Δ are controllable. The light intensity I_f as well as I_0 can be tracked by a calibrated light sensor putted behind the atom cloud. In the case of an array of light sensors as well as CCD cameras, equation 2.14 can be applied to model each CCD pixel. At the same time, if the absorption path of the atom cloud is properly imaged into the CCD-chip, the information about the spatial atoms distribution in x and y direction can be obtained. This technique is called absorption imaging. In the following section three different special cases are described: simple absorption imaging, non-resonant absorption imaging and saturation absorption imaging.

Simple absorption imaging

The simplest method for absorption imaging is setting the laser frequency at the atomic resonance ($\Delta = 0$) and the light intensity such that $I_0 \ll I_{sat}$. In this case equation 2.14 becomes

$$-\ln\left(\frac{I_f}{I_0}\right) = \sigma_0 \cdot N_z \cdot \int \rho(z) dz \quad (2.15)$$

The left part of this equation is defined as optical density (OD)² [89, 90] which can be measured by tracking the variation on the light intensity with a photodetector, with I_f and I_0 being the measured signal with/without an atom cloud. Note that for this technique the absolute intensity values are not necessary, but just the relative ones. Since the beam intensity is proportional to the value given by the photodetector, this can be directly used for the data analysis.

Using a CCD camera as a detector, allows to make an optical image of the absorption shape from the atom cloud into the chip. This provides information about the optical density in 2 dimensions (x, y) perpendicular to the light propagation direction (z). For every single detector in the CCD chip (pixel) the equation 2.15 can be applied and for each pixel at (x, y) we have

$$-\ln\left(\frac{I_f}{I_0}\right)_{x,y} = \sigma_0 \cdot N_{x,y} \cdot \int \rho(x, y, z) dz \quad (2.16)$$

²Note that the definition of optical density differs in the literature depending on the field and the context. Here we choose the same definition as in [89, 90]

2 Hybrid Atom-Ion Trap (HAITrap)

For the total number of atoms detected in one pixel one obtains

$$N_{x,y} = -\frac{\text{OD}_{x,y} \cdot A_{\text{pixel}}}{\sigma_0} \quad (2.17)$$

being A_{pixel} the area of one pixel weighted with the magnification of the optical image of the cloud into the CCD chip. This equation provides the total number of atoms N independent on the information about the form of the trapping potential. Adding the atoms detected for each pixel then the total number of atoms N can be obtained:

$$N = \sum_{x,y} N_{x,y} \quad (2.18)$$

Furthermore, assuming that the atoms are trapped in an harmonic potential in 3 dimensions following the Maxwell-Boltzmann statistics, the single atom density $\rho(x, y, z)$ is described with a normalized Gaussian distribution. This means that the optical density is also Gaussian distributed. Hence, by fitting this model to the information extracted from the CCD image (OD) using equation 2.16, the geometrical information about the atom cloud can be gained. The fitted model is referred as the fitted optical density $od(x,y)$ and in this case is:

$$od(x, y) = od_0 \cdot e^{\left(-\frac{(x-x_0)^2}{2 \cdot \sigma_x^2} - \frac{(y-y_0)^2}{2 \cdot \sigma_y^2} \right)}. \quad (2.19)$$

with $od_0 \rightarrow$ fitted peak optical density,
 $x_0, y_0 \rightarrow$ cloud center position in x and y direction,
 $\sigma_x, \sigma_y \rightarrow$ cloud standard deviation;
describes the atoms cloud width.

Replacing this equation in 2.16 stays that the fitted optical density in 2 dimensions gives direct information about the atoms column density distribution (atoms density 2D projection):

$$n(x, y) = \frac{od(x, y)}{\sigma_{abs}} \quad (2.20)$$

In order to extract the total number of trapped atoms, the atoms column density distribution should be integrated and the equation 2.18 becomes

$$\begin{aligned} N &= \int \int \frac{od(x, y)}{\sigma_{abs}} dx dy \\ &= \frac{2\pi \sigma_x \sigma_y od_0}{\sigma_0} \end{aligned} \quad (2.21)$$

Another common characteristic used in the literature for describing an atom cloud is the peak atom density n_0 . This can be calculated as

$$n_0 = \frac{N}{(2\pi)^{3/2} \sigma_x \sigma_y \sigma_z} = \frac{od_0}{(2\pi)^{1/2} \sigma_z \sigma_0} \quad (2.22)$$

Note that in order to calculate this parameter, information about the atoms distribution in z direction is needed.

Absorption imaging in the HAITrap

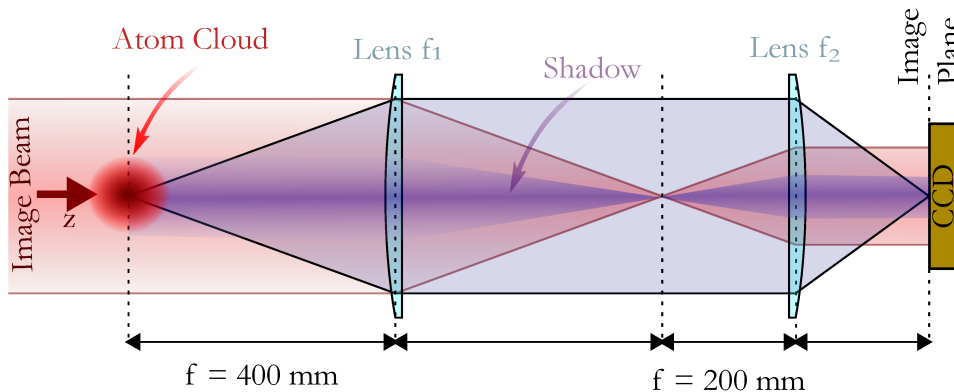


Figure 2.17: Simplified setup of the imaging system for the atom cloud. A laser imaging beam (red) travels in z-direction. Due to absorption, the atoms create a shadow (purple) at the imaging beam. This is imaged via a two lens system with focal length f_1 and f_2 into a CCD camera, which is placed on the image plane.

In figure 2.17 the simplified schematics of the imaging system in the experiment is shown. A more complete scheme of the imaging path can be found in section 2.2.3, figure 2.15. The imaging light is a laser beam (absorbi) prepared as explained in section 2.2.2. It has a Gaussian shape with a beam FWHM of 1 cm. Its intensity as well as the frequency are controlled via an acoustic-optic modulator. For simple absorption imaging, the laser beam frequency is set at atomic resonance ($\Delta = 0$) and its power to $100 \mu\text{W}$. For a Gaussian beam this means a peak intensity of $I_{peak} = 2P/\pi\sigma_{beam}^2 = 0.35 \text{ mWcm}^{-1}$ which is well below I_{sat} .

The laser probe beam is imaged into a CCD camera with a 2 : 1 lens system. Both lenses are plano-convex in order to reduce field curvature effects. In our system, the first lens' focal length was chosen in order to match the distance from the atom cloud to the next place available outside the vacuum chamber. The second lens ensures a 2 : 1 reduction of the image at its focal plane. This is done by using the full CCD chip size as an image plane for the absorption laser's beam shape. The lens system is mounted in a mounting cage (Thorlabs), which is displaceable in z direction for rectifying possible misalignment of the focal plane. This ensures that the image is sharp in the CCD chip plane. This cage provides the further advantage that the lenses are easily adjustable and can be mounted together with the camera in the same axis. For tracking the light intensity we use a calibrated near infrared CCD Camera (Allied Vision Guppy F-038B).

It should be noted, that the characterizations of the ion cloud shown in this section was performed without the presence of the ion trap. This could set a limitation in the number of trapped atoms and dark state fraction because the

2 Hybrid Atom-Ion Trap (HAITrap)

repumping light can be scattered into the trap. Therefore, future experiments should consider a more accurate characterization of the ion cloud.

Typical row data from de CCD camera is shown in figure 2.18. To obtain absorption images of the atom cloud, the laser beams are turned off and a fill-in pulse is shined onto the cloud, which repumps the atoms being in the dark state ($F = 2$) to the so called bright state ($F = 3$). If the fill-in pulse is not used, only atoms that are already in the bright state are detected, which can be used to determine the bright state fraction of the atom cloud. Then, a pulse of the absorption beam is shined onto the cloud (as depicted in figure 2.17) and the image from the CCD camera is stored in the control software. Lastly, an equal absorption beam pulse is triggered in order to measure the reference intensity without the atom cloud. Using each pixel information, the optical density can be computed using the equation 2.14.

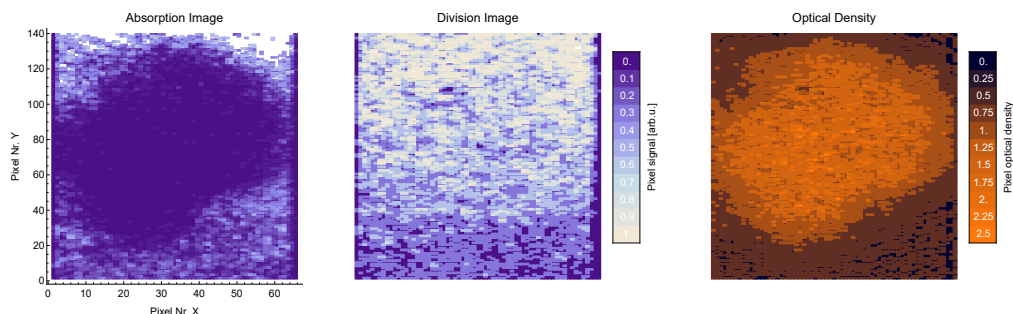


Figure 2.18: Absorption imaging. The left picture shows a typical absorption image of the atoms, whereas the middle picture shows an image of the laser beam without the atom cloud. The right graph shows the optical density of the atom cloud calculated using the equation 2.14.

Saturation absorption imaging

Until now, a two-level system has been assumed for the absorption model. However, in a real system the atoms are distributed over several Zeeman sub-levels. In order to model the absorption of such an atomic ensemble, it is assumed that the atom cloud absorbs the laser light having an effective saturation intensity [90, 89] with

$$I_{\text{sat,eff}} = \alpha I_{\text{sat}}, \quad (2.23)$$

with α being a dimensionless factor that models the distribution of the atom cloud in the different Zeeman sub-levels. As a consequence, the on-resonance absorption cross section (see equation 2.13) has an effective value of

$$\sigma_{0,\text{eff}} = \frac{\sigma_0}{\alpha}. \quad (2.24)$$

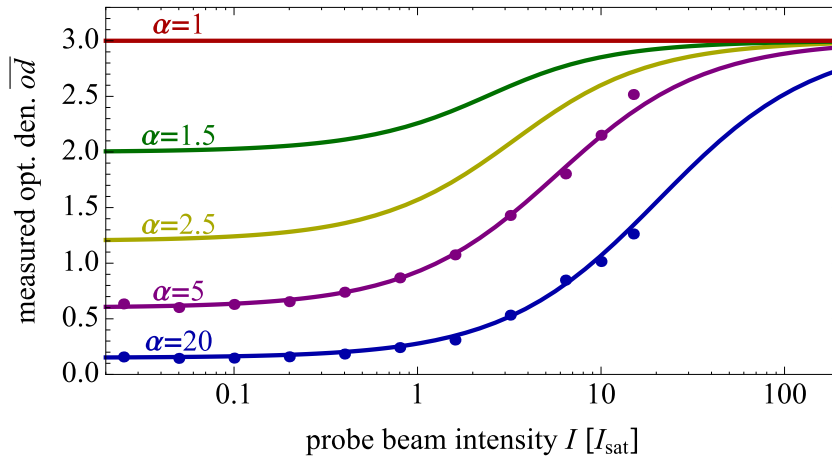


Figure 2.19: Experimental determination of the parameter α . Optical density measured as a function of the absorption beam intensity for different α parameters calculated using the equation 2.25. The points depict two examples of measured data sets with resultant parameter of $\alpha = 5$ and 20 respectively.

Plugging this in equation 2.14 leads to

$$\alpha \cdot \left(1 + 4 \left(\frac{\Delta}{\Gamma} \right)^2 \right) \cdot \ln \left(\frac{I_f}{I_0} \right) + \frac{I_f - I_0}{I_{sat}} = -\sigma_0 \cdot \int n(z) dz \quad (2.25)$$

The two terms on the right side of this equation are the measured optical density \overline{od} . Only the second term depends on the absolute probe beam intensity. For simple absorption imaging, as discussed above, it can be neglected as $I_0 \ll I_{sat}$. With increasing intensity, the second term cannot be neglected anymore. For $I \gg I_{sat}$ the first term can be neglected and the optical density becomes independent of the parameter α . Therefore, the actual atom cloud's optical density can be measured by using large enough beam intensities. Nevertheless, this is not applicable in most experimental realizations. Therefore, in order to measure α , different absorption images are obtained as a function of the beam intensity.

In order to obtain good quality images of the atom cloud, high optical densities should be avoided by reducing the absorption cross section. This can be done by detuning the absorption beam from resonance [91]. For large atomic clouds, it is assumed that the measured shape of the cloud remains unchanged with a given detuning of the probe beam [5].

Figure 2.19 shows the measured optical density \overline{od} , which is calculated assuming $\alpha = 1$, as a function of the probe beam intensity. By fitting equation 2.25 to the data, the actual α parameter can be determined.

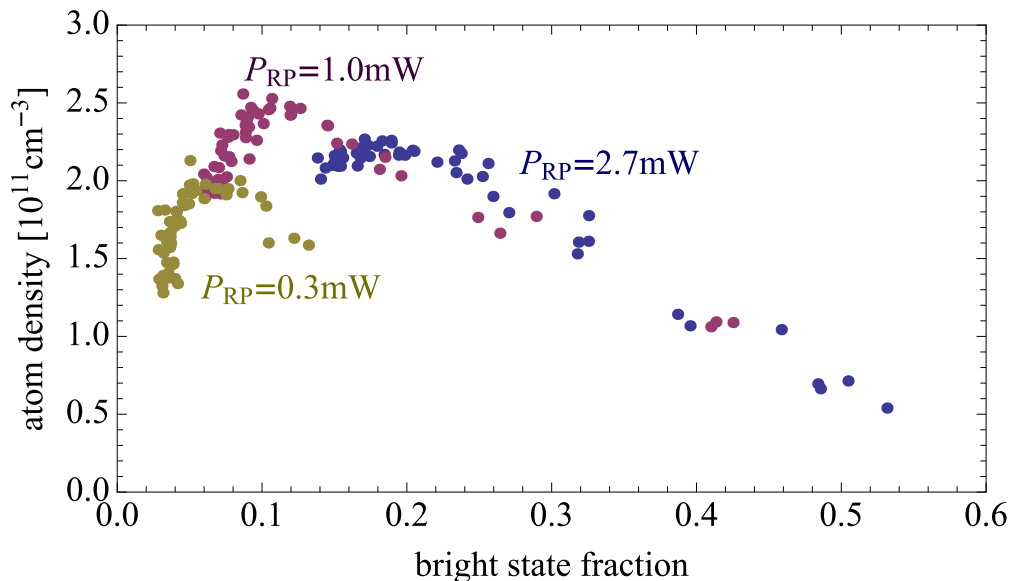


Figure 2.20: Atom density and bright state fraction. Atom peak density as a function of the bright state fraction for different repumper powers (color coded). The bright state fraction was controlled by varying the cooler beam power.

With this information, the atom number N and the peak density n_0 can be determined by

$$\begin{aligned}
 N &= \frac{2\pi \sigma_x \sigma_y \overline{od}}{\sigma_0}, \\
 n_0 &= \frac{\overline{od}_0}{(2\pi)^{1/2} \sigma_z \sigma_0}.
 \end{aligned}
 \tag{2.26}$$

The darkSPOT allows to control the bright state fraction of the atom cloud. This can be achieved by changing the balance between the cooling and repumping beam powers. By increasing cooling power, an atom will undergo more transition cycles per second. The repumping power determines how fast an atom will be repumped to the bright state. Therefore, to achieve low bright state fractions, a high cooling power and a low repumping power are needed. This is depicted in figure 2.20.

To determine the dark state fraction of the atom cloud in the experiment, two different measurements have to be performed. First, the atom cloud is imaged with a fill-in pulse as described above, which provides the total number of atoms in the trap. Then, a second image is obtained without fill-in pulse, which provides the number of atoms in the bright state. The dark state fraction is hence given by the ratio between these two measured number of atoms.

3 Sympathetic cooling of anions by ultra-cold atoms

This chapter presents sympathetic cooling of negative ions in their translational degrees of freedom via elastic collisions with ultra cold atoms in our hybrid atom-ion trap. For this aim, we analyze in section 3.1 the types of collisions that can take place in hybrid traps, namely reactive, elastic and/or inelastic collisions between ions and atoms, with special scope on the system $\text{OH}^- + \text{Rb}$. Specifically, the characterization and experimental control of reactive collisions in this system are discussed in section 3.1.1. Afterwards the elastic collision dynamics of single ions with atoms inside a hybrid trap with different ion trap geometries and mass ratios is analyzed in section 3.1.2. Based on this, the expected final ion energy distributions for different ion trap geometries, mass ratios and specifically for our HAITrap are presented in section 3.1.3.

In this work, two different motional thermometry techniques were used and compared to each other. These methods allow sympathetic cooling of the ions' translational degrees of freedom via elastic collisions with the ultra cold buffer gas. The first method, presented in section 3.2, is based on tomography measurements of the ion cloud using photodetachment of the anion's electron. The second method, presented in section 3.3, is based on precise measurements of the ion time of flight distributions.

3.1 Neutral-ion collisions inside a hybrid trap

Hybrid trap systems are an elegant tool for experimental studies on several types of atom-ion collision dynamics. This section describes different collisions between ions and atoms that take place in hybrid traps, namely *reactive*, *elastic* and/or *inelastic* collisions.

- **Reactive collisions.** A reactive collision, or chemical reaction, is an interaction process that results in the transformation of the colliding partners into other chemical species [92]. In hybrid traps this implies that reactive collisions between ions and atoms lead to either ion losses from the trap or to the transformation of the trapped ion into other kind of ion. Both cases can be easily monitored in a hybrid trap.

In our atom-ion system, several reactive collision channels are open:



The reactions 3.1b and 3.1a are called associative detachment and are the most prominent reactive collisions in the system. These channels have different reaction cross sections. The reaction 3.1c is called charge transfer. Here, the anion's electron is relocated in the neutral partner during the collision. This constitutes an open channel only if the neutral partner is in the excited state.

On basis of controlling these chemical reactions in the HAITrap, it is possible to enhance the number of elastic collisions, which are fundamental for sympathetic cooling. An overview of reactive collisions in hybrid traps, and specially in our system, is given in section 3.1.1.

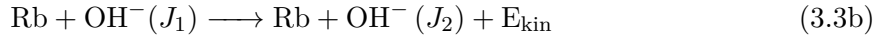
- **Elastic collisions.** An elastic collision takes place when the colliding particles exchange only kinetic energy with each other. Thereby the ion changes its kinetic energy from E_{kin1} to E_{kin2} :



If the ion loses kinetic energy after the collision ($E_{kin2} < E_{kin1}$), the process leads to sympathetic cooling of the anion. For cooling an ensemble of anions this kind of collisions need to be favored in the experiment. Nevertheless, inside a radio frequency trap it is possible, that the ion gains energy after a collision ($E_{kin2} > E_{kin1}$) even if the atom is at rest in the laboratory frame. The dynamic of such collisions inside a hybrid trap are detailed in section 3.1.2. This allows the development of an experimental strategy for enhancing collisions where the ion loses its kinetic energy. The experimental realization and demonstration of sympathetic cooling will be shown in sections 3.2 and 3.3.

3 Sympathetic cooling of anions by ultra-cold atoms

- **Inelastic collisions.** An inelastic collision happens when there is an interchange between the kinetic and the internal energy of the colliding particles [92]. Specifically in our system following inelastic collision channels are possible:



In the channel 3.3a the rubidium atom is de-excited after the collision, whereby its excitation energy can be transferred to the colliding particles as kinetic energy. This can lead to heating or loosing the anion since it can no longer be trapped in the confining potential of the octupole trap.

Similarly, the channel 3.3b refers to a collision where the molecular anion being in a rotational state J_1 is excited or de-excited to another rotational state J_2 . Collisions where the anion is de-excited ($J_2 < J_1$) allow for rotational quenching of molecular ions. This will be described in detail in chapter 4.

The most important parameters to describe the dynamics of these type of collisions are their cross section and rate constants. The so called capture model is an established tool for estimating these parameters [93]. It is based on Langevin's theory for atom-ion interactions [94].

In this model, the effective interaction potential between an ion and a neutral atom is given by an attractive term (charge-induced dipole $\propto -r^{-4}$) and a repulsive term (centrifugal $\propto r^{-2}$) [95]. The shape of such interaction potential has a maximum (known as the centrifugal barrier) that depends on the impact parameter b and the collision velocity v .

There is a critical impact parameter b_c , for a given collision energy, where the trajectory of the particles after the collision is described by an orbit around the scattering center with a constant atom-ion separation [96]. In this model, the probability for a Langevin collision is $p = 1$ for $b \leq b_c$, and the collision does not occur ($p = 0$) for $b > b_c$.

The critical impact parameter is also used to define the so called Langevin cross section similar to the hard-sphere collision model:

$$\sigma_L = \pi b_c^2 = \pi \sqrt{\frac{4\alpha e^2}{\mu v^2}} \quad (3.4)$$

with α being the polarizability of the neutral, e the elementary charge and μ the reduced mass of the atom-ion system. As can be seen in this equation, the cross section depends inversely on the relative velocity of the colliding ion-atom pair. Hence, the collision rate constant for this process is independent of the relative collision velocity:

$$\kappa_L = v\sigma_L = 2\pi e \sqrt{\frac{\alpha}{\mu}} \quad (3.5)$$

3 Sympathetic cooling of anions by ultra-cold atoms

The Langevin model is often used in the literature to compare it to more detailed models for atom ion collisions as it is a good estimation for the total collision rate of the system. For $\text{Rb} + \text{OH}^-$ the obtained rate constant is $4.1 \cdot 10^{-9} \text{cm}^3 \cdot \text{s}^{-1}$.

In the following we aim to analyze this kind of collisions in more detail. On basis of this knowledge we estimate the feasibility of sympathetic cooling in our HAITrap for the system $\text{Rb} + \text{OH}^-$.

3.1.1 Reactive collisions

Although a detailed study on reactive and inelastic collisions is not the central scope of this thesis, in this section we aim to give a brief overview on this exciting research field, which has attracted a lot of attention to a whole scientific community since decades. Atom-ion reactive collisions at very low temperatures are of special interest since the wave nature of the colliding particles lead to non-classical stochastic reaction effects [7, 16]. This research area offers not only fundamental understanding of this type of collisions but also a vast range of applications, for example in quantum control of chemical reactions [97, 98, 99] or in quantum computing [100].

Moreover, it is important to characterize the possible ion losses due to chemical reactions, as they set a natural limitation for sympathetic cooling for ions in radio frequency traps [97].

Reactive collisions in hybrid traps

Hybrid atom-ion systems are an excellent tool for the study of reactive collisions between atoms and ions in a very well-controlled environment [17, 18, 19].

[101, 99] To mention a few examples, single $^{174}\text{Ba}^+$ and $^{87}\text{Rb}^+$ ions were overlapped with a Rb Bose-Einstein condensate (BEC) [102]. Thereby charge transfer reactive collisions were observed and analyzed. As an application the ions were used to probe the spatial distribution of the atom cloud. Similarly, charge exchange was observed in systems with a single Yb^+ ion overlapped with a Rb BEC [103] and also between $\text{Yb}^+ + \text{Yb}$ in a magneto optical trap [104].

Nevertheless, as already pointed out in the introduction, studies on reactive channels in hybrid trap systems have been carried out mostly on positive charged ions (cations), the only exception being the work in our group on the system $\text{OH}^- + \text{Rb}$ [15]. Our system is to date the only one in the world capable of mixing negative charged ions (anions) with an ultracold cloud of neutrals, opening a whole new experimental branch in quantum chemical physics. In this work we choose the molecular anion OH^- as the first test anion for several reasons already discussed in the introduction.

Reactive collisions in the system $\text{OH}^- + \text{Rb}$

As mentioned before, this system can react in different ways (see collision paths 3.1), being associative detachment the dominating reaction channel. Using the

3 Sympathetic cooling of anions by ultra-cold atoms

Langevin theory of atom-ion collisions (equation 3.4) for estimating this cross section would mean that each collision of such type lead to a chemical reaction of the colliding particles. Consequently, this model provides an estimation for the upper limit of this collision rate.

More sophisticated models are based on the numerical computation of the potential energy surfaces of the colliding and outgoing particles by taking into account their internal structure, in our case the interaction potential curves of $\text{Rb} + \text{OH}^-$ and the neutral products $\text{Rb} + \text{OH}$. In this model, it is stated that a chemical reaction takes place when the system has enough energy to reach the region where both potential curves cross each other, i.e. in our case the region of nuclear coordinates where the relative energy is $E_{\text{Rb}+\text{OH}^-} < E_{\text{Rb}+\text{OH}}$. This region is called the auto-detachment region.

The calculation of such energy surfaces and hence their crossing points depend on the numerical method applied and the internal structure. A key ingredient in this calculation is given by the approximation of the effective core potentials of each particle describing their core electrons. For the system $\text{OH}^- + \text{Rb}$ two independent calculations have been reported [105, 106]. Nevertheless, these calculations dropped quantitative different results due to the use of different core potentials. The main difference between these two works is the OH^- internal state for which the associative detachment reaction takes place. In [105] it was reported that associative detachment is open only if OH^- is in at least its second excited vibrational state, whereas in [106] this reaction happens already for the OH^- vibrational ground state.

In figure 3.1 a 1D cut of the calculated potential surfaces calculated in [106] are shown. This cut corresponds to a collision angle of zero degrees i.e. Rb approaching OH from the oxygen side of the molecule. The potential energy for rubidium hydroxide ($\text{Rb} + \text{OH}$) is shown in orange and the one for $\text{Rb} + \text{OH}^-$ in dark green, the last one being the entrance channel for the associative detachment reaction. As discussed before, when both curves exhibit a crossing point in the negative energy region, associative detachment takes place [106]. This is marked as a black circle. Similarly, an example of an entrance channel for rubidium in the excited state is shown in bright green, showing a crossing point near the one in the ground state rubidium case.

A further analysis on these collisions calculations shows that the potential crossing points depends on the collision angle between the two particles. For example, when rubidium is approaching the molecule from the hydrogen side, associative detachment should not take place. Effectively, the accessible angular space for this collision to happen depend highly on the collision energy and hence the particle temperatures. Following this reasoning, the final rate constant for associative detachment is the Langevin rate times the accesible angular space, which is found to be around 0.1. In consequence, for the atom being in its ground state, about 10% of the collisions lead to associative detachment.

In contrast, if the atom is in the excited state (see reaction path 3.1b), additional term effects have to be taken into account. In this case, the accessible angular space for the reaction is found to be drastically larger as in the case for

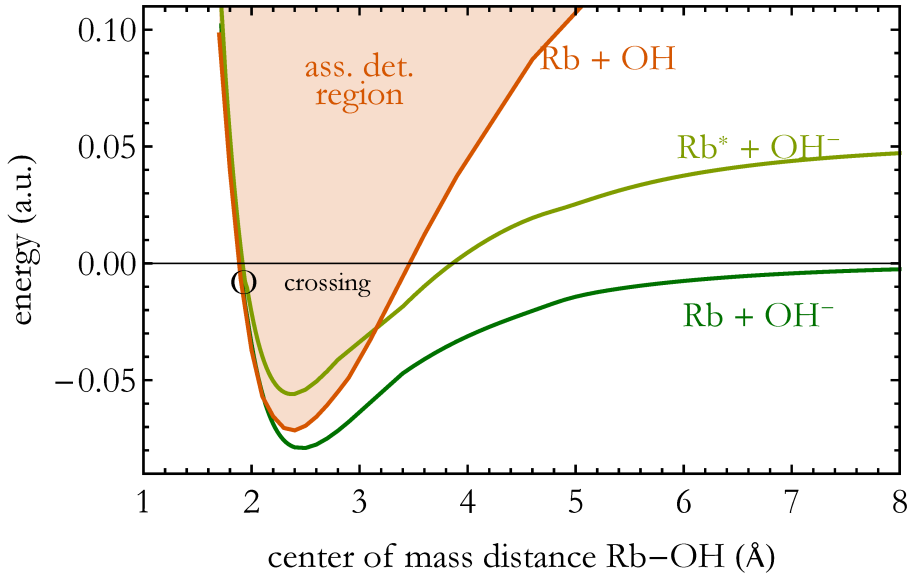


Figure 3.1: Potential energy curves for $\text{OH}^- + \text{Rb}$. The interaction potential energy of the colliding partners is plotted as a function of their distance. Two examples of entrance channels are plotted in green, whereas the molecular potential energy of rubidium hydroxide is plotted in orange. The black circle indicates the crossing points of the potential curves, which is an estimation for associative detachment. Details for the calculation of these curves can be found in [106]

ground state rubidium, namely about 90% of the collisions lead to associative detachment.

A further interesting aspect from the results of this calculations is the fact that in this case (Rb in excited state), a small part of the angular space may lead to charge transfer (see reaction path 3.1c). This channel is found to be roughly 400 times weaker than the Langevin rate constant.

These results have direct implications for the prospects of sympathetic cooling. These theoretical estimations and previous measurements on this system [15] suggested that the best configuration for sympathetic cooling in the system $\text{OH}^- + \text{Rb}$ is to use a dark spot with the highest dark state fraction possible.

Furthermore, it is of great interest to experimentally reperform the measurements done in [15] in our new generation hybrid trap. In our experiment we are able to control the fraction of the atoms that are in the excited state, and therefore perform a measurement on the collision rates that lead to chemical reactions as a function of the internal state distribution of the atoms.

Reactive collision losses in our HAITrap

As discussed above, the chemical aspects of the system $\text{OH}^- + \text{Rb}$ are on the one hand of great interest for chemical physics, but on the other hand for sympathetic cooling it is important that only elastic collisions take place. Reactive collisions in our system are unavoidable. Therefore, this section characterizes the losses due to inelastic and reactive collisions inside our hybrid trap. For this, we performed a measurement of the loss decay rate as follows.

After the ions are generated (section 2.1.2), they are mass selected and loaded into the thin-wire 8-pole trap (section 2.1.3), where they first thermalize with a pulse of helium buffer gas at 300 K. The loaded number of ions is limited for this experiment to a mean of about 30 ions per experimental run in order not to saturate the channeltron detector (section 2.1.4). Once they are trapped, the voltage applied to the compensation electrodes of the ion trap is ramped down in order to ensure optimal overlap of both clouds. During this process, which takes about 5 seconds, a laser at 780 nm is shined into the trap in order to detach O^- , such that just OH^- ions remain trapped. This time is also used for pumping out the remaining He buffer gas. At this point the pressure of the main chamber drops down to 4.5×10^{-9} mbar, which is enough to effectively load the dark spot. Rubidium is afterward loaded and after a certain interaction time, the remaining ions are extracted and counted.

Figure 3.2 show the results for the reactive collisions losses occurring inside the hybrid trap. The purple points show the case where the ions did not interact with the Rb cloud. In this case, the ions are lost because of background collisions (see figure 2.14). For the other cases, at time $t = 0$ rubidium is loaded in the dark-SPOT in different dark state configurations (see figure 2.20). Therefore, the observed losses are attributed to be caused mainly by associative detachment. One observes, that the higher the bright state, the faster are the ion losses.

The decay constant for this case is $\kappa = 0.29 \text{ s}^{-1}$.

Since our setup allows us to tune the dark state fraction of the atom cloud very precisely, a more systematic measurement will be done in near future in order to clarify the ongoing discussion on associative detachment in the system $\text{OH}^- + \text{Rb}$ [105, 106].

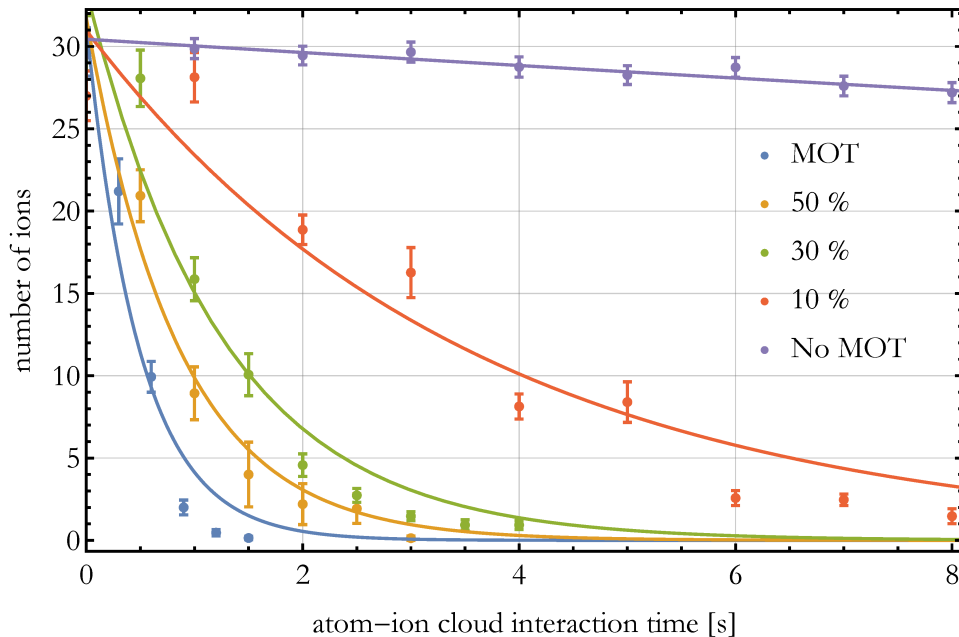


Figure 3.2: Ion losses due to reactive collisions for different bright state fractions. The detected number of ions is plotted as a function of the atom-ion interaction time for different darkSPOT configurations. The purple points show the intrinsic ion loss from the trap where no atom cloud is present. When the Rb atoms are present, the ion losses depend on the bright state fraction (marked with different colors). The solid lines show an exponential fit to the data.

3.1.2 Elastic atom-ion collision dynamics

It is well known from classical thermodynamics that if a gas A is put into a gaseous thermal bath B of temperature T_B , the gas A 's temperature will reach thermal equilibrium with its energy reservoir B . The fundamental process behind the thermalization are the elastic collisions between both gases. For the case of cooling, the particles of gas A lose their kinetic energy after elastic collisions with those of B until A reaches thermal equilibrium with B at $T = T_B$.

Nevertheless, this picture is not entirely true for the case of radio-frequency stored ions being cooled by an atom cloud at low temperatures. In such systems, the ions can increase its kinetic macro-motion energy after an elastic collision, even if the atom cloud is at 0 K. The reason for this counter-intuitive effect has to do with the intrinsic motion of the trapped ions.

As seen in section 2.1.1, the trajectory of an ion stored in a radio-frequency trap can be described by two motions: i) the micro-motion, which is a fast oscillation caused by the radio-frequency field and ii) the macro-motion, which is a much slower motion, can be interpreted as a motion of an ion at a given temperature inside an effective confining (ponderomotive) potential. The storage

of the ion in the trap is based on an exchange of energy between these two motions. Elastic collisions alter this interplay, resulting in an energy transfer from the micro- to the macromotion. This is exemplified in figure 3.3.

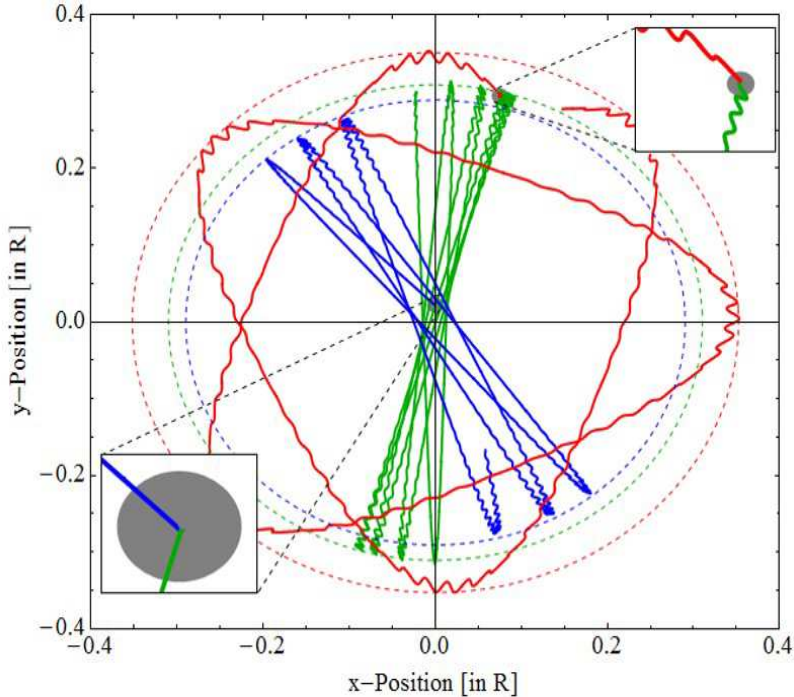


Figure 3.3: Ion trajectories before and after a collision at different radial positions. Shown are 2D projections from trajectories of an ion stored in an rf trap. The green curve shows the trajectory for a given ion energy. After a collision near the center of the trap (blue trajectory) the ion loses energy, whereas if the collision takes place in the trap’s outer region, the ion gains energy.

This phenomenon, called collisional heating, has been subject to many theoretical studies over decades [107, 14, 20, 21, 22, 23]. One of the major outputs of these theoretical findings was the estimation of the natural limitation for this technique: for being able to cool down trapped ions stored in a radio frequency trap via sympathetic cooling with an atom gas, one has to choose in the experiment the atom to ion mass ratio $\xi = m_a/m_i$ below a critical value, which is estimated to be around unity.

As stated in the introduction of this chapter, already in 1995 Gerlich had an intuition for avoiding the cooling limitation set by collisional heating in rf traps [7]. His idea was to use a laser cooled atom cloud as a buffer gas and localize it in the center of the ion trap, such that elastic collisions between atoms and ions happen where the ions have almost no micro-motion. Yet, theoretical studies mentioned earlier were limited by two assumptions: i) the ions are stored in a 4-

3 Sympathetic cooling of anions by ultra-cold atoms

pole rf trap, known as linear Paul trap, and ii) the buffer gas fills homogeneously the entire ion trap.

Hence, a realistic theoretical framework for modeling the dynamics of an n-pole rf-trapped ion immersed in a spatial-localized buffer gas cloud of atoms was missing. This motivated our group to extend the theoretical studies mentioned earlier in order to take into account the pole order of the ion cloud and the localization of the buffer gas [24, 25].

The assumptions of our model are:

- The ion is stored in a cylindrically symmetric trap with $2n$ radio frequency electrodes, where n is the trap order. Axial confinement is not taken into account.
- The ion undergoes exclusively elastic collisions with atoms.
- The micromotion oscillation frequency is much faster than that of the macromotion. This is known as adiabatic approximation.
- The duration of a collision is much shorter than one macromotion oscillation period. This implies that the micromotion remains unchanged during the collision.

With these assumptions it can be shown via conservation of energy and impulse that the macromotion velocity after a single elastic collision is (see supplementary material in [24])

$$\vec{u}'_i = \frac{m_a}{m_i + m_a} R(\theta_c, \phi_c) (\vec{u}_i - (\vec{v}_a - \vec{v}_i)) + \frac{m_i \vec{u}_i + m_a (\vec{v}_a - \vec{v}_i)}{m_i + m_a} \quad (3.6)$$

- with
- \vec{u}_i, \vec{u}'_i → ion's macromotion velocity before/after collision;
 - \vec{v}_i → ion's micromotion velocity during collision;
 - \vec{v}_a → atom's velocity before collision;
 - m_i, m_a → ion, atom mass;
 - $R(\theta_c, \phi_c)$ → Rotation matrix with polar and azimuthal scattering angles respectively;

Here, the micromotion velocity can be described as

$$|\vec{v}_i(r)| = \frac{eV_0}{\omega R_0} \cdot \frac{n}{m_i} r^{n-1} \cos(\Phi_{rf}) \quad (3.7)$$

- with
- r → ion's radial position;
 - n → trap order;
 - e → elementary charge;
 - V_0 → radio frequency voltage;
 - ω → angular radio frequency;
 - R_0 → trap's inner radius;
 - Φ → radio frequency phase

3 Sympathetic cooling of anions by ultra-cold atoms

In order to characterize the kinetic energy difference of an ion before and after a collision, we can calculate

$$\Delta E_i = \frac{1}{2} m_i (\vec{u}_i'^2 - \vec{u}_i^2). \quad (3.8)$$

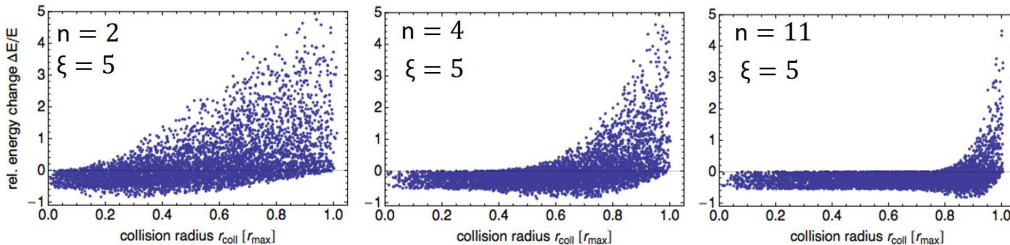


Figure 3.4: Monte Carlo simulations of the ion’s relative energy change after an atom-ion collision as a function of the collision’s position for different trap orders. The traps geometrical center is at $r_{col} = 0$. The collision radius axis is normalized by the maximal radius r_{max} an ion can reach at the given energy E . Each point represents one collision of an ion at fixed energy E with an atom at rest ($T_a = 0$). Their mass ratio is $\xi = 5$, as is the case for our experiment. About 10^4 collisions are shown. When the collision happens in the outer part of the trap, the ion can gain many times over its initial energy ($\Delta E > 0$), leading to collisional heating. In contrast, the ion loses energy ($\Delta E < 0$) near the trap’s center, leading to sympathetic cooling. The region inside the trap where the ion loses energy after a collision increases with increasing pole order n due to the absence of micromotion in the central region of higher order traps.

Using equations 3.6 to 3.8 we can now give an intuitive picture of the energy transfer in collisional heating. For this we look at the dependency of an ion’s relative energy change after an elastic collision as a function of the collision position, characterized by the collision radius r_{coll} . Hereby, we assume the ions to have a fixed energy E and the atoms to be at rest ($v_a = 0$). Therefore, in this example, the energy change after an elastic collision is only given by the coupling to the energy reservoir provided by the radio frequency field. Furthermore, we choose their mass ratio to be $\xi = 5$ as is the case for our experiment.

In figure 3.4 the results of this analysis is given for different trap orders. A convenient normalization for the collision radius is the geometrical turning point of the ion with energy E inside the effective confining potential. Each point represents one collision. A set of about 10^4 collisions are plotted for each trap order.

As one clearly sees from the figure, if the collision happens in the outer part of the trap (near r_{max}), the ion can gain many times over its initial energy ($\Delta E > 0$), leading to collisional heating. In contrast, the ion loses energy ($\Delta E < 0$) near the trap’s center, leading to sympathetic cooling. This fact is given by the fact that the micromotion’s amplitude in the central region of

3 Sympathetic cooling of anions by ultra-cold atoms

radio frequency traps cancels out (see equation 3.7). As a consequence, the region inside the trap, where the ion loses energy after a collision, increases with increasing pole order n . For example, at exactly the traps center ($r_{col} = 0$), the ion's micromotion is zero. Therefore, an ion at this position colliding with an atom at $v_a = 0$ can only lose energy after such an elastic collision.

Following this analysis in a more general way, we can find two critical parameters [24, 25]:

- **Critical mass ratio.** As mentioned before, there exists a critical mass ratio for which sympathetic cooling in a Paul trap is achievable. By averaging the ions energy change (equation 3.8) over one radio frequency period and stating that the average energy transfer has to be zero, we find the critical mass ratio to be pole-order dependent:

$$\xi_{crit} = \frac{3}{2}(n - 1) \quad (3.9)$$

Note that this definition holds for a buffer gas filling out the whole ion trap. However, the most prominent consequence of this fact is that the mass ratio limitation for sympathetic cooling can be overcome by using a sufficiently high pole order n . In the case of our experiment (8-pole rf trap), this would result in a $\xi_{crit} = 4.5$, which is lower than the mass ratio of our system. Nevertheless, one has to take into account that our buffer gas is spatially localized, which leads us to the second critical parameter:

- **Critical collision radius.** Given the fact that the energy change is positive (heating) or negative (cooling) depending on the position of the collision, we can define a critical collision radius where the net energy transfer within this radius is positive for $r_{col} > r_{crit}$ or negative for $r_{col} < r_{crit}$. It can be shown that this radius is given by

$$r_{crit} = r_{max} \left(\frac{1 - \frac{3}{2}k_B T_a / E_i}{1 + \xi} \right)^{1/(2(n-1))} \quad (3.10)$$

with T_a being the temperature of the atom cloud. By localizing the buffer gas within this radius, sympathetic cooling of ions becomes feasible even for mass ratios far beyond the critical value ξ_{crit} .

In our experiment we combine the advantages of these two critical parameters: the use of an 8-pole ($n=4$) radio frequency trap and a localized buffer gas realized by means of a magneto optical trap.

In this analysis we have just considered the atoms to be at rest. This is of course a simplification of the real experimental scenario. In the following we aim to give an overview of the final energy distributions expected in a hybrid trap for different trap orders and mass ratios.

3.1.3 Final energy distributions

In order to model the final energy distributions of a single rf-stored ion interacting with a neutral buffer gas cloud at a given temperature, we have first to model the thermalization process of the ions with the atoms. Hence, we have to calculate consecutive atom-ion collisions until the ion attains a stable (steady-state) energy distribution.

This is done making three assumptions:

- For modeling the elastic atom-ion collision rate we use the Langevin interaction theory. As already discussed (see equation 3.5), this model yields a good estimate for the probability per second that an ion collides with an atom depending only on the atom cloud's density. Furthermore, the fact that this collision rate constant is energy independent makes it a convenient tool to use for our model.
- For modeling the energy change after a collision, we make the adiabatic approximation for the ion's motion. We assume that the micromotion oscillation frequency is much faster than that of the macromotion. In other words, we limit our model to small stability trap parameters η (see section 2.1.1). In this way, in case of a collision, we can compute the relative energy change as showed in the last section (equation 3.8). This assumption is valid for most of the experiments using ion traps.
- We assume low atomic densities, such that the time period between two consecutive collisions is much longer than one macromotion period. Hence, it is possible (and more convenient) to describe the ion dynamical properties by the ion's radial probability distribution $\rho_i(r, E, L)$ rather than calculating the ion's exact trajectory. This optimizes computing time for the simulation of multiple consecutive collisions.

In base of this assumptions and the relative overlap of the buffer gas and ion density distributions, we can calculate the probability of a collision to happen at a given ion position r . Our algorithm to calculate stable final energy distributions works as follows.

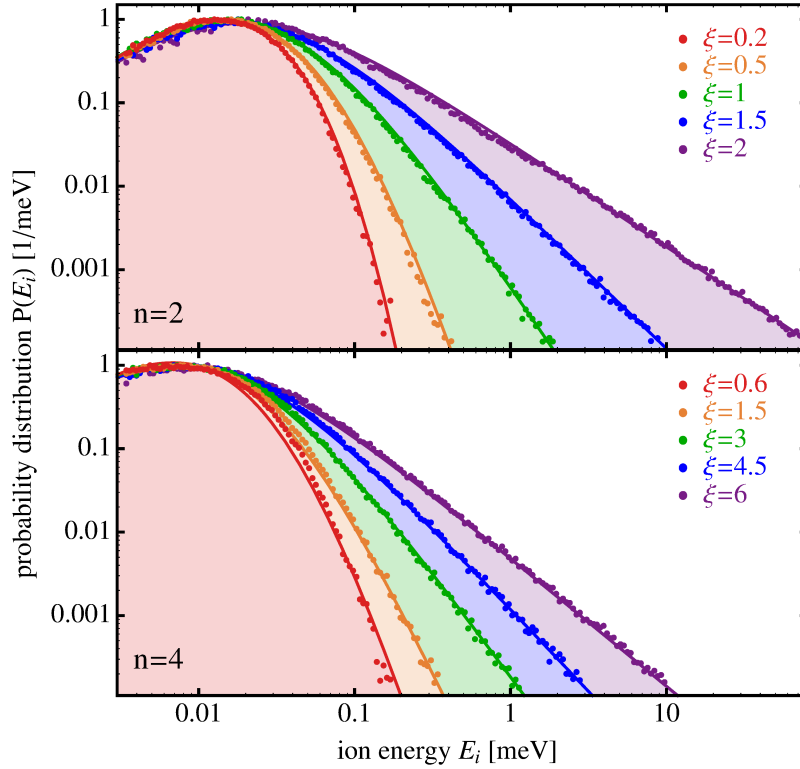


Figure 3.5: Final ion energy distributions for different pole orders n and mass ratios ξ . Top: Paul trap ($n = 2$). Bottom: Octupole trap ($n = 4$). The points are the results of the numerical simulations explained in the text and the solid lines are a fit to the data using a Tsallis function (equation 3.11). The higher the mass ratio, the higher is the power law towards higher energies in both cases. Yet for $n = 4$ the power tails are lower compared with than that of $n = 2$ for equal mass ratios.

Algorithm for consecutive collisions

For the atoms we assume a Boltzmann velocity distribution and a spatial normal distribution. The ion's initial conditions (total energy E and angular momentum L) are arbitrary chosen. The final energy distributions are namely independent of the choice of these initial conditions as long as a sufficiently large number of collisions take place.

With these initial conditions, we start the algorithm with one collision randomizing following parameters: radio frequency phase, incident angle, atom velocity according with a Boltzmann distribution, collision radius according to $\rho_i(r, E, L)$ and scattering angle according to Langevin (isotropic). By means of the equation 3.8 the new macromotion velocity is calculated. Based on this and the collision radius, the new ion's energy and angular momentum after the collision are computed, stored and used as the initial condition for the next collision. We simulate $\approx 10^6$ consecutive collisions as listed above.

For computing the steady-state energy distribution, we analyze the obtained collision data as follows. First, we have to take into account the average time τ an ion spends at a given E and L before new collision takes place. This free mean time is calculated with equation 3.5, which is weighted with the relative overlap of atom and ion distributions. Every computed energy value is weighted with the value of τ . Finally, the weighted energy values are binned, resulting in the required final energy distribution.

In our publications we make a complete analysis on different stable energy distribution regimes observed in our simulations [24, 25]. In this work we aim to focus on the equilibrium regime our experiment is operated in.

Energy probability distributions

In order to compare the effect that different experimental parameters have on the final energy distributions, here we aim to give a set of examples for energy values numerically computed with the algorithm discussed above.

Two trap geometries are chosen as example (see figure 3.5): a Paul trap ($n = 2$) and an octupole trap ($n = 4$). For each geometry, different mass ratios are chosen (see legend). The final (binned, time weighted and normalized) energy values are shown as color-coded points for different mass ratios. We interpret this as the final energy probability distribution of a single ion stored in an rf-trap interacting with a buffer gas. For this examples, we choose the case of a buffer gas homogeneously filling out the whole volume of the rf-trap.

For a further analysis of the numerically obtained energy distributions, we fit the data by a Tsallis function of the form

$$P(E_i) \propto \frac{E_i^{1/2+1/(n-1)}}{[1 + aE_i/(k_B T_a)]^b}, \quad (3.11)$$

with a and b being two free parameters. For $b \rightarrow 0$ this function becomes a Maxwell-Boltzmann energy distribution and for larger b parameters, the energy distribution shows a power law tail (E^κ) towards large energies. This kind of

3 Sympathetic cooling of anions by ultra-cold atoms

Tsallis functions have been also used in the literature on sympathetic cooling in rf-traps [20, 21, 108].

Let us compare the case for very small ratios (red solid lines and points). Equation 3.11 is fitted to the numerical data, yielding a value of $b \rightarrow 0$ for both trap orders. Therefore, the ions final energy distribution is well described by a Maxwell-Boltzmann energy distribution. The corresponding final temperature of the ion matches the temperature of the atom cloud T_a .

With increasing mass ratio, the parameter b in equation 3.11 increases and the energy distribution differs further from a Boltzmann distribution. The exponent of the power law tail (E^κ with $\kappa < 0$) also increases towards 0. This effect is a direct consequence of the collision induced heating discussed before, as it critically depends on the mass ratio (see equation 3.6).

The blue curves show the case of the critical mass ratios for the respective trap orders (equation 3.9). This is $\xi_{crit} = 1.5$ for $n = 2$ and $\xi_{crit} = 4.5$ for $n = 4$. Their fit curves have a power law exponent of ≈ 2 towards higher energies, which matches our analytical result from equation 3.9.

Furthermore, one can show that for a $\kappa \geq -2$ the mean energy of the ion diverges and therefore it can escape the trapping potential equation 3.9. Consequently it is not possible for the last case to calculate an steady-state energy distribution.

By comparing this effect as a function of the trap geometry ($n = 2$ and $n = 4$), one clearly sees: the higher the trap's pole order, the higher the mass ratios that can be used in the experiment in order to become steady state distributions.

Our HAITrap

From the last section, one could possibly argue that despite the use of an octupole rf-trap, it should be not possible to achieve stable final energy distributions for a mass ratio of $\xi = 5$, for $\text{OH}^- + \text{Rb}$. Nevertheless, one has to take into account that our buffer gas is spatially localized in the center of our rf-trap. As a result of this, the power law at higher energies is interrupted because the extreme energy gain collisions become less probable (see figure 3.4).

In order to predict the final energy distributions in our HAITrap, we performed a simulation as explained before in this section. We load thereby the geometry of our trap and the proper mass ratios in our simulation algorithm. The results of these simulations are shown in figure 3.6.

In our experiment, as explained in section 2.1.3, it is fundamental for the trapping procedure that the ions interact with a buffer gas pulse. Therefore, we first simulate the thermalization process of the ions interacting with a Helium buffer gas filling out the whole trap's volume. The results of the simulations are shown in the left graph of figure 3.6 as green dots. For comparison, the thermal energy distribution of the buffer gas at 300 K is also shown. As stated before, a general probability distribution for ions inside a rf-trap is given by a Tsallis function (equation 3.11). Therefore, we fit this function to the data, which results in a very similar probability distribution as a thermal distribution.

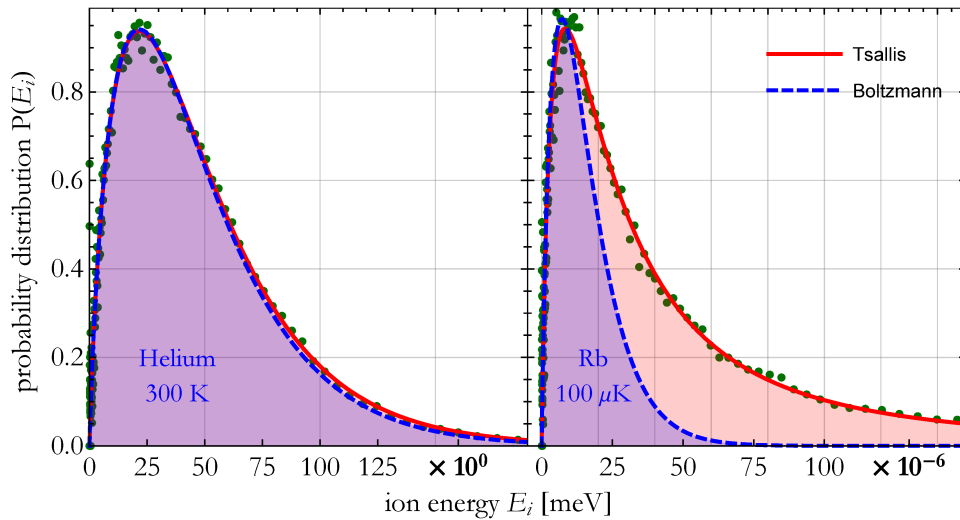


Figure 3.6: Final ion energy distributions in our HAITrap for the different buffer gases used in the experiment. The green dots show the results of the numerical simulations. The dashed blue line shows the Boltzmann energy distribution of the buffer gas.

Left graph: Helium was used as a buffer gas at 300 K, which homogeneously fill out the trap’s volume. The red solid line is a fit to the data using equation 3.11. No significant difference is observed between the two energy distributions.

Right graph: Rubidium was used as a buffer gas at 100 μ K, which was localized in the center of the trap. The size of the atom cloud is $\sigma = 1$ mm. In this case, the ions converge to a non-thermal distribution, which is well described by a Tsallis function (equation 3.11).

This means, that the ions inside our trap should be well described by a thermal distribution at 300 K after their interaction with Helium.

In the second simulation, shown in the right part of figure 3.6, we choose rubidium as buffer gas and localize it in the trap’s center with a size of $\sigma = 1$ mm. Again, the thermal energy distribution of the buffer gas at 100 μ K is shown as dashed blue line. In this case, one clearly sees that the ions converge to a non-thermal distribution, characterized by the Tsallis coefficients $a = 3.1$ and $b = 0.57$ (from the fit results). The percentage of the ions that differ from a thermal distribution towards higher energies is about 49%, yet the peak energy probability is in the order of tens of nano electronen volts.

3.2 Thermometry via photodetachment tomography

In this section, we apply the method called *photodetachment thermometry* to show evidence on sympathetic cooling of ions via elastic collisions with a localized rubidium buffer gas. This technique is based on the fact that the ions spatial distribution inside a confining potential is correlated with the energy distribution of the ions, i.e. the higher the ions temperature, the wider is the size of the ion cloud inside the trap. Consequently, by knowing both the trapping potential landscape and the spatial distribution of the ion cloud, one can derive the ions temperature.

In order to gain qualitative knowledge of our trapping potential, we simulate the ion cloud spatial distribution by means of SIMION. The results of this simulation are given in section 3.2.1. The process of imaging the ion cloud and measuring its size inside the rf-trap by means of photodetachment tomography is explained in section 3.2.2. Finally, by applying this imaging method in our experiment, we observe evidence of sympathetic cooling. These experimental results are given in section 3.2.3.

Further details and characterizations of our trap via photodetachment tomography can be found in form of bachelor and master thesis done during the course of this work [65, 66, 67].

3.2.1 Ion density simulations

In [59] our first effort to show sympathetic cooling by using photodetachment thermometry in our HAITrap was reported. Nevertheless, the limitation for observing a clear signature of sympathetic cooling was the use of high voltages (in the order of ≈ 250 V) on the DC compensation electrodes. This was needed in order to slow down the ions that are accelerated in the mass spectrometer (see section 2.1.3). As we will show here in more detail, the consequence of using such high voltages is that a de-confinement potential arises, which pushes the ions out in radial direction. Effectively, this leads the total trapping potential to show pockets in radial direction. Unfortunately, this potential pockets happened to be placed exactly behind the ion trap wires, preventing us to have optical access to most of the ions in the trap. As mentioned in section 2.1.4, in order to overcome this limitation the power supplies of the DC compensation electrodes in our trap were implemented during this work such that we can adiabatically ramp down the voltages.

In this section, we aim to compare the difference between the ion density expected for the potential landscape with high and low DC electrode voltages shown in figure 2.10. In section 2.1.3 we have introduced SIMION, the program we use in this work in order to numerically compute the trapping potentials in our HAITrap. Based on the numerically calculated potential landscapes in SIMION, we analyze the ion cloud shape (or the resultant ion cloud spatial distributions) we expect by means of these simulations.

It is well known, that for a given trapping potential landscape $V(x, y, z)$, the probability of finding a particle $\rho(x, y, z)$ depends only on the temperature T

3 Sympathetic cooling of anions by ultra-cold atoms

of this sample. Assuming a thermal distribution of the ions and neglecting possible interparticle interactions (as Coulomb interaction between ions), this probability can be computed with the Boltzmann factor as

$$\rho(x, y, z) \propto e^{-\frac{V(x, y, z)}{k_B T}}. \quad (3.12)$$

Using this equation, we can estimate the ions spatial distribution for the potentials numerically calculated in SIMION (see figure 2.10). The proportional factor in this equation can be estimated by setting it firstly at 1 (for a single particle) and then integrating the function in all directions. The final normalization factor is given by the inverse of this integral. This provides us a 3D spatial distribution of a single ion. Since we assume non-interacting particles, this equation describes the total shape of the ion cloud.

Nevertheless, as explained in more detail in section 3.2.2, in our experiment we have only access to a 2D projection of the ions distribution (see figure 3.8). Therefore, by integrating the ions 3D spatial distribution in one radial direction, in our case z (see figure 2.9), we obtain a 2D single ion column density distribution.

As stated before, the spatial distribution of the ions depend on the potential shape and their temperature. For a better visualization of this effect and for allowing a direct comparison of these simulations with experimental results, in the following we analyze axial and radial 1D cuts of the ions 2D column density distribution. This is shown in figure 3.7.

The bottom graphs show the resultant ions distributions by using high voltages at the dc compensation electrodes, the potential landscapes of which can be seen in figure 2.10. This use of such voltages is inevitable for the trapping procedure (see section 2.1.3) but have the disadvantage that a radial de-confinement potential arises, leading to potential minima out of the center of the trap. This has a big effect on the final spatial distribution of the ions, as can be seen in the right-bottom figure. The colder the ions, the higher is the ions density near this potential minima. The position and the depth of this pockets depend on the voltages applied on the different electrodes. We observe that the higher the voltages applied, the deeper are this pockets. Unfortunately, this potential pockets happen to be placed behind the ion trap wires (marked as gray zones), preventing us to have optical access to most of the ions in the trap. This limits the sensitivity of a temperature measurement via tomography.

As mentioned before, in order to overcome this limitation the power supplies of the DC compensation electrodes can be adiabatically ramped down. The upper graphs show the resultant ion distributions after such a ramping procedure, i.e. at low dc voltages 2.10.

One important observation from these simulations is that as long as the axial potential has a harmonic shape, the width of the ions spatial distribution in axial direction is correlated with the temperature of the ions as $\sigma_x \propto T$, regardless of the relative height.

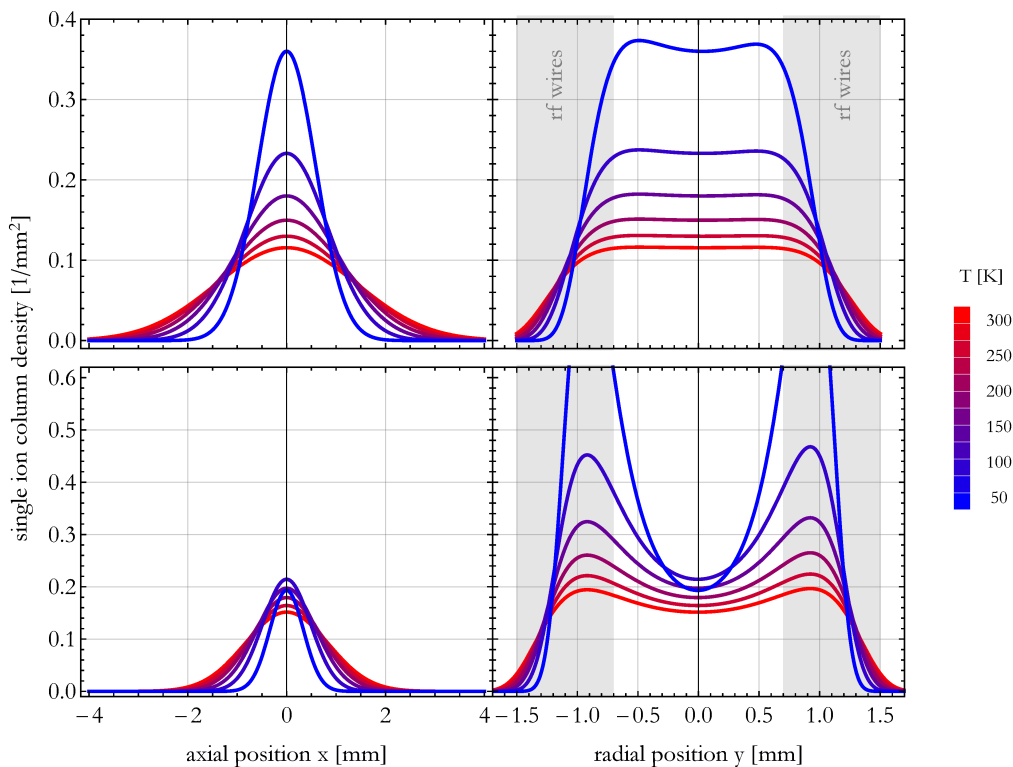


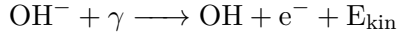
Figure 3.7: Ions spatial distribution for different temperatures and potential landscapes. The single ion column density is plotted as a function of the traps axial direction (left graphs) and radial direction (right graphs) for two different potential landscapes: the upper graphs show the resultant ion distributions for low voltages at the dc compensation electrodes and the bottom graphs for high voltages. The illustrated cuts are done such that they can be directly compared to a 1D tomography scan in both directions. For the definition of the coordinate system see figure 2.9. For the exact shape of the potential landscapes see figure 2.10.

3.2.2 Ion cloud imaging via PD tomography

From section 3.2.1 we have learned that the spatial information of the ion cloud can be used for measuring relative temperature differences of the ion cloud (see figure 3.7). A wide used method for measuring the size of the ion cloud is to excite the ions by means of a laser and image the fluorescence from the ions on a CCD chip. Nevertheless, most of the negative ions cannot be imaged in this way, since they lack on closed transitions, making it difficult to detect the fluorescence, if any, from such ion samples.

Therefore, one has to find a different approach for for imaging the ion cloud and measuring its size inside the rf-trap, even if it is "invisible" for a CCD detector. Photodetachment can be applied as a tool for such an alternative method [109, 53, 110]. The method takes advantage on the fact that ions get lost from the trap when interacting with a laser beam at the right wavelength. The interaction strength between the ions and the laser, characterized by their photodetachment cross section, depends among others on the spatial distribution of the trapped ions and its geometrical overlap with the laser beam. Therefore, the higher the single ion column density, the higher the decay rate from the trap due to photodetachment. Consequently, measuring the photodetachment decay rate as a function of the position of the laser beam gives information on the geometry of the ion cloud.

For modeling this more accurately, let us first analyze the interaction of an OH^- ion cloud with a laser field. The single process



occurs in our trap at a certain rate depending on several experimental parameters: the laser frequency, its power, the ions rotational state J'' and the geometrical overlap between the ion cloud and the laser beam.

For this experiment, we choose the laser frequency such that the dependence of the OH^- photodetachment cross section on the ions internal structure negligible, i.e. all internal states have the equal photodetachment cross sections. In this sense, we can assume that the dynamical change on the number of ions in the cloud $dN(t)/dt$ is proportional to total number of ions at a given time $N(t)$. This can be modeled by means of the following differential equation [53, 52]:

$$\frac{dN(t)}{dt} = -\sigma_{pd,\nu} \cdot \iiint F_\gamma(x, y, z) \cdot n(x, y, z) N(t) dx dy dz \quad (3.13)$$

with $N(t)$ \rightarrow number of trapped ions at the time t ,
 $\sigma_{pd,\nu}$ \rightarrow absolute photodetachment cross section
for OH^- at the laser frequency ν ,
 $F_\gamma(x, y, z)$ \rightarrow photon flux density distribution,
 $n(x, y, z)$ \rightarrow ions geometrical distribution in space.

For solving the differential equation 3.13 we first work out the geometrical overlap integral by making following simplification. For the ion cloud spatial

3 Sympathetic cooling of anions by ultra-cold atoms

distribution we assume that the ion cloud is very dilute and is at thermal equilibrium. Therefore, the ion cloud shape can be described by a single particle density distribution given only by the shape of the trapping potential. The integration in dz of this term yields unity times the projection of the 3D single-particle density distribution onto the (x,y) plane. This projection is called single-particle column density distribution $\rho(x, y)$.

For the photon flux density distribution we assume that: i) z is the laser's propagation direction and it is constant along this path. Therefore, the integration in dz yields the number of photons per second that go through the (x,y) plane. ii) the laser beam is much smaller in size than the ion cloud. In consequence, the geometrical dependency in x and y directions of the laser are negligible. A delta distribution at the point (x_γ, y_γ) models this geometrical distribution. With these assumptions, the photon flux can be written as:

$$F_\gamma(x, y, z) = \frac{P_\gamma}{h\nu} \delta(x - x_\gamma) \delta(y - y_\gamma). \quad (3.14)$$

with $P_\gamma \rightarrow$ laser beam power [W],
 $h\nu \rightarrow$ photon energy [J],
 $\delta(x; y) \rightarrow$ Dirac delta function [1/m],
 $x_\gamma, y_\gamma \rightarrow$ laser beam position relative to the ion cloud [m].

Setting equation 3.14 in 3.13, one can easily solve the overlap integral. Integrating the two remaining dimensions dx and dy yields the single particle column density $\rho(x_\gamma, y_\gamma)$ evaluated at the relative laser position (x_γ, y_γ) . Equation 3.13 become:

$$\frac{N(t)}{dt} = - \underbrace{\sigma_{pd,\nu} \cdot \frac{P_\gamma}{h\nu} \cdot \rho(x_\gamma, y_\gamma)}_{=\kappa_{pd,\nu}} N(t). \quad (3.15)$$

The solution to the differential equation 3.15 is an exponential function with the photodetachment decay rate $\kappa_{pd,\nu}(x_\gamma, y_\gamma)$:

$$N(t) = N(0) \cdot e^{-\kappa_{pd,\nu}(x_\gamma, y_\gamma) \cdot t} \quad (3.16)$$

with $N(0)$ being the initial number of trapped ions.

In the experiment, one can measure the number of ions remaining in the trap as a function of the photodetachment interaction time t at a given position (x_γ, y_γ) . Fitting equation to this data gives the photodetachment decay rate at this position. From this analysis, two main conclusions can be made:

- By measuring $\kappa_{pd,\nu}$ for different positions of the laser beam in both directions, one can directly measure the absolute photodetachment cross section at the chosen laser frequency ν . This is made by integrating the measured decay rates over the (x,y) plane:

$$\iint \kappa_{pd,\nu}(x_\gamma, y_\gamma) dx dy = \iint \sigma_{pd,\nu} \cdot \frac{P_\gamma}{h\nu} \cdot \rho(x_\gamma, y_\gamma) dx dy \quad (3.17)$$

3 Sympathetic cooling of anions by ultra-cold atoms

Since the integral of the single particle density over the x and y directions is one (right term of this equation), one obtains for the absolute cross section

$$\sigma_{pd,\nu} = \frac{h\nu}{P_\gamma} \cdot \iint \kappa_{pd,\nu}(x_\gamma, y_\gamma) dx dy \quad (3.18)$$

- The single ion column density is directly proportional to the measured decay rate at the position. Therefore, measuring the decay rate at different laser positions gives the information on the spatial distribution of the ion cloud inside the trap:

$$\rho(x, y) = \frac{h\nu}{P_\nu \cdot \sigma_{pd,\nu}} \cdot \kappa_{pd,\nu}(x, y). \quad (3.19)$$

The absolute photodetachment cross section can be either determined in the experiment as explained above, or it can be taken from the literature, for example ($\sigma_{abs,15108\text{ cm}^{-1}} = 8,5 \cdot 10^{-18} \text{ cm}^2$) [53].

Furthermore, as seen in section 3.2.1, for a given trapping potential landscape $V(x, y)$, the shape of the ion cloud $\rho(x, y)$ depends only on the temperature T of the ions as

$$\rho(x, y) \propto e^{-\frac{V(x,y)}{k_B T}}. \quad (3.20)$$

Consequently, with exact knowledge on the trapping potential $V(x, y)$, measuring the decay rates as a function of the laser position gives direct information about the temperature of the ions. Nevertheless, an exact calculation of this potential is very difficult. Even with sophisticated software as SIMION, as in our case, or other programs as used in [15], this estimation is usually the greatest source of error.

Yet, independently on potential calculations, one can still make relative measurements on possible ions temperature changes. Assuming that i) the trapping potential is separable, i.e. $V(x, y) = V(x) + V(y)$, and ii) the axial trapping potential is harmonic, i.e. $V(x) \propto x^2$, one expects the ion cloud to be normally distributed in axial direction. Fitting a normal distribution to the measured decay rates for different axial positions, one can extract its standard deviation σ_x , which correlates with the ion temperature as $\sigma_x \propto \sqrt{T}$.

Experimental procedure

The experimental cycle for measuring the spatial distribution of the ion cloud inside the radio frequency trap is shown in figure 3.8. The anions are created and loaded into the octupole rf-trap as described in section 2.1.3. At the beginning of the trapping process, the ions interact with a He buffer gas pulse of ≈ 200 ms at room temperature (295 K). Once trapped, the ion cloud is cleaned out for O^- impurities, assuring that only OH^- remains in the trap (section 2.1.4). During

3 Sympathetic cooling of anions by ultra-cold atoms

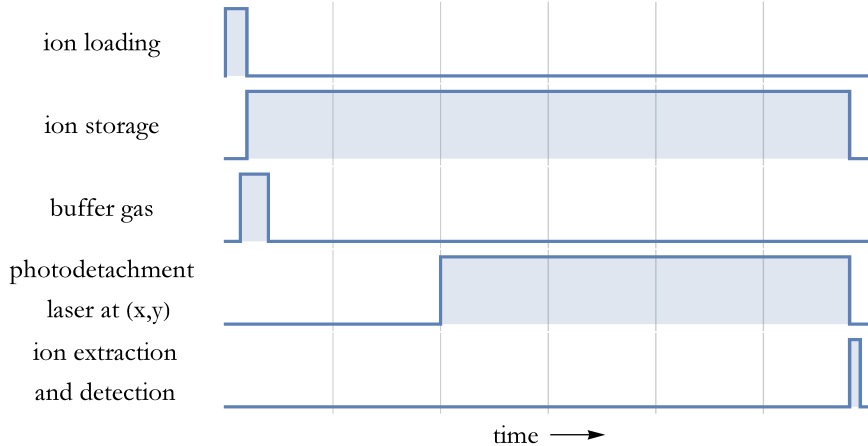


Figure 3.8: Experimental cycle timings for photodetachment tomography. Before loading, the laser is positioned at (x,y) by means of a 2D translation stage. During loading, the ions interact with a pulse of helium buffer gas at 295 K. The ions are stored in the trap for a fixed time set for all experimental runs. After pumping out the buffer gas, the photodetachment laser beam with frequency ν is turned on for a given time period related to the end of the total ion storage time. Lastly, the remaining ions are extracted and counted. Times are not to scale.

this time, we ramp the electrodes down in order to get rid of radial potential pockets caused by the de-confinement effect of the dc-offset potential set at the rf-wires (see section 3.2.1). Afterwards the photodetachment laser beam is shined into the ion clod (perpendicular to the trap, as depicted in figure 3.9) at a given (x,y) position, which is set prior to the beginning of the experimental cycle. The ions cloud then interact with the laser beam for a certain interaction time. The remaining ions are subsequently extracted and counted with a channeltron detector (section 2.1.4). This data and the corresponding set values are stored for further analysis. This experimental run is repeated several times for different interaction times at a given laser position. At each experimental run, the interaction time is shuffled in order to reduce systematic uncertainties. The laser power is monitored via a calibrated photo-diode for each experimental run.

A set of example results of this procedure is shown in figure 3.10. Shown is the mean number of ions detected as a function of the photodetachment interaction time for different axial positions. The error bars are the standard deviation of the ion number weighted with the square root of the number of measured values. The solid lines depict an exponential fit to the data using equation 3.2.2. The fit algorithm then provides the best parameter value for the photodetachment decay rate κ_{PD} . As discussed above, the last value is directly proportional to the column density of the ion at the position of the laser 3.19. As a consequence, by

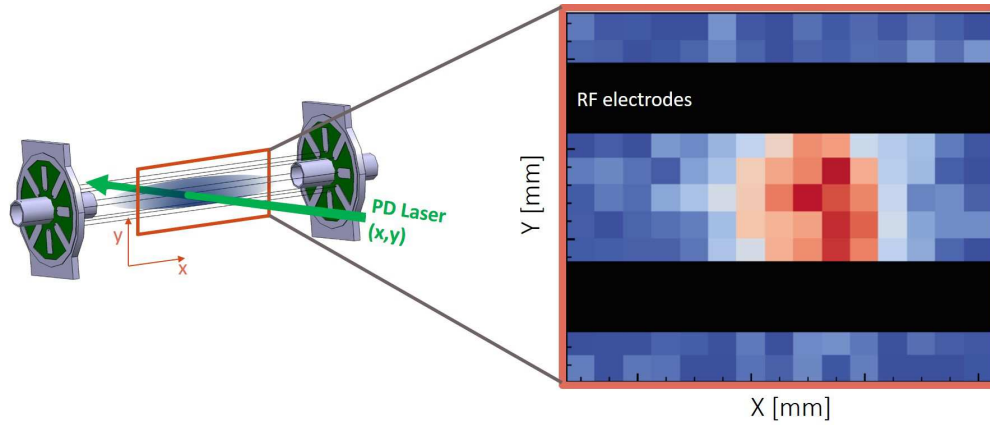


Figure 3.9: Determination of the ions spatial distribution via photodetachment tomography.

Left graph: Simplified sketch of the experimental setup. The trapped ions are marked inside the rf trap as a blue cloud. The photodetachment laser and its propagation direction is marked as a green arrow. The laser can be placed with respect to the ion cloud at an arbitrary position by means of a translation stage.

Right graph: Example of a resultant photodetachment image. Red corresponds to the maximum value of the ions column density measured and blue depicts the case for a value of zero on the decay rate.

scanning the laser position in a 2D raster along the trap, one obtains the spatial distribution information of the ion inside the trap.

This information can be plotted as an image of the ion cloud. This is done in figure 3.10. Furthermore, this information can be used to measure the absolute cross section of $\text{OH}^- + \gamma$, as explained above (equation 3.18).

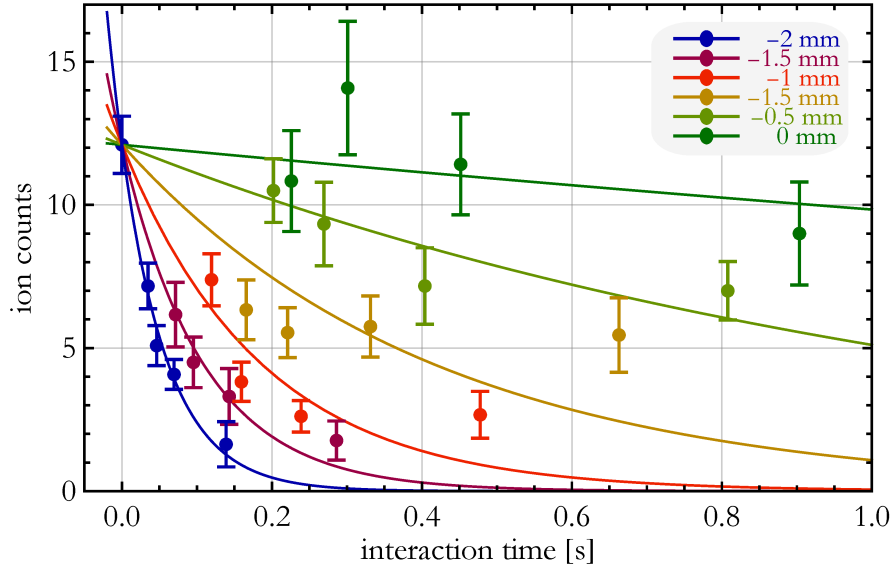


Figure 3.10: Photodetachment ions decay for different axial positions.

The mean ion count is plotted as a function of the interaction time between the ions and the photodetachment laser for different positions in axial direction at a fixed radial position. The solid lines represent a fit to the data using equation 3.2.2.

Determination of absolute σ_{PD} in our HAITrap

In figure 3.11 a typical image of the ions inside the trap is shown. Specifically, the photodetachment decay rate (color coded) is plotted as a function of the radial and axial position of the photodetachment laser. As stated above, this information can be used for measuring the absolute photodetachment cross section of the ions interacting with photons at a given wavelength.

For this experiment, a diode laser was used, a full characterization of which was done in the frame of a bachelor thesis in our group [66]. The wavelength of the laser used is 661.2 nm, which corresponds to a wavenumber of $15\,124\text{ cm}^{-1}$, and its power was 40 mW. As will be discussed in chapter 4, at this wavelength the photodetachment cross section does not depend on the internal structure of the ions (see figure 4.3). Given this values, using equation 3.18 the resultant cross section measured results in $\sigma_{PD,662nm} = 7.3 \cdot 10^{-18}\text{ cm}^{-2}$.

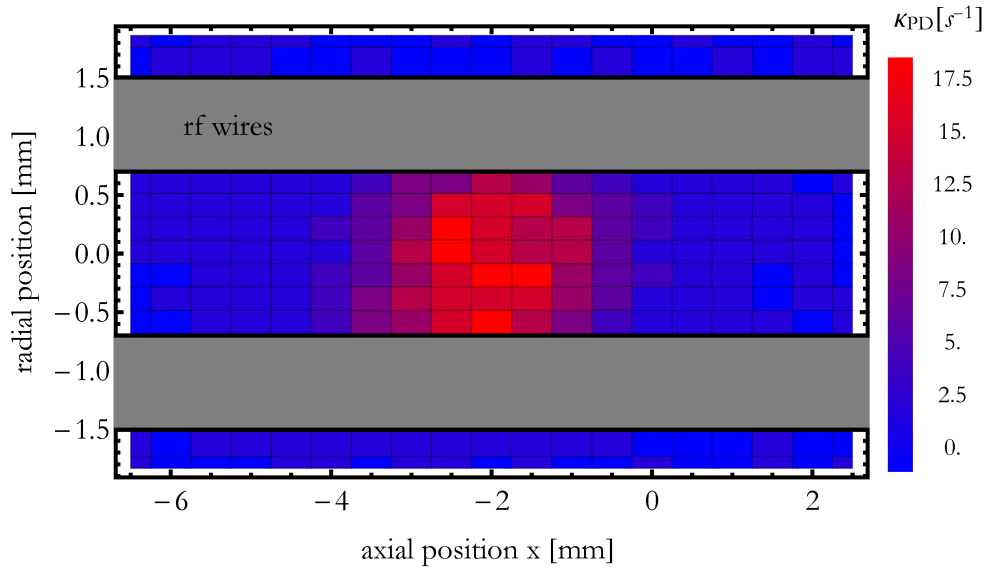


Figure 3.11: Image of the ion cloud inside the radio frequency trap. Plotted is the photodetachment rate as a function of the axial and radial position of the laser beam. The gray zones depict the radio frequency wires, which make this region of the trap optical inaccessible.

3.2.3 Experimental evidence of sympathetic cooling

In this section, we provide experimental evidence on sympathetic cooling of ions by collisions with ultracold atoms in our HAITrap. The thermometry method applied for this aim is photodetachment tomography, details of which are explained in section 3.2.2. In contrast to the experimental procedure shown in that section for measuring σ_{PD} , here we let the ions interact with an ultracold cloud of rubidium atoms placed in the center of the trap prior to the photodetachment procedure. An sketch of one experimental cycle is shown in figure 3.12. After a fixed atom-ion cloud interaction time (4 s) for all experimental runs, a photodetachment laser beam is shined into the ion cloud as depicted in figure 3.9. The interaction time between ions and photodetachment laser is pseudo shuffled after each experimental run. For this experiment, a total number of 900 experimental cycles were performed for each buffer gas.

For each laser position, an exponential decay (equation 3.2.2) is fitted to the resultant ion counts as a function of the photodetachment interaction time, similarly as shown in figure 3.10. As stated before (equation 3.19), this decay rate is directly proportional to the ions column density. The fitted values of the photodetachment decay rate are plotted as a function of the laser position. The final results of this measurement are plotted in figure 3.13. Thereby, the error bars depict the parameter errors provided by the fitting algorithm. Because of the ion losses caused by associative detachment (section 3.1.1), after 4 s atom-ion

3 Sympathetic cooling of anions by ultra-cold atoms

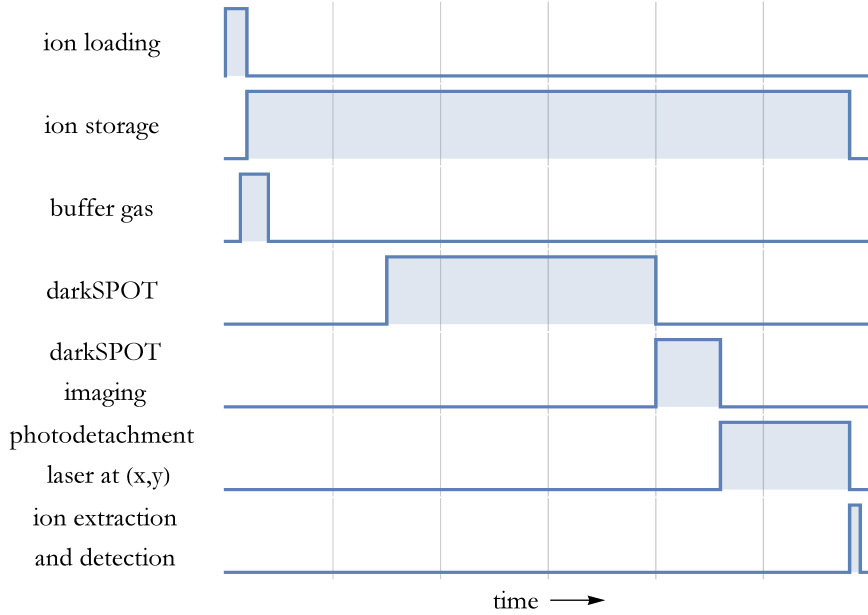


Figure 3.12: Experimental cycle timings for photodetachment thermometry. Before loading, the laser is positioned at the axial position x along the symmetry axis ($y = 0$) by means of a 2D translation stage. During loading, the ions interact with a pulse of helium buffer gas at 295 K. The ions are stored in the trap for a fixed time set for all experimental runs. After pumping out the buffer gas, rubidium atoms are loaded in the darkSPOT if needed. After a certain interaction time, a detuned-absorption image of the atom cloud is made. Thereafter the photodetachment laser beam is turned on for a given time period related to the end of the total ion storage time. Lastly, the remaining ions are extracted and counted. Times are not to scale.

cloud interaction time only a few ions remain in the trap, in this case we count a mean number of 6 ions right after the atom-ion clouds interaction. This and the big fluctuations on the number of ions loaded in the trap are the reason for the relative large errors on the photodetachment decay rate in the case for $\text{OH}^- + \text{Rb}$.

The solid lines in the figure show a Gaussian fit to the data, which provided following values: $\sigma_{x,\text{OH}^-+\text{He}} = 1.12 \pm 0.08$ mm and $\sigma_{x,\text{OH}^-+\text{Rb}} = 0.56 \pm 0.08$ mm. In spite of the big systematic uncertainties of this measurement, it provides a clear effect of sympathetic cooling. In order to make a rough estimation of the final temperature of the ions, we can make following analysis. Assuming a harmonic trapping potential, the spatial standard deviation correlates with the ions temperature as $\sigma_x \propto \sqrt{T}$ (equation 3.20). Therefore, we can estimate the final decrease on the temperature of the ions after their interaction with

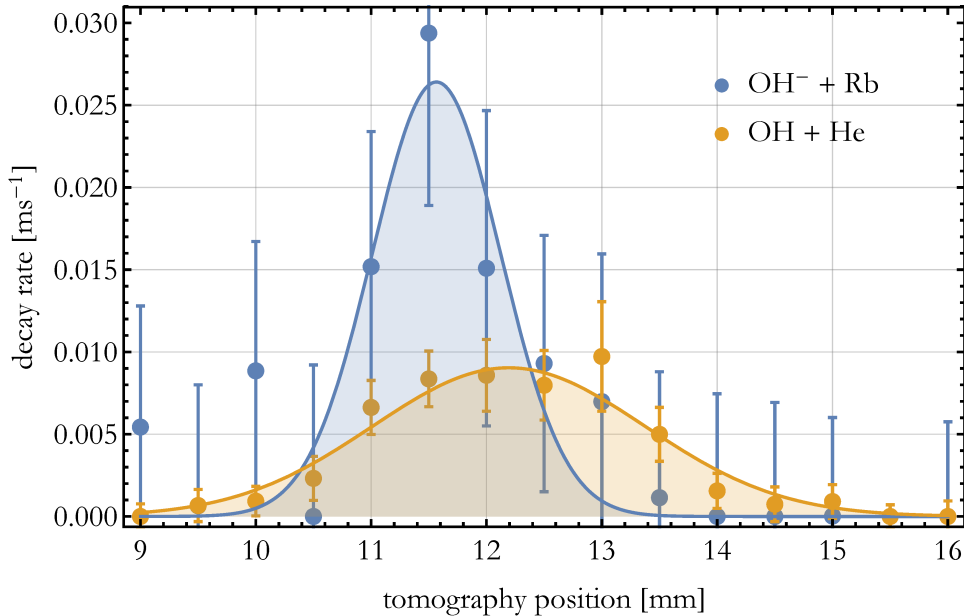


Figure 3.13: Experimental evidence of sympathetic cooling via 1D photodetachment tomography. The measured ions decay rate (as in figure 3.10), which is directly proportional to the ions column density, is plotted as a function of the photodetachment laser position. The error bars depict the parameter errors provided by the fitting algorithm. The tomography measurement was done along the symmetry axis of the trap ($y = 0$). The ions interacted with two different buffer gases: helium at room temperature (295 K) and localized rubidium at $\approx 300 \mu\text{K}$. The solid lines show a Gaussian fit to the data, which provided following values: $\sigma_{\text{He}} = 1.12 \pm 0.08 \text{ mm}$ and $\sigma_{\text{Rb}} = 0.56 \pm 0.08 \text{ mm}$. The narrowing of the spatial distribution can be attributed to sympathetic cooling of the anions by the ultra cold atoms.

rubidium as $T_{\text{OH}^- + \text{He}}/T_{\text{OH}^- + \text{Rb}} = (\sigma_{x,\text{He}}/\sigma_{x,\text{Rb}})^2 = 0.24 \pm 0.08$. This means that the ions have only 24% of their initial temperature. Assuming that the ions thermalized with the helium buffer gas at room temperature as expected from our simulations (see figure 3.6), we can attribute the standard deviation $\sigma_{x,\text{He}}$ to be a measurement of the spatial distribution of the ions being at 295 K. This estimation provides a final ions temperature of $72 \pm 26 \text{ K}$.

3.3 Thermometry via Time of Flight

In this section, we apply the method called *time of flight thermometry* to demonstrate sympathetic cooling of ions via elastic collisions with a localized rubidium buffer gas. This technique is based on mapping the velocity of a trapped ion at the moment of extraction to the ion's time of flight (ToF) from the trap to the detector. It has been applied in a similar way in other groups [29, 111].

In order to understand the ion dynamics of the extraction procedure, we first make numerical simulations of the trajectory of the ions from the trap towards the detector. Details of these simulations are presented in section 3.3.1. Afterwards, in section 3.3.2, we present the experimental procedure for sympathetic cooling, the measured time of flight distributions and give an intuitive interpretation of these results based on thermal distributions. In section 3.3.3 we discuss the interpretation of the ToF distributions based on the predicted non-thermal distributions. Thereby we show that the measured ToF distributions are statistically better explained as a consequence of initial energy distribution given by a Tsallis function as compared to a Boltzmann function.

3.3.1 Trajectory simulations

This section gives an overview on the ions trajectory simulations performed for understanding the dynamics of the ions during their extraction procedure. Thereby we explore the possibility to map the energy distribution of a trapped sample of ions to the ion's time of flight (ToF) from the trap to the detector. Further details on these simulations can be found in two bachelor thesis undertaken in our group during the course of this work [63, 67].

HAITrap electrodes extraction configuration in SIMION

As explained in section 2.1.3, the electrode configuration of our HAITrap, as shown in figure 3.14, was implemented in SIMION based on a 3D geometrical CATIA model of our trap (figure 2.8). Details for this implementation can be found in [63].

In order to simulate the ion extraction procedure as we do in the experiment, we set the different electrodes at their corresponding voltages (see section 2.1.3). For the rf-trap, we use its full electrode configuration as shown in figure 2.8, as these are the most critical parameters for simulating the extraction of the ions out of the trap. A group of these electrodes have the same voltage during the trapping as during the extraction, i.e. no potential switch is implemented. These are:

- Shielding electrodes at the top/bottom: $V_{Sh,t/b} = 80 \text{ V}$
- Left side end cap electrode: $V_{EC,l} = 40 \text{ V}$
- dc-offset at the rf-wires: $V_{dc} = 30 \text{ V}$

The extraction potential is then generated by 3 electrodes:

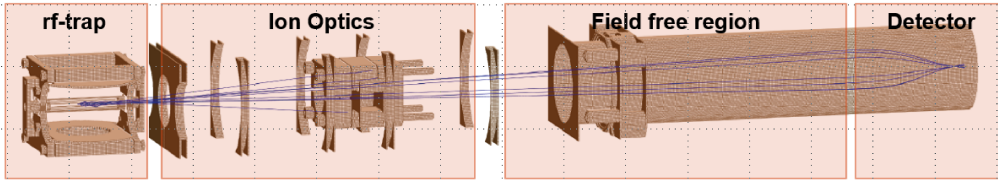


Figure 3.14: Electrode configuration in SIMION. On the basis of this 3D model of the electrodes used in our HAITrap, SIMION computes an electrostatic potential by means of the Laplace equation 2.7. This allows the numerical simulation of the ion trajectories from the rf-trap to the detector (marked as blue lines) using equation 2.8. Due to an extraction potential, the ions escape the rf-trap through the hollow end cap electrode. The ion optics compensate geometrical imperfections and lead most of the ions to the detector. Afterwards, they fly through a field free region and are attracted by the potential from the detector.

- Right side end cap and shielding electrodes are set to ground: $V_{EC,r} = V_{Sh,r} = 0$ V.
- Left shielding electrode: $V_{Sh,t/b} = 150$ V.

The ion optics after the trap, as implemented in our experiment, is a combination of an ion lens and benders in both horizontal and vertical directions. In our simulations, we set the benders at 0 volts and the lens at -10 V. After the ion optics, the ions enter a field free region and are then attracted by the potential of the ion detector (at 1500 V). In the simulation, the CF40 detector mounting tube is implemented as part of the geometrical configuration (field free region in the figure) because it affects critically the potential shape near the detector. Furthermore, in figure 3.14 a set of trajectories simulated in SIMION is shown (blue lines), giving an intuitive visualization of the possible motions of an ion after the extraction.

Visualization of the extraction potential

For the values described above, the resultant total extraction potential along the middle axis is shown in figure 3.15. This 1D probing of the extraction potential offers an intuitive picture of the landscape the ions have to fly through. The axial position in the figure is scaled relative to the geometrical center of the trap in axial direction. Only the region of the ion trap is shown.

One observes from the figure that the ions have to travel first through a potential with relatively low gradient and afterwards they are accelerated by a steep potential. This is a similar potential configuration we have seen in section 2.1.3 for the Wiley McLaren time of flight mass spectrometer [78]. Indeed, one similarity of this potential configuration with the spectrometer is that we can find a potential region where the ions time of flight does not depend on the ion initial position.

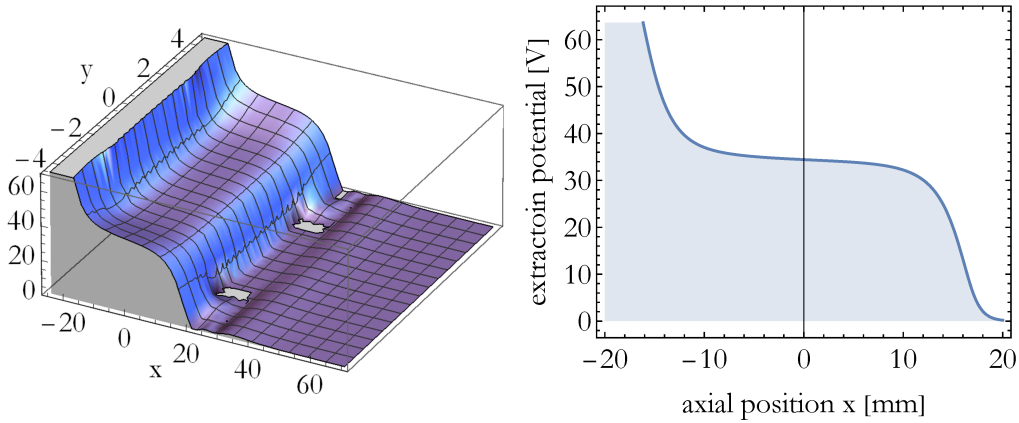


Figure 3.15: 2D and 1D cut of the extraction potential landscape along the trap’s symmetry axis. The extraction potential is plotted as a function of the axial x (and radial y) position. $x = 0$ is the geometrical center of the trap. The potential curve is calculated in SIMION using the voltages from the experiment for each electrode. Also used are the potentials from the ion optics and the ion detector. These are described in detail in the text.

ToF spread: initial position

For finding a trap’s region where the ToF does not depend on the ions initial position, we numerically calculate different ion trajectories. As we have the information of the extraction potential, the derivative in three dimensions provides the electric field. By solving then the corresponding differential equation, we obtain the full trajectory information. This is done with different initial conditions: the ions position and velocity in the trap at the moment of extraction. The final output from these simulations is the complete trajectory of the ion.

As a first estimation and for qualitative understanding of the extraction dynamics, we analyze the time of flight spread caused by the initial position of the ions in 1D along the trap’s symmetry axis. For this purpose, we let the initial velocity of the ions be 0. The ions axial position is probed in steps of 0.5 mm, with a total length of 20 mm centered in the geometrical center of the trap. From the numerical results we extract the time of flight at the detector and store it in an array with the corresponding initial position in the trap.

This array is shown in the upper graph of figure 3.16 as blue points. The solid blue line corresponds to a interpolation function to the simulated data. Furthermore in this graph, Gaussian ion density distributions are plotted in order to signalize the initial conditions for further simulations. The Gaussians are marked in different colors for different mean positions μ_0 , namely at the maximum of the time of flight curve with green, at the center of the trap with orange and 3 mm right from the center in blue. For each μ_0 , 4 different σ are chosen: $\{0.1;0.4;0.7;1\}$ mm. This σ correspond to the Gaussian probability of finding an ion in a harmonic potential at different temperatures.

3 Sympathetic cooling of anions by ultra-cold atoms

The bottom graph of figure 3.16 show the results of simulating 10^6 ions for each Gaussian distribution shown in the upper graph. The resultant time of flight distributions are binned and normalized to the corresponding maximum value. Otherwise the green distributions would make the other curves not visible. These results are shown as points with the same color coding as the upper distributions. The blue distributions are fitted with a Gaussian distribution, the standard deviation of which correlates linearly with the original σ . The orange distributions show asymmetric behavior due to the non linear ToF correlation. The green distributions meet the Wiley-Mc-Claren criteria, i.e. the ions ToF in this region is nearly not depending on the initial ions position. In this case, for all initial axial spreads, about 95 % of the ions arrive within 100 ns.

3 Sympathetic cooling of anions by ultra-cold atoms

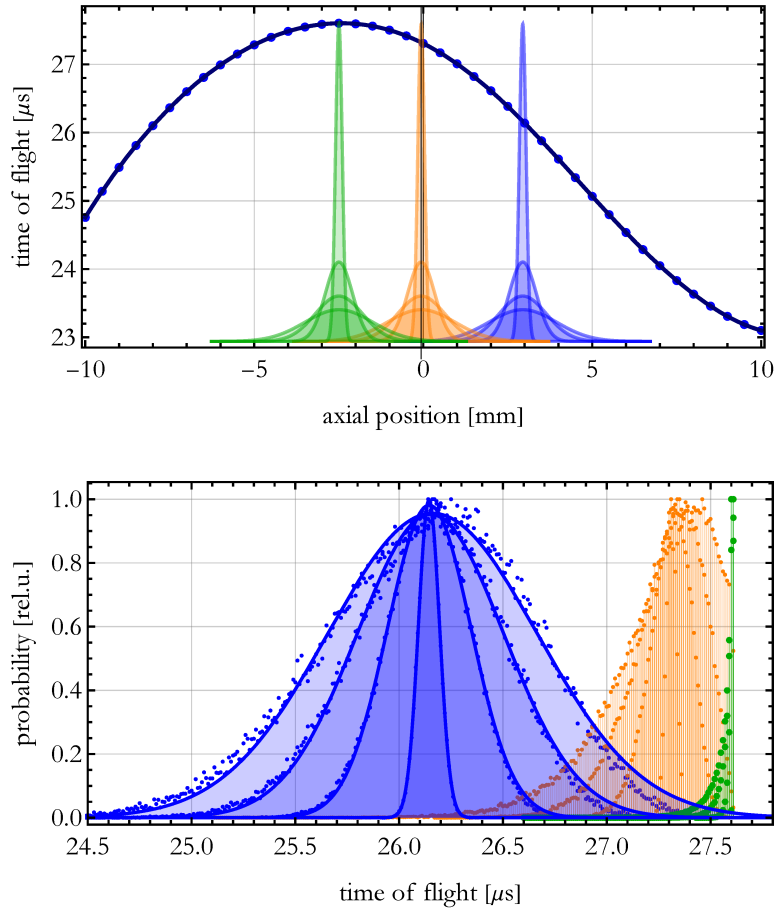


Figure 3.16: Time of flight space spread. The ions time of flight was simulated as a function of their initial position of the trap with zero initial velocity.

Top graph: The full trajectories of 20 ions were simulated, the arrival times of which are marked as blue points. The solid blue line corresponds to a interpolation function to the simulated data. Furthermore, Gaussian ion density distributions are marked with different colors indicating the initial conditions for the further simulations showed in the bottom graph.

Bottom graph: 10^6 ions are simulated for each Gaussian distribution showed in the upper graph. The resultant ions ToF are binned and normalized to the corresponding maximum value. These results are shown as points with the same color coding as the upper distributions. The blue distributions are fitted with a Gaussian distribution, the standard deviation of which correlates linearly with the original σ . The green distributions meet the Wiley-Mc-Claren criteria, i.e. the ions ToF in this region is nearly not depending on the initial ions position.

ToF spread: initial velocity

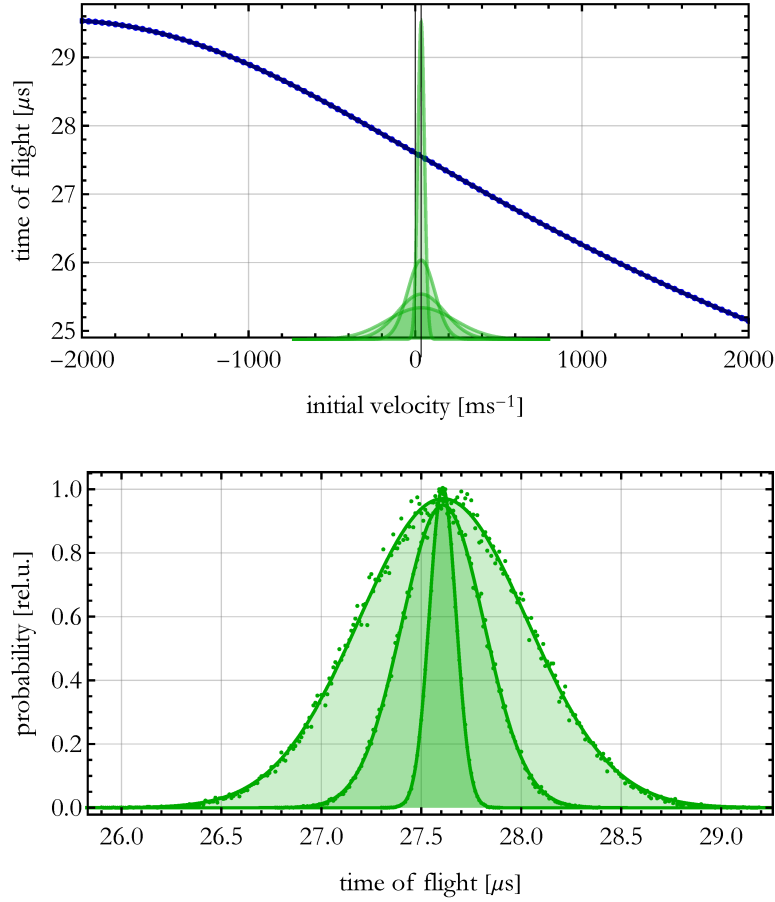


Figure 3.17: Time of flight velocity spread. The ions ToF was numerically calculated as a function of their initial velocity. All ions start at the same position, namely at the maximum of the ToF space spread curve (figure 3.16).

Top graph: The simulated arriving ToF of the ions are shown as green dots and are plotted as a function of their initial velocity. The green distributions correspond to a Boltzmann distribution, the wider ones represent 300 K for OH⁻.

Bottom graph: The resultant time of flight distributions are shown for the different Gaussian distributions shown in the upper graph. We observe again a linear correlation of the standard deviation from the fitted Gaussians and the initial σ_v .

The same analysis can be made for the spread in the time of flight distribution caused by the initial ions velocity distribution. In figure 3.17 the results of our numerical simulations are shown. Thereby, the ions axial velocity is probed in steps of $10 \text{ m} \cdot \text{s}^{-1}$ in a range of $\pm 2000 \text{ m} \cdot \text{s}^{-1}$ with initial position corresponding

to the axial position where the ions time of flight curve from figure 3.16 reaches its maximum. This line shows a near linear correlation between the initial velocity and the ions time of flight.

In order to compare the spatial ToF spread with the one caused by the velocity, we simulate 10^6 ions in a thermal distribution. These distributions are schematically shown in the upper graph of the figure. The wider one corresponds to a thermal distribution of 300 K, the corresponding standard deviation for the case of oh- is 381 ms^{-1} . The resultant ToF distributions are shown in the bottom graph. In this case we again find a nearly linear correlation between the initial velocity spread σ_v and width of the fitted normal distribution to the simulated data.

ToF spread: phase space

Now we analyze the ToF spread caused by the combination of the both effects shown above, i.e. the 2D phase space. For this aim we calculate a 3D array consisting of the initial axial position and velocity with its respective time of flight. In the left graph of figure 3.18 an interpolation function of this 3D array is shown. Thereby, the resultant ions ToF is plotted as a function of the ion's initial axial position and initial velocity. A key observation is that the ions velocity is *imaged* to the ToF in a systematically increasing order for all the axial positions, which is important for the final temperature mapping.

In the same figure, the right graph shows the results from the simulations by taking into account both the spatial and the velocity spread of the ions in the trap. Simulating the final ToF distributions is performed in a way similar to the cases shown above. For each temperature on this case, we generate 10^4 ions, each of which has a pseudo-randomly chosen initial position and velocity. The probability functions for both initial conditions are normal distributions. For the case of the velocity, this is given by a thermal Boltzmann distribution, implying that the mean velocity in axial direction is zero and the velocity spread is computed by $\sigma_v = \sqrt{k_B T / m_i}$. This is 381 ms^{-1} for the room temperature case, whereas it is about 100 ms^{-1} for 20 K. For the spatial dimension, the mean of the Gaussian is directly correlated with its temperature. This is, by assuming a harmonic confining potential, the size of the ion cloud (characterized by its standard deviation) is given by $\sigma_x \propto \sqrt{T}$. Here, the proportionality factor is given by the curvature of the harmonic potential. For these simulations we choose the harmonic potential such that $\sigma_{x;(T=300 \text{ K})} = 1 \text{ mm}$. We observe again, the colder the ions are in the beginning, the narrower the resultant ToF distribution gets.

For a more accurate estimate about which parameter brings the mean initial position of the ion cloud on this behavior, we make similar simulations as in figure 3.18, but now scanning the temperature as well as μ_x over the ion cloud's axial position relative to the trap. From these simulations, we fit the resultant ToF with a Gaussian and plot their standard deviations as a function of the axial position. The results of this analysis are shown in figure 3.19.

In order to compare the relative effect on the ToF width, we normalize the

3 Sympathetic cooling of anions by ultra-cold atoms

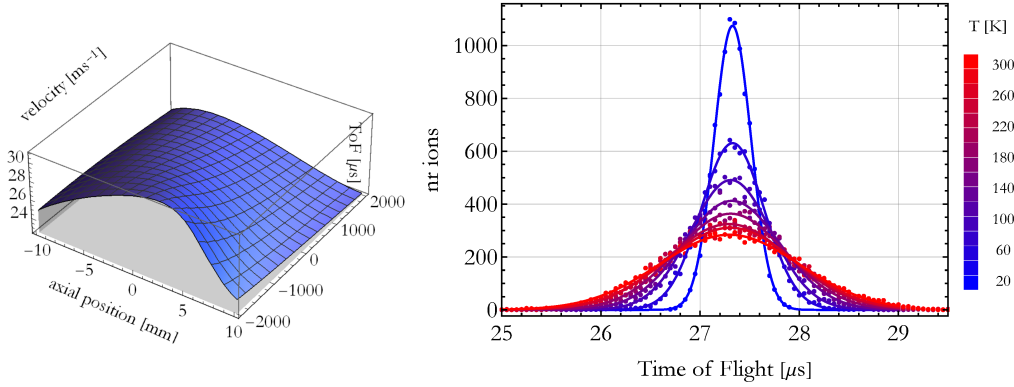


Figure 3.18: ToF spread caused by the ions phase space in the trap. The calculation was done for the extraction potential showed in figure 3.15.

Left graph: The ions ToF is plotted as a function of their initial position and initial velocity.

Right graph: Resultant ToF distributions for different initial temperatures. Thereby the ions cloud mean position is at the center of the trap ($\mu_x = 0$).

resultant widths for each mean position with the resultant width for 300 K at that position. This means, for each μ_x from figure 3.19, the ToF widths are normalized as $\sigma_{ToF, \mu_x} / \sigma_{ToF, \mu_x, (300K)}$. In figure 3.19, these relative widths σ_{rel} are plotted as a function of the ions initial temperature. From this data, we observe a clear correlation between the relative time of flight spread and the initial ions temperature, regardless of the initial position of the ions. The correlation is of the form $\sigma_{ToF} \propto \sqrt{T}$, which allows us to extract the ions temperature as a first good approximation.

3 Sympathetic cooling of anions by ultra-cold atoms

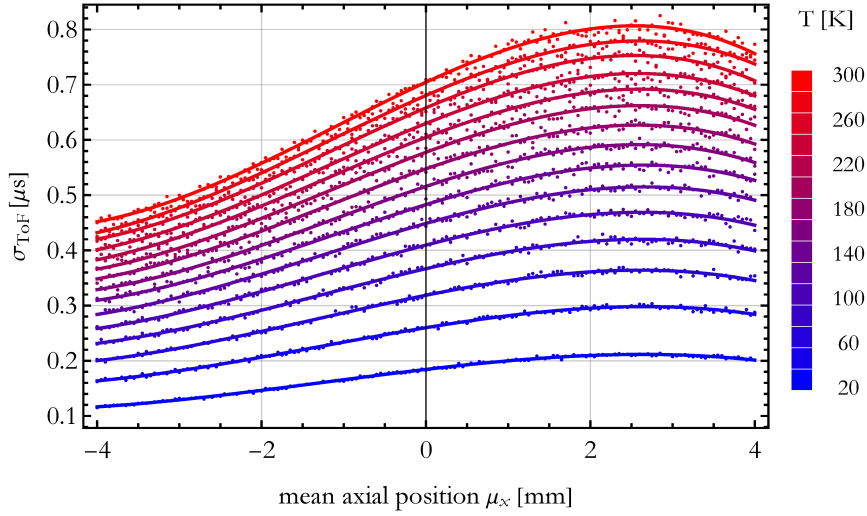


Figure 3.19: ToF spread as a function of the mean ion cloud's axial position for different temperatures. Each point represents the standard deviations of the fit to the resultant ToF distributions of 10^5 ions. The solid lines are a guide.

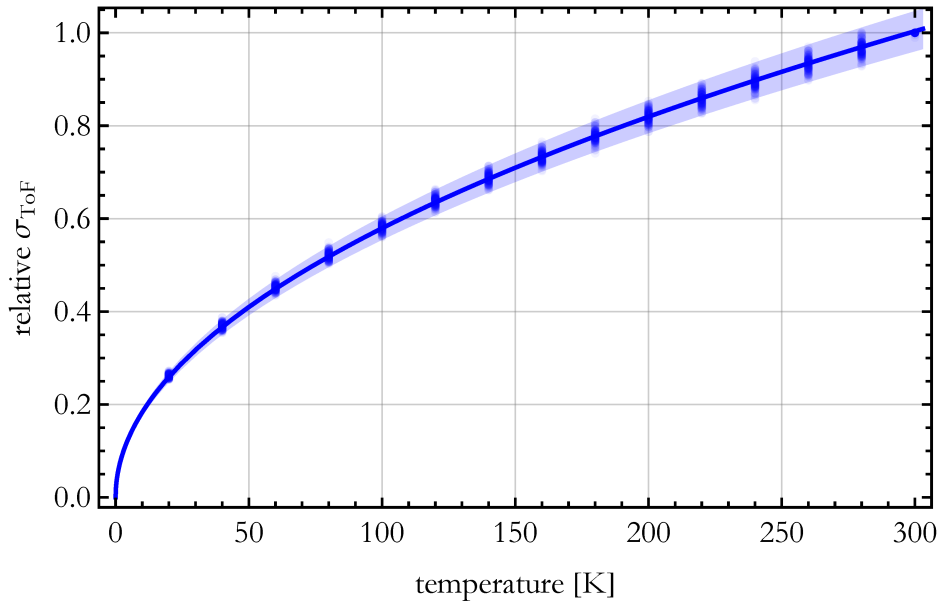


Figure 3.20: ToF temperature mapping. For each mean starting position μ_x from figure 3.19, the resultant ToF widths are normalized as $\sigma_{ToF,\mu_x} / \sigma_{ToF,\mu_x,(300K)}$. These are plotted as a function of the ions initial temperature (blue points). The solid line is a fit to the simulated data with $\sigma_{ToF} \propto \sqrt{T}$.

3.3.2 Experimental demonstration of sympathetic cooling

In the last section we have shown the expected correlations between the trapped ions temperature and their time of flight (ToF) distribution after extraction. These numerical simulations show a characteristic dependence of the ToF distribution's width on the ion's temperature in the trap (see figure 3.20). In this section, we apply this technique experimentally and show sympathetic cooling of anions via elastic collisions with ultra cold rubidium atoms.

Experimental cycle

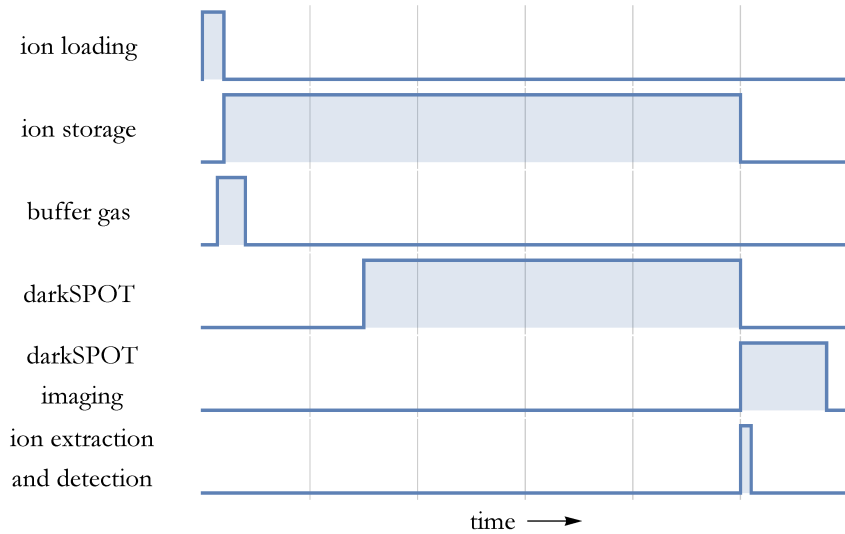


Figure 3.21: Experimental cycle timings for sympathetic cooling. During loading, the ions interact with a pulse of helium buffer gas at 295 K. The ions are stored in the trap for a fixed time set for all experimental runs. After pumping out the buffer gas and ramping down the static potentials of the ion trap, rubidium atoms are loaded into the darkSPOT. After a certain ion-atom interaction time, the ions are extracted and counted. A detuned-absorption image of the atom cloud is captured to monitor the atom cloud characteristics. Times are not to scale.

A sketch of the experimental cycle timings is shown in figure 3.21. First, the anions are created and loaded into the octupole rf-trap as described in section 2.1.3. At the beginning of the trapping process, the ions interact with a He buffer gas pulse (≈ 250 ms) at room temperature (295 K). In order to detach O^- impurities from the ion trap, the atoms cooling laser is on during this time. As seen in section 3.1.3 we expect the ions to be fully thermalized with this buffer gas. Consequently the ions should have a thermal energy distribution of 295 K after the interaction with this initial buffer gas pulse.

3 Sympathetic cooling of anions by ultra-cold atoms

After loading, the ions are stored for a few seconds in the radio frequency trap for multiple reasons. During this time:

- the remaining He buffer gas is pumped out. This is needed for achieving a sufficiently low pressure in the main chamber ($\approx 10^{-8}$ mbar) in order to be able to load the Rb atoms into the darkSPOT.
- the trapped ion cloud is cleaned out for O^- impurities, assuring that only OH^- remains in the trap. This is done by photo-detaching O^- using the magneto-optical trap cooling laser (section 2.1.4).
- the static compensation potentials of our ion trap are ramped down. This is done for a convenient technical reason. The ion detection electronics, specifically the current amplifier, picks up a strong signal from the radio frequency generator. Therefore, after ion extraction we turn off the rf-generator. Nevertheless, it takes about $15\mu s$ for the generator to be completely off. As a consequence, ions arriving before this time at the detector are harder to detect, which leads to systematic errors in the measurement. A low dc offset potential on the rf wires leads to a longer time of flight to the detector. This enables us to separate the detected ion signal from the picked-up rf signal at the amplifier.
- the compensation electrodes are set such that the ion cloud is shifted for about two millimeters to the left from the axial center of the trap. This is done for the later extraction procedure. As seen from sections 3.3.1 and 2.1.4, in this region of the trap, the extraction potential accelerates the ions such that the arrival time of the ions at the detector does not depend on the ion's position at the moment of extraction.

After this ion cloud preparation, the rubidium atoms are loaded into the darkSPOT by switching on the re-pumper laser (section 2.2.3). In this way the atom and anion clouds are overlapped for a given interaction time. Note that prior to the experiment the atom cloud is prepared in two ways: i) the compensation coils of the magneto optical trap are set such that the overlap of both clouds is optimized ii) the dark state fraction of the atom cloud is set to be as high as possible (in our case $\approx 95\%$), in order to control chemical reactions (see section 3.1.1).

Thereafter, the remaining ions are extracted and detected. The time of flight data is stored for each experimental run (see figure 2.11). In order to monitor the optical density of the atom cloud after each experimental run, a non-resonant absorption image of the atom cloud is produced (section 2.2.3). The atom cloud imaging procedure is performed immediately after the extraction of the ions.

As seen in section 2.1.4, we have to limit the number of detected ions (under ≈ 20 ions per experimental cycle) in order to avoid saturation effects of the channeltron detector. At the same time, as shown in section 3.1.1, the system $OH^- + Rb$ has unavoidable reaction channels leading to ion losses during the cooling process. Therefore, prior to loading, we set the number of ions loaded

into the trap such that at the end of the interaction process, the number of detected ions remains under ≈ 20 ions per experimental cycle.

Final ToF distributions

The experimental run explained above is repeated several times for different interaction times and optical densities. These parameters are pseudo-randomized for each experimental run in order to reduce systematic uncertainties.

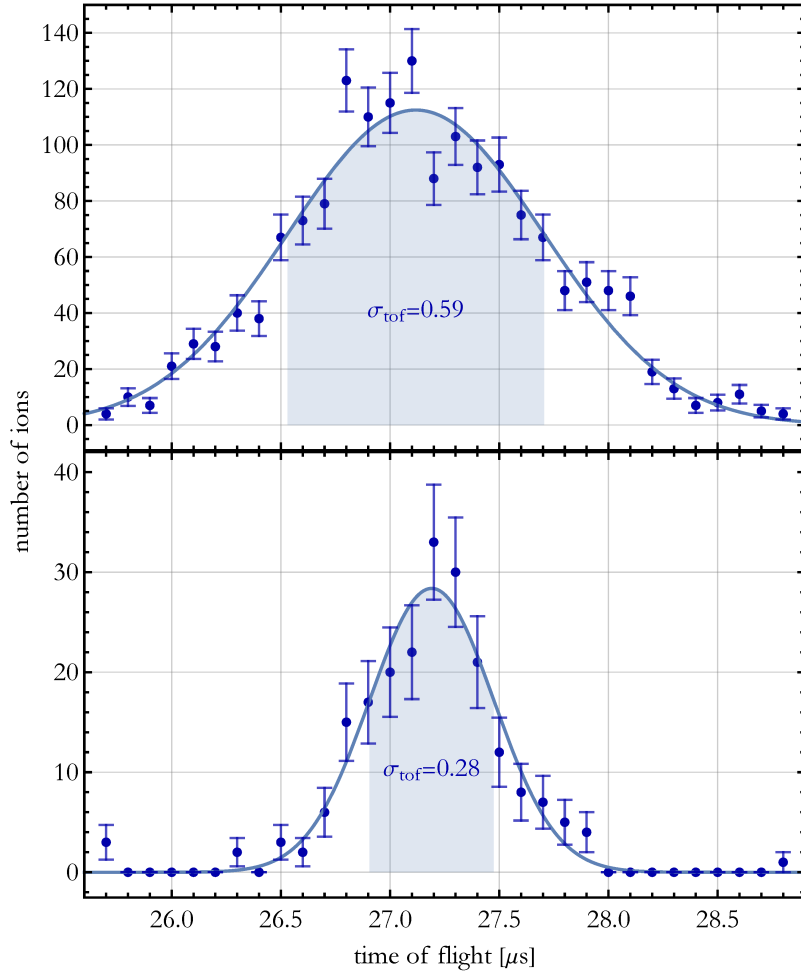


Figure 3.22: Typical ions time of flight distributions after two different interaction times with the atom cloud. The graph on top (at bottom) represents 1 s (4 s) interaction time with an atom cloud's optical density around 1 (1.6). The solid curves are a Gaussian fit to the data. The narrowing of the ToF distributions (characterized by σ_{tof}) is a direct proof of sympathetic cooling.

In figure 3.22 two examples of the measured ToF distributions are shown. In order to obtain the final ion ToF distributions for a specific interaction time

and optical density, the ToF data of each detected ion is grouped together and binned. Here we choose a bin width of 100 ns. The binned data is shown in the graph as points and represent the measured ToF distributions. The solid line in the graph represents the fit to the data using a Gaussian distribution. This distribution function is chosen as it allows a qualitatively intuitive interpretation of the cooling dynamics.

In figure 3.23 the results of a more systematic measurement for sympathetic cooling is presented. Thereby, the width of the measured ToF distributions (characterized by σ_{ToF}) is plotted as a function of the interaction time with the atom cloud. This is done for different atom optical densities and is shown in different colors.

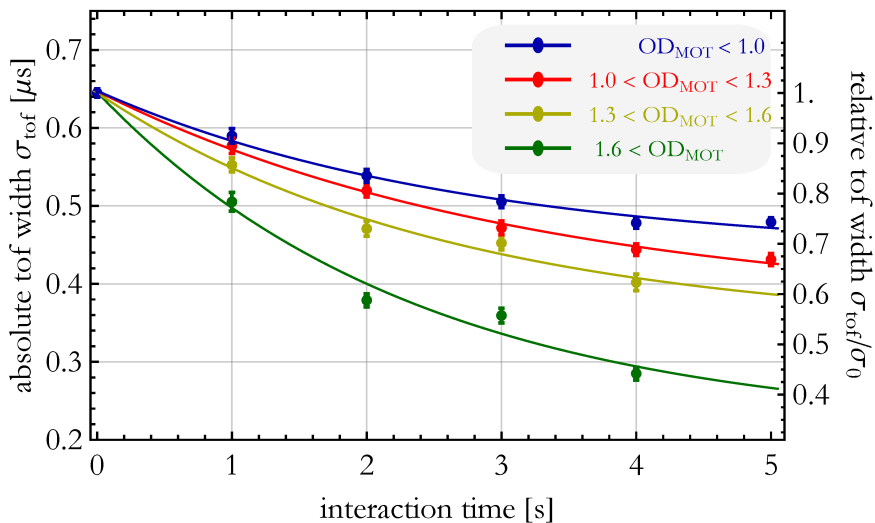


Figure 3.23: Demonstration of sympathetic cooling via time of flight.

The width of the measured ToF distributions (characterized by σ_{ToF}) is plotted as a function of the interaction time with the atom cloud. Different colors are chosen for different atom optical densities (see legend). The longer the interaction time and optical density, i.e. the more collisions, the narrower is the ToF distribution. This is a direct consequence of sympathetic cooling of the ions, as numerically validated in figure 3.20. The solid lines are a rescaled fit using equation 3.24.

One clearly sees from the figure that longer the interaction time and higher the optical density of the atom clouds are, as in other words, more the number of atom-ion collisions, the narrower the final measured ToF distribution gets. This is a direct consequence of sympathetic cooling of the ions, as can be validated in two different ways.

- **Experimental validation.** The characterization of our trap showed that the ions extraction procedure works similarly to a Wiley Mc-Laren ToF

3 Sympathetic cooling of anions by ultra-cold atoms

spectrometer [78]. This means that for specific conditions on the extraction potential, the arrival time of the ions does not depend on the ion's position at the moment of extraction (section 2.1.4). In this experiment the extraction potential is chosen such that it meets this conditions.

Consequently, the spread of the measured ToF distribution is only given by the energy distribution of the ions. This means, the observed narrowing of the ToF spread arises from a decrease of the ions mean energy, demonstrating sympathetic cooling.

- **Numerical validation.** In section 3.3.1 we have numerically shown that the ions ToF distribution correlates with the energy distribution of the ions at the moment of extraction. This allowed us to map the ToF distributions to the initial thermal distributions, as shown in figure 3.20. Thereby the observed correlation is of the form $\sigma_{tof} \propto \sqrt{T}$, which is a consequence of setting the extraction potential as explained before. Thus, the ToF distribution spread does not depend on the spatial spread of the ion cloud but rather on its kinetic energy (or velocity) spread. The mapping is based on the fact that for this extraction potential, the ToF of one ion depends nearly linear on its velocity at the moment of extraction (see figure 3.18). Even though the absolute values of σ_{ToF} in the simulations (section 3.3.1) do not perfectly match with the measured ones, we observe $\sigma_{tof} \propto \sqrt{T}$ regardless of the extraction potential, as long as it meets the position-independent condition.

The expected ions energy distribution in our HAITrap after interacting with Helium at 300 K is shown in section 3.1.3, figure 3.6. Furthermore, we observed experimentally that the ToF spread reaches an equilibrium value, meaning a complete thermalization of the ions with the buffer gas at 300 K. Therefore, we assume that the measured ToF distribution without interaction with the atom cloud ($t = 0$ in figure 3.1.3) is a measurement for the ToF distribution at 300 K.

Assuming $\sigma_{tof} \propto \sqrt{T}$, we can now give a rough estimation on the final temperature of the ions. For example, in figure 3.1.3 we observe a narrowing of the ToF distribution by 60 %. Therefore, the lowest measured temperature of the ions in figure 3.23 is estimated to be in the order of 35 ± 5 K.

Ion heating due to background collisions

A further important characterization parameter for our experiment is the heating (or energy gain) caused by background collisions with the rest of the gas in the chamber. For measuring this, we first cool the ions via collisions with the ultra-cold rubidium cloud as explained before and stop the cooling process by turning off the darkSPOT. Thereafter the ions are stored for a few seconds, extracted and detected. The measured ToF distributions are plotted as a function of the storage time in the trap after cooling at different atom optical densities. The results are shown in figure 3.24. One clearly sees from the figure that the ToF spread increases with increasing ion storage time after the cooling process. Note

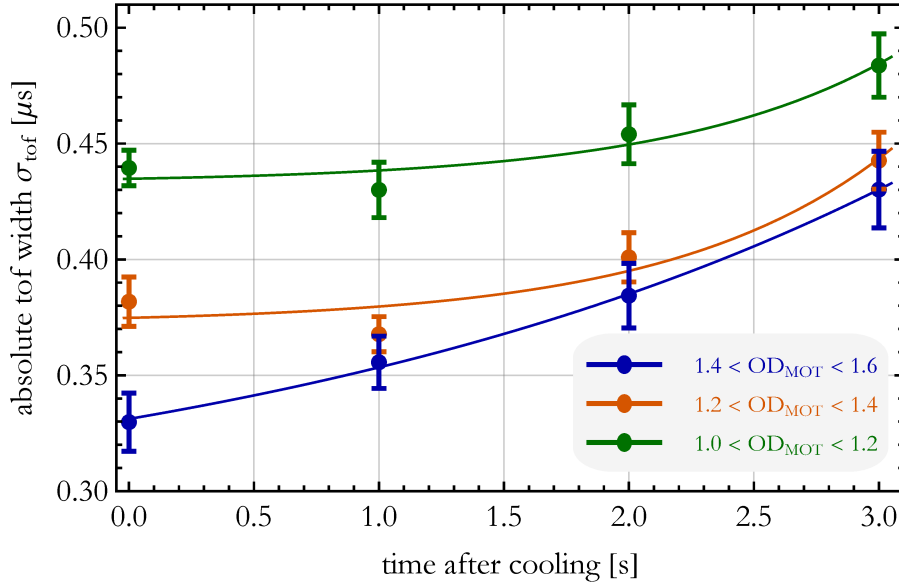


Figure 3.24: Ions background heating. After the ions interact with the atom cloud for 4 seconds, the darkSPOT is turned off. The ToF width is plotted as a function of the time after cooling. It is observed that the ToF spread increases due to heating caused by background gas collisions.

that background gas is the main origin of heating effect during cooling process. We assume that the most prominent heating effect is rf-collisional heating.

Cooling dynamics

In the context of thermodynamics, we can model the ion cooling dynamics via heat transfer. A simple well known model is the Newton's law of cooling. It states that the thermal energy change rate of an object is proportional to the temperature difference between the object and its surrounding thermal bath. This can be formally interpreted as a convection process, the differential equation of which is given by

$$\frac{d}{dt}Q = -\eta_Q(T_{\text{ion}}(t) - T_{\text{res}}) \quad (3.21)$$

with $Q \rightarrow$ thermal energy [J];
 $\eta_Q \rightarrow$ effective heat transfer coefficient [W/K];
 $T_{\text{res}} \rightarrow$ temperature of the energy reservoir [K];

Differentiating the definition of heat capacity as $C = dQ/dT$ with respect to

3 Sympathetic cooling of anions by ultra-cold atoms

the time one obtains

$$\frac{d}{dt}Q = C \frac{d}{dt}T_{\text{ion}}(t) \quad (3.22)$$

Setting this in equation 3.21 it yields

$$\frac{d}{dt}T_{\text{ion}}(t) = -\eta(T_{\text{ion}}(t) - T_{\text{res}}), \quad (3.23)$$

with $\eta = \eta_Q/C$ being a positive characteristic constant of the system with SI units [s^{-1}]. Assuming cooling ($T_{\text{ion}}(t=0) > T_{\text{res}}$), the coefficient η can be interpreted as the cooling efficiency of the system per unit time. Furthermore, the product $\eta \cdot T_{\text{res}}$ can be interpreted as a heating rate R_h . In this sense, $T_{\text{res}} = R_h/\eta$ is the effective final temperature the ions achieve due to the interplay of cooling and heating effects. This model has been used in a similar way in other works [31]. The solution to this differential equation is given by

$$T_{\text{ion}}(t) = (T_0 - T_{\text{res}})e^{-\eta t} + T_{\text{res}} \quad (3.24)$$

Assuming $\sigma_{\text{tof}}^2 \propto T$, we fit this equation to the data shown in figure 3.23. Thereby we let T_0 fixed, η and T_{res} are the free fitting parameters. The solid lines in this graph show the rescaled resultant fits. We observe an increase of the cooling efficiency coefficient from $\eta = 0.32s^{-1}$ to $\eta = 0.72s^{-1}$ with increasing atom optical density. As expected, increasing the atom density increases the number of collisions, leading to an increase of the cooling efficiency.

3.3.3 Emergence of non-thermal distributions

Until now we have interpreted the resultant ToF distributions using classical thermodynamics. In this way, we can use intuitive quantities, such as temperature, for describing the cooling dynamics of the ions. Nevertheless, we have shown in section 3.1.3 that we expect in our system deviations of thermal energy distributions which are rather well described by a Tsallis energy distribution. Indeed, such energy distributions have been shown for a hybrid trap system consisting on a linear paul trap and a magneto optical trap with $^{88}\text{Sr}^+ + ^{87}\text{Rb}$ [112]. In such works, Doppler spectroscopy has been used to detect deviations from thermal distributions.

In this section, this effect will be qualitatively described in our system via time of flight. For this aim, we follow the same procedure as described in figure 3.21, with two main differences: i) We place the ions in the right part of the trap (about two millimeters from the center) because in this region, the extraction potential linearly maps the ions ToF with both the ions initial position and velocity. This has the advantage that the high energy ions that are able to climb the highest part of the axial confining potential in both directions and are 'imaged' symmetrically onto the time of flight. Therefore, this part of the extraction

3 Sympathetic cooling of anions by ultra-cold atoms

potential is better suited to detect a change in the ion energy distributions from a Boltzmann to a Tsallis distribution. ii) We make the atom cloud bigger by reducing the dark state fraction of the atom cloud in comparison with that in section 3.3.2. This enhances the rf-collisional heating effect, but reduces the cooling efficiency because more reactive collisions take place, as seen in section 3.1.1.

In this experiment, we set only one fixed interaction time between ions (1.5 s) and atoms while keeping a fixed atom density and compare it with the case where the ions only interacted with a pulse of helium buffer gas at 300 K. More details on the experimental procedure as well as the measured time of flight distributions can be found in section 3.3.2. In figure 3.25 the measured time of flights for this experiment are shown as points. For fitting this data we make following analysis.

In section 3.1.3 we have shown that the final expected energy distributions in our hybrid trap system can be described by a Tsallis probability distribution. Additionally, it has been shown that these non-thermal distributions are reflected in the spatial domain with the same probability function as in the energy domain [25, 20]. Furthermore, for the used extraction potential in this experiment, we map the initial position of the ions in the trap (or the ions cloud spatial distribution) to the ToF distribution. In consequence, we expect that the ToF distributions have the same shape as they have inside the trap. Therefore, we define the probability P for an ion arriving at a given time t at the detector as:

$$P(t) \propto \frac{1}{\left(1 + \frac{(t-t_0)^2}{n \cdot \sigma_{Ts}^2}\right)^n}, \quad (3.25)$$

with t_0 being the mean ToF, σ the width of the distribution and n a Tsallis characteristic parameter. It can be shown, that for $n \rightarrow \infty$ the function converges to a Gaussian of the form

$$P(t) \propto e^{-\frac{(t-t_0)^2}{2\sigma_G^2}}, \quad (3.26)$$

whereas for small values of n , the function 3.25 shows a power law tail of the form $(t/\sigma)^{-2n}$.

In figure 3.25 both equations 3.25 and 3.26 are used to fit the data. The top graph shows the ToF distribution measured after the ions interacted with a buffer gas at 300 K. From our theoretical model (section 3.1.3) we expect the ions to be thermalized with this gas and the energy distribution to be normal distributed (equation 3.26). Following the above reasoning, the ToF distribution should also be a Gaussian. As expected for this case, the ToF data fits a Gaussian function with high accuracy (blue curve). By using the Tsallis function for fitting the data (orange curve), the fit algorithm provides a power law exponent of $n = 7.9$, which is high enough to be similar to a Gaussian.

The bottom graph shows the resultant ToF distributions after the ions interacted with the atom cloud for 1.5 s. The Gaussian fit provides a width of

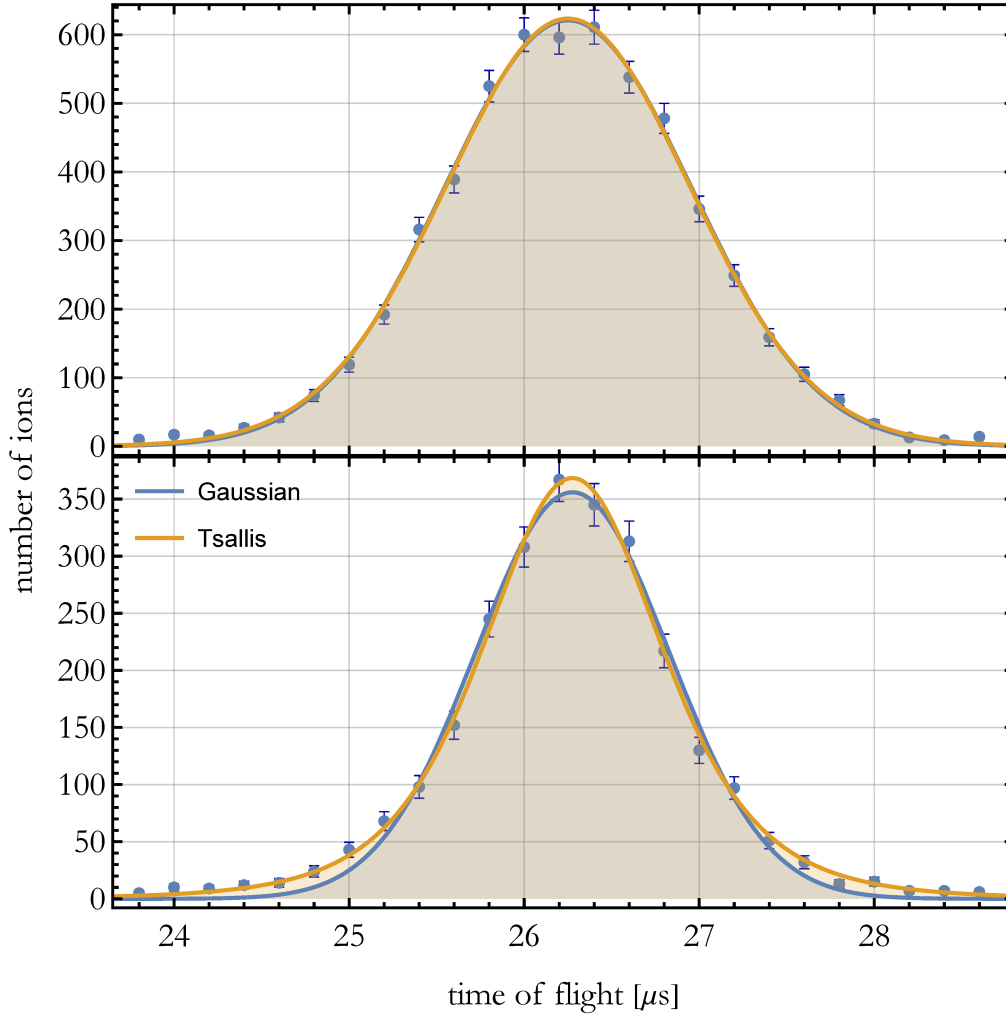


Figure 3.25: Emergence of non-thermal distributions measured via time of flight thermometry.

Top graph: ToF distribution measured after the ions interacted only with a buffer gas at 300 K. The solid lines represent two different fit functions. As expected for this case, no significant difference between the Tsallis (equation 3.25) and the Gaussian (equation 3.26) functions is observed.

Bottom graph: ToF distribution measured after the ions interacted with the atom cloud for 1.5 s. One observes a narrowing of the ToF distribution, but in contrast to the upper graph, the Tsallis function provides a better fit, specially at the wings of the distribution (see figure 3.26). This deviation is a consequence of the non-thermal distributions expected from our theory (see section 3.1.3).

3 Sympathetic cooling of anions by ultra-cold atoms

$\sigma_G = 0.55$ s, which is a narrowing of 75% in comparison with the upper graph. One can already observe that particularly at the wings of the distribution, the Gaussian fit does not describe the data as well as it did for the upper case. In contrast, by using the Tsallis function, the fit algorithms provide a power law exponent of $n = 2.8$, which is low enough for differentiating from a Gaussian. The data is better described by this function and in order to verify this, we performed a simple further statistical analysis.

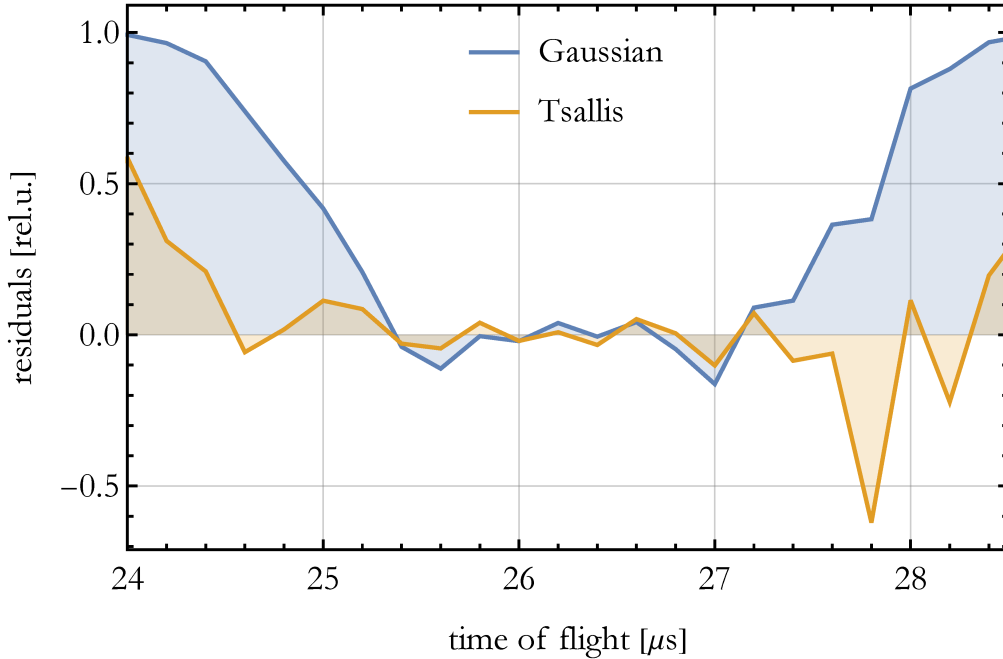


Figure 3.26: Relative residuals from the measured ToF distributions.

The graph shows the residual values for both fits as a function of the time of flight. Each residual value is normalized to the corresponding measured ion count. One observes that the data is in good agreement with both fits at the center of the distribution. On the contrary, at the wings of the distribution, the residuals from the Gaussian fit are all positive and show a non-random pattern, indicating that this model does not capture the whole information from the data. In contrast, the Tsallis fit function provides residuals with a random pattern along the whole ToF distribution.

For this aim we plot the residual values for both fits as a function of the time of flight in figure 3.26. In order to visualize the residuals more appropriately, each residual value is divided by the corresponding measured ion count for all ToF values. At the center of the distribution, both fits provide a random distribution around zero, which is expected from a function that fits the data accurately.

On the contrary, at the wings of the distribution, the residuals from the Gaussian fits are all positive and show a non-random pattern, indicating that this

3 Sympathetic cooling of anions by ultra-cold atoms

model does not inherit the whole information from the data. In contrast, the Tsallis fit function provides residuals with a random pattern along the whole ToF distribution. This indicates that the Tsallis function is a suitable model for the description of the measured ToF distributions. Provided that the ToF distribution maps the ion cloud's spatial distribution and therefore their energy distribution, the observed deviation in the ToF between a Gaussian and a Tsallis function can only be a consequence of the emergence of non-thermal distributions predicted in our theory.

Note that it is not possible to reconstruct the final energy distribution at the moment of extraction, as the time of flight just provide a 1D projection of an ensemble with 6 dimensions. Nevertheless, these results present clear evidence of the emergence of non-thermal distributions for our hybrid trap in the system $\text{OH}^- + \text{Rb}$.

4 Rotational quenching of molecular anions by ultra cold atoms

In the chapter 3 sympathetic cooling of negative ions in their translational degrees of freedom via elastic collisions with ultracold Rb atoms was demonstrated. Thereby, considerations of the internal structure of the anion could be neglected. In this chapter we demonstrate cooling of the internal degrees of freedom of a molecular anion via inelastic collisions with ultracold Rb atoms.

As already stated in the introduction of this thesis, the preparation and manipulation of cold molecular samples in their absolute ground state is of prime importance for physical research [2]. Such samples are used not only to study fundamental questions but also offer uncountable applications in other research areas.

Though laser cooling allows the preparation of ro-vibrational cold molecular ions [8], this method has the disadvantage that the cooling scheme is usually very complicated and has to be specifically customized for every particle to cool in order to find a closed optical cycle. For a long number of particles, it is even inapplicable.

Another, more general approach is the use of cryogenic systems, where the ion trap and the ion sample are cooled down to a few Kelvin with the use of a cold buffer gas. Helium gas is commonly used in these systems because of its high gas density at a few Kelvin, allowing efficient collisional cooling of both translational and rotational degrees of freedom [7, 10].

In such cryogenic systems, de-excitation of rotational states has been experimentally demonstrated for different molecular ions [113, 42]. Nevertheless, the main limitation of this approach is the temperature of the buffer gas. In the case of He the limit is about 5 K, which is the lowest temperature achievable for this gas. However, the measured rotational temperature measurements reported in these works are a few Kelvin above the one of the buffer gas. Although it is expected that the rotational distribution is in equilibrium with the effective collisional temperature [113], there is an ongoing discussion about the former effect, called incomplete rotational cooling [114]. As in the case for translational cooling, rotational quenching strongly depends on the properties of the trapping radio frequency field [113]. One of the reasons for this effect could be collision induced radio frequency heating.

Hybrid atom-ion trap systems overcome the upper limitations for the same reasons as discussed for translational cooling: i) the temperature of the buffer gas is many orders of magnitude lower than those achievable in cryogenic systems and ii) the buffer gas can be spatially localized arbitrarily within the radio frequency trap, specially in its middle where the radio frequency field amplitude

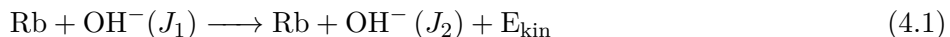
is at lowest, suppressing collision induced radio frequency heating.

Although in some cases the MOT-lasers interact with the ion sample leading to unwanted effects (e.g. photodissociation [115]), the use of a hybrid atom-ion is very advantageous for studying de-excitation processes. To date, only one research group has reported evidence for vibrational quenching of molecular ions in a hybrid trap system [116], whereas the experimental demonstration of rotational quenching in a hybrid trap has not been yet reported.

Our hybrid trap (see chapter 2) provides therefore an ideal setup to explore the current research gap on rotational quenching of molecular anions. In contrast to previous experiments, this system is capable of mixing negative charged ions with an ultra-cold cloud of neutral rubidium, opening a whole new experimental branch in quantum (chemical) physics.

Among many interesting molecular ions, for this work OH^- is chosen as the first system for proving rotational quenching. Besides playing a central role in organic, inorganic and atmospheric chemistry, OH^- is a well-established system for studying fundamental questions since it can be effectively modeled as a two-dimensional quantum rotor. Furthermore, the rotational detachment thresholds for this anion are experimentally advantageous because of its large rotational parameter [54]. Additionally, the great amount of experimental and theoretical data for this anion has made it for decades an ideal system [46, 47, 48, 49, 50, 51, 52, 53, 38, 39].

Moreover, theoretical calculations have shown that the system ($\text{OH}^- + \text{Rb}$) is advantageous for sympathetic cooling of the anions internal degrees of freedom, as it is expected to show large de-excitation rates [55, 56, 57]. In these works, the collisional (de)excitation of rotational states is treated as an inelastic collision where the molecular anion in a rotational state J_1 is excited or de-excited to another rotational state J_2 .



During such a collision, transitions between any rotational level are allowed, most likely being the ones with $J'' \rightarrow J'' \pm 1$. Collisions where the anion is de-excited ($J_2 < J_1$) are called rotational quenching.

It should be noted that during rotational quenching, the anion's excitation energy is redistributed as kinetic energy between both collision partners [56]. Given the fact, that OH^- is lighter than the neutral collision partner, it is more likely that the anion carries the most part of the released kinetic energy after such an inelastic collision. For example, already the lowest possible transition (from $J = 1$ to $J = 0$) releases an energy of $2 * B_0 = 37.48 \text{ cm}^{-1}$, meaning an equivalent temperature of about 54 K, whereas a transition from an excited state, e.g. $J = 6$ to $J = 5$ sets free an energy of equivalent temperature of 324 K. Therefore, the rotational quenching process can be accounted as a further heating and even loosing mechanism for translational cooling of OH^- .

In order to report the first experimental demonstration of rotational cooling of the molecular anion OH^- via inelastic collisions with an ultra-cold cloud of Rb atoms in a magneto optical trap, this chapter is organized as follows.

4 Rotational quenching of molecular anions by ultra cold atoms

First, we start modeling the internal structure of OH^- . This is done through several theoretical studies, specially the one described in [38] (supplementary material). A broad introduction on the electronic, vibration and rotation energies in molecules is given in section 4.1. A more specific treatment of the rotational structure of OH^- and its neutral partner OH is presented in section 4.1.1.

In order to measure the internal temperature of the trapped ion sample, we make use of a well-established technique called internal state photodetachment thermometry [117]. Thereby the ion cloud interacts with a laser beam of different wavelengths near the anions photodetachment threshold. This sort of action spectroscopy provides detailed information about the anions' internal structure and its rotational level population distribution. Therefore, it is necessary to model the OH^- expected photodetachment transition cross sections. This is discussed in section 4.1.2.

In our experiment, the anions also absorb/emit photons from/to its surroundings. This leads to a change in the rotational level distribution. Thus it is necessary to both qualitatively and quantitatively analyze the interaction of anions with the surrounding black body field. This is presented in section 4.1.3.

Following these procedures, we perform an analysis in section 4.2.1 on the dynamics of an OH^- ion cloud interacting simultaneously with a black body radiation field and a photodetachment laser. Thereby an experimental strategy for state selective detachment of the anion cloud and to probe the ion's rotational level distribution is established.

The former estimations are experimentally tested and presented in section 4.2.2. Thereby, the anion cloud interacts with a buffer gas (Helium at 295 K), after which a photodetachment laser is turned on at different wavelengths.

Finally, the experimental demonstration of rotational quenching is presented in section 4.2. This is done by allowing the ion cloud to interact with the ultra cold cloud of Rb atoms and applying state selective photodetachment spectroscopy. The experimental data and its analysis is presented. Furthermore, we apply a technique involving photodetachment spectroscopy that allows the preparation of absolute ground state molecular anions without the need of using cryogenic systems [42].

4.1 Internal structure of OH⁻

The method used in our experiment for measuring the internal state distribution of OH⁻ is based on the detachment of the electron from the molecular anion using photons with different energies. This is called photodetachment action spectroscopy and will be explained in detail in section 4.1.2. In order to characterize this process and the possible photodetachment transitions, we first need to consider the internal structure of both the molecular anion OH⁻ and its neutral partner OH.

In molecular physics, the internal structure of molecules is described by their electron shell, their geometrical configuration i.e. how the constituent atoms are placed in space and how they move in their rest frame relative to each other. For theoretical details about molecular physics, standard books like [118, 119] are recommended.

For a given molecular electronic shell configuration, there are several possible vibrational states, arising from the fact that the atoms in the molecule move in periodic motion relative to each other. Similarly, for each molecular vibrational state, the molecule can be in a certain rotational state, caused by the spinning of the constituent atoms relative to a given symmetry axis. In order to illustrate this for the case of OH⁻ and OH, a schematic chart of their energy level structure is shown in figure 4.1.

In this context, it is usual to describe a molecule's electronic configuration by its quantum numbers. Specifically for diatomic molecules, this is done using the following notation¹ [118]

$$|S, L, \Lambda, \Sigma, \Omega\rangle = {}^{2S+1} \Lambda_{\Omega} \quad (4.2)$$

with	S	→	Total electronic spin; = $\sum_i s_i$
	L	→	Total azimuthal quantum number; = $\sum_i l_i$
	Λ	→	orbital momentum projection quantum number; = $ M_L = 0 \leftrightarrow \Sigma, 1 \leftrightarrow \Pi, 2 \leftrightarrow \Delta, \dots$
	Σ	→	total spin projection quantum number; = $M_S = S, S - 1, \dots, -S$
	Ω	→	total angular momentum projection number; = $ \Lambda + \Sigma $
	$2S + 1$	→	State multiplicity.

For the case of OH⁻, the electronic shells of both atoms are completely filled out. Therefore, in its electronic ground state (labeled with X), the electronic quantum numbers S, L, Λ and Σ are zero. In consequence, the labeling for its

¹The fine structure states of the molecules are labeled using the Hund's case a) . Note that in this notation the greek letter Σ symbolizes at the same time an state with $\Lambda = 0$ and the projection of the total spin.

electronic ground state is written as $\text{OH}^- (X^1\Sigma_0)$. In the literature, Ω in many instances not explicitly specified as the sum of $(\Lambda + \Sigma)$ is also zero.

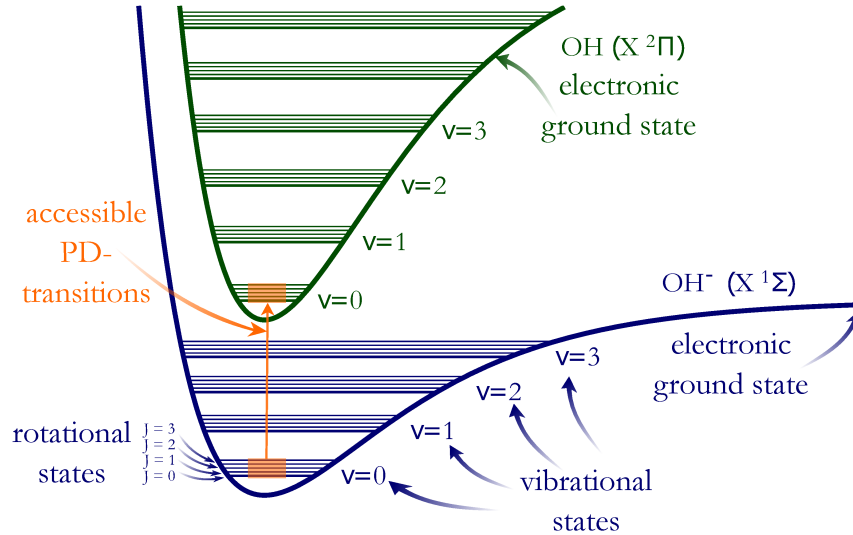


Figure 4.1: Schematic illustration of ro-vibrational energy levels for OH^- and OH . Within one electronic state, several vibrational states (ν_i) are possible. Similarly, for a given vibrational state several rotational states (J_i) are available. The photodetachment transitions accessible in our experiment are shown in orange and are plotted in more detail in figure 4.2.

For our experiment we assume that for the anion OH^- all vibrational states are frozen out. Therefore, in this work we focus our analysis on the rotational structure of $\text{OH}^- (X^1\Sigma_0)$ at its vibrational ground state $\nu = 0$ (section 4.1.1).

In contrast, the electronic valence shell in OH is not completely filled as one electron is missing. Therefore, in the electronic ground state its electronic quantum numbers are $S = 1/2, \Lambda = 1, \Sigma = \pm 1/2$. Subsequently, Ω take the values $1/2$ and $3/2$, meaning that the fine structure of the electronic ground state is not degenerate. These states are written down as $\text{OH}(X^2\Pi_{1/2})$ and $\text{OH}(X^2\Pi_{3/2})$.

The photodetachment process can be interpreted as a transition from $\text{OH}^- (X^1\Sigma_0)$ to $\text{OH}(X^2\Pi)$. Near threshold, this transition sets its neutral partner in its vibrational ground state $\nu = 0$, but in different rotational states depending on the photons energy. Therefore, in section 4.1.1 we make an analysis of the rotational structure of $\text{OH}(X^2\Pi)$ only in its vibrational ground state $\nu = 0$. The possible photodetachment transitions are schematically shown in 4.1 (orange) and are analyzed in detail in section 4.1.2.

4.1.1 Rotational structure of OH⁻ and OH

In this section we aim to provide an overview of the model used in this work to analyze the rotational structure of OH⁻ and OH in their vibrational ground state. This is a necessary tool for further modeling the possible photodetachment transitions, the photodetachment spectra of OH⁻ (section 4.1.2) and the interaction of OH⁻ with a black body radiation field (section 4.1.3). In these chapters, we follow the model presented in [38] (supplementary material), which makes an excellent review on the models available in the literature [48, 50, 120, 54].

Rotational energy levels of the hydroxide anion OH⁻

In spectroscopy, the rotational structure of molecules is conventionally described by the so called rotational term F . It is defined as the ratio of the rotational energy and the product of the Planck constant times the speed of light [92]. Historically, the most used unit for this term is cm⁻¹. For the case of the molecular anion OH⁻ ($X^1\Sigma$) this term can be modeled as [118]:

$$F(J'') \equiv \frac{E_{rot}}{hc} = B_0 J''(J'' + 1) - D_0 (J''(J'' + 1))^2 \quad (4.3)$$

with $J'' \rightarrow$ rotational quantum number,
 $E_{rot} \rightarrow$ rotational energy,
 $h \rightarrow$ Planck's constant,
 $c \rightarrow$ speed of light;
 $B_0 \rightarrow$ rotational constant;
 $D_0 \rightarrow$ centrifugal distortion correction constant.

Note that the rotational quantum number for OH⁻ is named as J'' . This is done in order to differentiate it from the rotational quantum number J' for OH

The term $B_0 J''(J'' + 1)$ in equation 4.3 originates from modeling the molecule as a quantum rigid rotor. Thereby it is assumed that the distance between the molecule's constituent atoms is constant. Nevertheless, in a rotating molecule the distance between the atoms is increased because of the centrifugal forces acting on it. Therefore, in order to correct such centrifugal effects, the term $D_0 (J''(J'' + 1))^2$ is included in equation 4.3.

In the bottom part of figure 4.2 a level scheme of the rotational structure described here is shown. Thereby, equation 4.3 was used and the rotational constants were taken from [50]. These are $B_0 = 18,74 \text{ cm}^{-1}$ and $D_0 = 2,05 \times 10^{-3} \text{ cm}^{-1}$.

For the later considerations on the photodetachment transitions, the parity of the wave function is another important parameter. In the case of OH⁻ ($X^1\Sigma$) this can be calculated as $P'' = (-1)^{J''}$.

Rotational energy levels of the hydroxide radical OH

The rotational structure for OH cannot be modeled as a rigid quantum rotor. This is because its orbital angular momentum and its total electronic spin couple to the rotational angular momentum. Therefore both fine structure states have to be treated separately.

For OH($X^2\Pi_{3/2}$) the rotational structure in the vibrational ground state can be described by the rotational term as [121, 38]

$$F1(J') = \frac{E_{rot}}{hc} = B_0 \left[\left(J' + \frac{1}{2} \right)^2 - \Lambda - \frac{\chi}{2} \right] - D_0 J'^4 \pm \frac{\Delta\nu_1}{2}, \quad (4.4)$$

and for OH($X^2\Pi_{1/2}$) as

$$F2(J') = \frac{E_{rot}}{hc} = B_0 \left[\left(J' + \frac{1}{2} \right)^2 - \Lambda + \frac{\chi}{2} \right] - D_0 (J' + 1)^4 \pm \frac{\Delta\nu_2}{2}, \quad (4.5)$$

with J' → rotational quantum number,
 B_0 → rotational constant,
 D_0 → centrifugal distortion correction,
 Λ → orbital momentum projection quantum number,
 $\Delta\nu_{1,2}$ → Λ doubling term.

Thereby the term χ is an abbreviation for

$$\chi = \sqrt{4 \left(J' + \frac{1}{2} \right)^2 + \Upsilon(\Upsilon - 4)}, \quad (4.6)$$

with $\Upsilon = A/B_0$, A being the spin orbit coupling constant for OH.

The lambda doubling term is given by

$$\Delta\nu_{1,2} = \pm \left(J' + \frac{1}{2} \right) \left[\frac{p + 2q}{2} \left(\pm 1 + \frac{2 - \Upsilon}{\chi} \right) + \frac{2q}{\chi} \left(J' + \frac{1}{2} \right) \left(J' + \frac{3}{2} \right) \right] \quad (4.7)$$

with $\Delta\nu_1$ → negative signs in equation,
 $\Delta\nu_2$ → positive signs in equation,
 p, q → Λ doubling parameters.

The rotational constants used here for OH are $B_0 = 18.55 \text{ cm}^{-1}$ and $D_0 = 1.92 \times 10^{-3} \text{ cm}^{-1}$. The spin orbit coupling constant is $A = -139.181 \text{ cm}^{-1}$. These values are taken from [122]. The lambda parameter values are $p = 0.235$ and $q = -0.039$ [123].

In the upper part of figure 4.2 the rotational level structure of OH is shown for both $^2\Pi_{3/2}$ (left) and $^2\Pi_{1/2}$ (right) states. The distance between the levels was calculated by means of equations 4.4 to 4.7. In both cases, the rotational levels with and without Λ splitting are shown. The Λ factor was multiplied by a factor of 100 in order to make the levels visible in this scale. In the graph, the parity for each Λ level is also denoted.

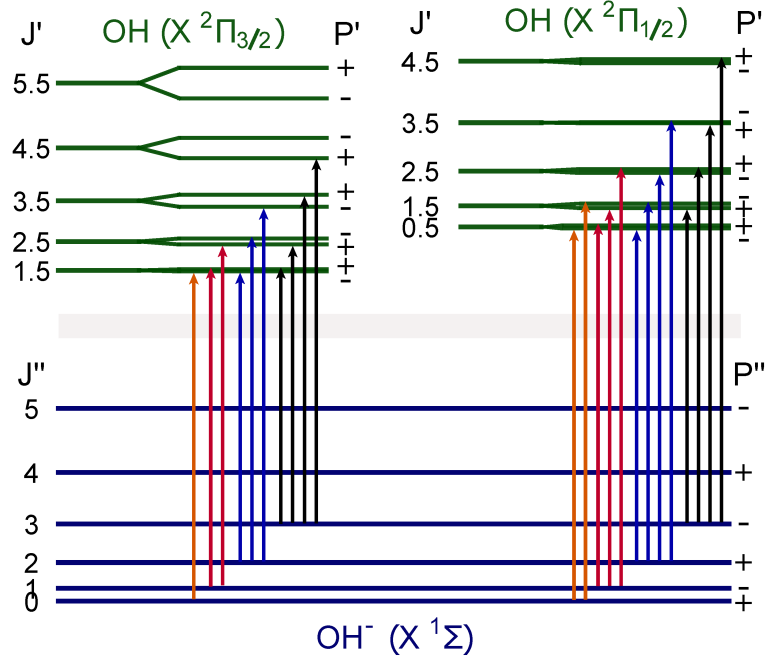
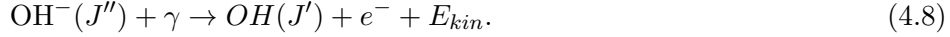


Figure 4.2: Rotational level scheme of OH^- and OH for the first rotational quantum numbers. The scaling distance between the rotational levels for OH^- is given by equation 4.3. For $\text{OH}(X^2\Pi_{1/2})$ equation 4.5 and for $\text{OH}(X^2\Pi_{3/2})$ equation 4.4 are used. The Λ -splitting in both fine structure states of OH were scaled up by 100 to make them visible. The horizontal gray line denotes that the energy distance between the levels of OH^- to OH is not to scale. The energy distance from $J'' = 0$ to $J'(\Pi_{3/2}^-) = 1.5$ defines the electron affinity of OH^- and is $\text{EA}_{\text{OH}^-} = 14\,741\text{ cm}^{-1}$.

Photodetachment transitions. All possible detachment transitions at $J'' = 0$ up to $J'' = 3$ are shown as vertical arrows. Thereby the selection rules described in equation 4.11 are used. The energy distance between the allowed transitions defines the corresponding photodetachment thresholds (equation 4.12), which are also shown in figure 4.3 with a proper scaling. The different arrow colors are arbitrary chosen for different initial J'' states.

4.1.2 OH⁻ photodetachment spectrum

In this section we aim to give an overview of the model for describing the interaction of the molecular anion OH⁻ with a photon γ of energy near the binding energy of the electron in the molecule. This interaction process is called *photodetachment* if it leads to following reaction path:



This reaction path is open only if the photon's energy $\hbar\omega_\gamma$ is high enough to detach the electron out of the molecule. The minimal photon's energy for allowing photodetachment is called threshold energy. This energy depends on the anion's rotational state J'' at the time of the interaction. Furthermore, after photodetachment, the neutral partner OH will remain in a certain rotational state J' , which depends on i) the photon's energy and ii) the initial rotational J'' state of OH⁻. Moreover, the final rotational state J' follow definite transition rules that depend on J'' . The minimal photon's energy for leaving the molecule OH in a given allowed state J' is called likewise threshold energy.

Allowed photodetachment transitions and threshold energies

A well established model for the allowed rotational photodetachment transitions in OH⁻ assumes a so called two step process [124]. Thereby, the photon is first absorbed by the anion, exciting it to a $X^1\Pi$ state. As this transition happens within the same electronic state, the allowed rotational transitions in this first step are [118]

$$\Delta J_i = 0, \pm 1. \quad (4.9)$$

In the second step, the electron auto-detaches from the molecule, leaving the neutral OH in the electronic state $X^2\Pi_\Omega$. Its final rotational state is then given by

$$J' = J'' + \Delta J_i \pm l \pm s \quad (4.10)$$

with $l \rightarrow$ electron's angular momentum,
 $s \rightarrow$ electron's spin.

For the electron it is assumed that only s-wave ($l = 0$) contributions are present, as the detached electron has small kinetic energy when leaving the molecule near threshold. The total change on the rotational momenta is therefore given by

$$J' - J'' = \pm 3/2, \pm 1/2. \quad (4.11)$$

All possible photodetachment transitions for the first 4 rotational levels ($J'' = 0$ to $J'' = 3$) of OH⁻ are shown in figure 4.2. In contrast to the higher rotational levels, the lowest one ($J'' = 0$) has only 3 possible transitions, resulting in 3

4 Rotational quenching of molecular anions by ultra cold atoms

different threshold energies. As J'' increases, more threshold channels open for the different rotational states. The maximum number of possible rotational transitions is 8, which is the case for $J'' \geq 3$.

The transition energy from the lowest rotational state of OH^- to the lowest one of OH ($J'' = 0 \rightarrow J'(\Pi_{3/2}^-) = 1.5$) is defined as the electron affinity of the molecule as $\text{EA}_{\text{OH}^-} = 14\,741 \text{ cm}^{-1}$ [38]. Relative to this, the energy difference from the initial to the final state is described by

$$\Delta F_{PD} = \text{EA}_{\text{OH}^-} + F(J'') - F_{1,2}(J'). \quad (4.12)$$

Thereby, the rotational terms F are given by equations 4.3, 4.4 and 4.5.

Photodetachment cross sections

Given the model for calculating the photodetachment threshold energies for every allowed transition (equation 4.12), the next step is to model the photodetachment cross section as a function of the photon energy E_γ near such a threshold. This is best described by estimating the cross section of the photodetachment process and its transition strength (reaction path 4.8).

Let us first analyze the photodetachment cross section behavior of one transition with one defined threshold energy E_0 . The most common model used for this case is the so called Wigner law [125]. In this model, the photodetachment cross section is zero below the threshold energy E_0 , as the photon's energy E_γ is not enough to detach the anion's electron. Above the threshold energy E_0 , the energy dependence of the photodetachment cross section is given by

$$\sigma_{PD,W} \propto (E_\gamma - E_0)^{l+1/2}, \quad (4.13)$$

with l being the angular momentum carried by the electron, in our case $l_e = 0$. Nevertheless, it has been shown that this law has to be slightly modified in order to take into account other types of interactions between the departing electron and the molecule (e.g electron-dipole interaction) [126, 127]. In this case, the cross section dependence is written as [128, 129]

$$\sigma_{PD,modW} \propto (E_\gamma - E_0)^\rho \quad (4.14)$$

with ρ being the modified Wigner law's threshold exponent, which is system specific. For the case of OH^- it is still in debate which threshold scaling law factor ρ describes the experimental data more effectively. In many works the exponents ρ have been chosen in an empirical way [46, 48, 50, 51, 117].

Furthermore, it has been experimentally observed, that the photodetachment cross section decreases far above the threshold energy. This has been also modeled in an empirical way as

$$\sigma_{PD} \propto \sigma_{PD,modW} \left(\frac{E_\gamma}{E_n} \right)^{\rho_f - \rho} \quad (4.15)$$

4 Rotational quenching of molecular anions by ultra cold atoms

with ρ_f being the far-above threshold exponent.

As shown previously, for every J'' state there are several allowed rotational transitions to the intermediate state. This means that for every J'' state there are as many threshold energies as allowed transitions. Additionally, it is well known that rotational transitions in molecules have different transition intensities I . This effect is taken into account in this model by assuming that the photodetachment cross section is proportional to the intensity of the rotational transition. These intensities can be calculated by means of the so called Hönl-London factors [130], which for our model are weighted with the degeneracy of states in the anion ($2J'' + 1$) [50, 54, 38]. In total, by adding the cross sections for every allowed rotational transition from J'' one obtains the energy dependence of the photodetachment cross section for a given initial rotational state J'' :

$$\sigma_{pd,J''}(E_\gamma) \propto \sum_n \frac{I_n}{2J'' + 1} (E_\gamma - E_n)^{\rho_n} \left(\frac{E_\gamma}{E_n} \right)^{\rho_f - \rho_n}, \quad (4.16)$$

with $n \rightarrow$ rotational transition labeling,
 $I_n \rightarrow$ relative intensity of n'th transition,
 $E_n \rightarrow$ threshold energy of n'th transition,
 $\rho_f \rightarrow$ far-above threshold exponent,
 $\rho_n \rightarrow$ threshold exponent of the n'th transition.

This model is plotted in figure 4.3 for the four first rotational levels J'' of OH^- . Here, we choose $\rho_f = -2.8$ $\rho_n = 0.2$ as in reference [38]. Furthermore, in order to make the photodetachment cross section appear in relative units, the curves are normalized with the value of $\sigma_{pd,J''=0}$ at a wavelength of known cross section $\nu_{pd,0}$. In this way the curves can be rescaled with experimental values of the absolute cross section at $\nu_{pd,0}$ (e.g. $\sigma_{abs,15\,108\text{cm}^{-1}} = 8,5 \cdot 10^{-18} \text{ cm}^2$ [53]). The energies for the corresponding thresholds are shown as vertical lines and calculated as discussed above (see equation 4.12). The colors chosen are the same as in figure 4.2.

As already mentioned in the analysis of the different transitions, there are 3 allowed rotational transitions for the rotational ground state of OH^- ($J'' = 0$), making 3 threshold contributions in the cross section's energy dependence. In contrast, for ($J'' = 3$) there are 8 possible transitions, opening 8 different threshold contributions in the cross section's energy dependence (see also figure 4.2).

4 Rotational quenching of molecular anions by ultra cold atoms

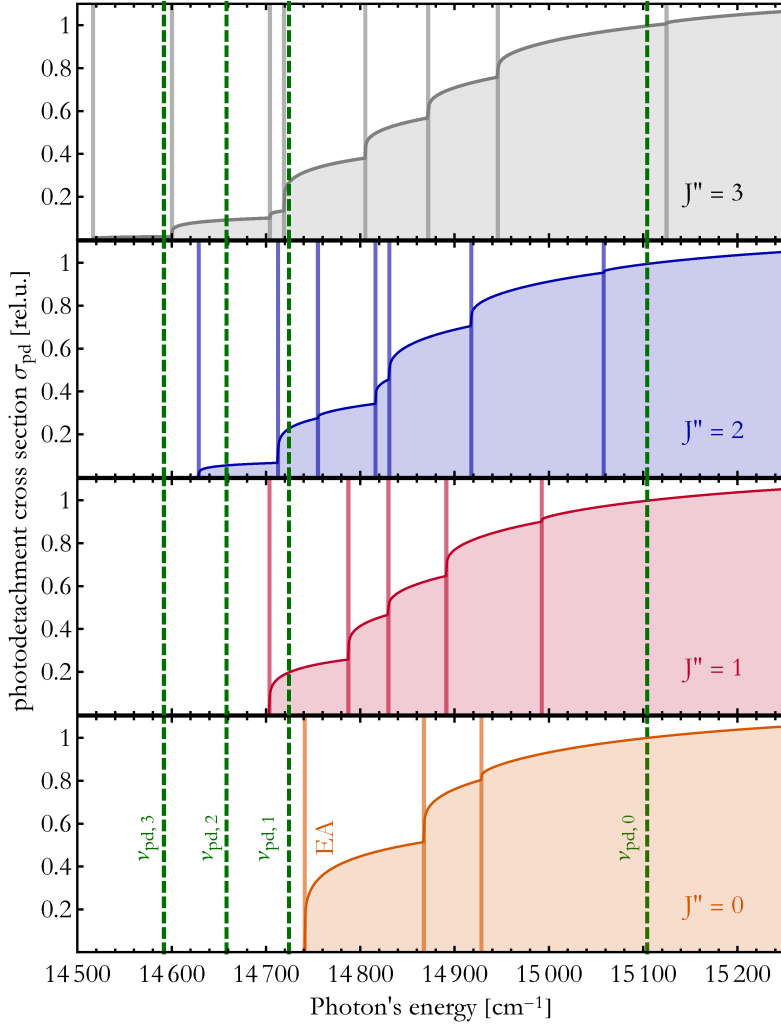


Figure 4.3: Energy dependence of the OH^- photodetachment cross section. The photodetachment cross section for different rotational levels J'' of OH^- is plotted as a function of the photon's energy (equation 4.16). The curves are normalized with the value of $\sigma_{pd, J''=0}$ at $\nu_{pd,0}$, such that they appear in relative units and can be rescaled with experimental values of the absolute cross section at this wavelength, e.g. $\sigma_{abs, 15108 \text{ cm}^{-1}} = 8,5 \cdot 10^{-18} \text{ cm}^2$ [53]. The different threshold energies for the allowed photodetachment transitions are marked as vertical lines (Same color coding as in figure 4.2). For $J'' = 0$ (orange) there are 3 possible transitions, making 3 threshold contributions in the cross section. The lowest threshold energy at $J'' = 0$ is defined as the electron affinity (EA) of OH^- . For $J'' = 3$ (gray) all possible rotational transition channels are open (8 threshold contributions). The green dashed vertical lines correspond to the probing photodetachment laser frequencies ν_i described in section 4.2.

4.1.3 Interaction of OH⁻ with black-body radiation

Another important process for characterizing the internal state distribution of the molecular anion cloud is its interaction with the surrounding radiative field, also known as black body radiation. This electromagnetic radiative field can be described by its spectral energy density (energy per volume and per frequency interval) given by the Planck's radiation law [118]

$$\begin{aligned}\rho(\nu) &= \frac{8\pi h\nu^3}{c^3} n_\gamma(\nu, T) \\ &= \frac{8\pi h\nu^3}{c^3} \frac{1}{e^{h\nu/(k_B T)} - 1},\end{aligned}\tag{4.17}$$

with

$\rho(\nu)$	→	spectral energy density,
ν	→	photon's frequency,
h	→	Planck's constant,
c	→	speed of light,
$n_\gamma(\nu, T)$	→	Bose-Einstein photon occupation number,
k_B	→	Boltzmann constant,
T	→	black body temperature.

A molecule interacts with such a field by absorbing and emitting photons at certain rates. The molecule hereby changes its rotational state from J''_i to J''_k , where $k > i$ is chosen for the following discussion. In the first case (absorption), the average probability W per second (transition rate κ) that OH⁻ in a rotational level J''_i absorbs a photon with energy $h\nu = (E_k - E_i)$ is proportional to the number of photons γ_ν per second that interact with the molecule:

$$\left(\frac{dW_{i\rightarrow k}}{dt}\right)_{abs} = B_{i\rightarrow k}\rho(\nu) \equiv \kappa_{i\rightarrow k}^{abs}\tag{4.18}$$

where the proportional factor $B_{i\rightarrow k}$ is defined as the Einstein absorption coefficient for the transition $J''_i \rightarrow J''_k$.

Similarly, the radiation field can stimulate the emission of a photon from the molecule, relaxing its rotational state. In this case, the average probability W per second that OH⁻ (in a rotational level J''_k) emits a photon with energy $h\nu = (E_k - E_i)$ is proportional to the number of photons γ_ν per second that interact with the molecule

$$\left(\frac{dW_{k\rightarrow i}}{dt}\right)_{sti} = B_{k\rightarrow i}\rho(\nu) \equiv \kappa_{k\rightarrow i}^{sti}\tag{4.19}$$

where the proportional factor $B_{k\rightarrow i}$ is the Einstein emission coefficient for the transition $J''_k \rightarrow J''_i$ with ($k > i$).

In contrast, if a molecule is in a high energetic rotational state J''_k , it will emit a photon spontaneously, i.e without the influence of the radiation field. In this case, the probability per second of the molecule emitting a photon with the energy $h\nu = (E_k - E_i)$ is directly given by the Einstein coefficient for spontaneous

4 Rotational quenching of molecular anions by ultra cold atoms

emission $A_{k \rightarrow i}$

$$\left(\frac{dW_{k \rightarrow i}}{dt} \right)_{spo} = A_{k \rightarrow i} \equiv \kappa_{k \rightarrow i}^{spo}. \quad (4.20)$$

It can be shown [118] that the Einstein coefficients are related via

$$\begin{aligned} B_{i \rightarrow k} &= \frac{g_k}{g_i} B_{k \rightarrow i} \\ A_{k \rightarrow i} &= \frac{8\pi h \nu^3}{c^3} B_{k \rightarrow i} \end{aligned} \quad (4.21)$$

where $g_{k,i} = (2J''_{k,i} + 1)$ is the statistical weight of the molecular state. With these relations the transition rates for both emission processes (equations 4.19 and 4.20) can be written as

$$\kappa_{k \rightarrow i}^{em} = \kappa_{k \rightarrow i}^{sti} + \kappa_{k \rightarrow i}^{spo} = A_{k \rightarrow i} (1 + n_\gamma) \quad (4.22)$$

For the case of spontaneous emission, the Einstein coefficient can be calculated for dipole transitions as

$$A_{k \rightarrow i} = \frac{2}{3} \frac{e^2 \omega_{k \rightarrow i}^3}{\epsilon_0 c^3 h} \left| \int \Psi_k^* \cdot \vec{r} \cdot \Psi_i \cdot dx dy dz \right|^2 \quad (4.23)$$

with $e \rightarrow$ elementary charge,
 $\omega_{i \rightarrow k} \rightarrow$ transition's angular frequency,
 $\approx 2\pi \cdot 2B_0(J''_i + 1)$,
 $\epsilon_0 \rightarrow$ vacuum permittivity,
 $h \rightarrow$ Plank's constant,
 $c \rightarrow$ speed of light,
 $\Psi_{i,k} \rightarrow$ i,k state's wave function,
 $\vec{r} \rightarrow$ electron's displacement vector.

The second term of this equation is called the matrix element for the transition $i \rightarrow k$. For pure rotational transitions this expression is given by

$$A_{k \rightarrow i} = \frac{2}{3} \frac{\omega_{k \rightarrow i}^3}{\epsilon_0 h} \mu_0^2 \frac{J''_k}{2J''_k + 1} \quad (4.24)$$

where μ_0 is the internuclear electric dipole moment of the molecule.

For the absorption process, the transition rate 4.18 can be calculated with equations 4.21 and 4.24 as

$$\kappa_{i \rightarrow k}^{abs} = A_{k \rightarrow i} \cdot n_\gamma(\nu_{i \rightarrow k}, T) \cdot \frac{2J''_i + 3}{2J''_i + 1}. \quad (4.25)$$

In figure 4.4 the calculated rates for the absorption and emission processes are compared. For calculating the different rates, equations 4.22 and 4.25 are used. For the black body field, a temperature of 300 K was assumed. The x axis shows the initial rotational level of the molecule, whereas the y axis is plotted with a logarithmic scale in order to compare both graphs in a better way.

4 Rotational quenching of molecular anions by ultra cold atoms

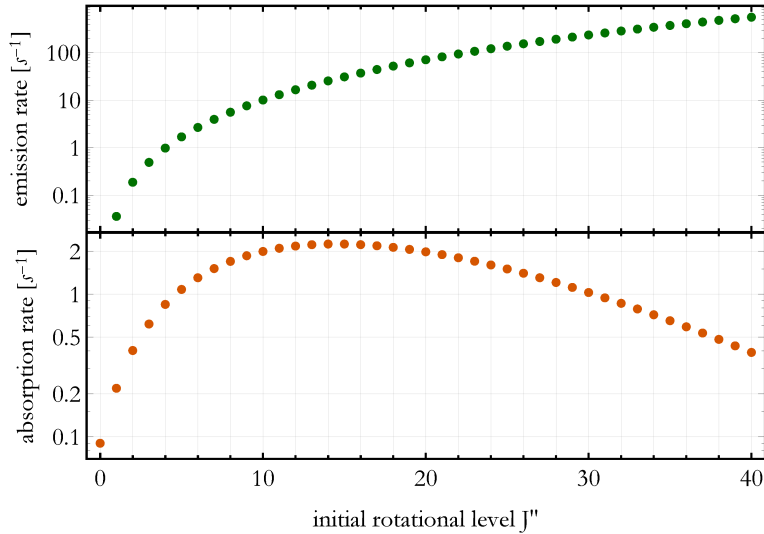


Figure 4.4: OH⁻ photon's emission and absorption rates for a black body field of $T = 300$ K as a function of the initial rotational levels J'' . The graph shows the case of pure rotational transitions where OH⁻ goes from the initial rotational state $J'' \rightarrow J'' + 1$ for absorption or from $J'' \rightarrow J'' - 1$ for emission.

For benchmarking the model obtained here, we look into the change on the relative populations for an molecular cloud at a given rotational temperature T_0 interacting with a black body field at 300 K. The occupation number $N(J'')$ of a rotational level J'' in thermal equilibrium can be described by Boltzmann statistics as

$$N(J'') = (2J'' + 1) \cdot e^{-\frac{E_0 \cdot (J''(J''+1))}{k_B T_0}}. \quad (4.26)$$

Since we assume that all ions are in the electronic-vibrational ground state, we can describe the system with the relative population p of a specific level. This is given by the occupation number of the level J'' weighted with the total number of ions

$$p_{J''} = \frac{N(J'')}{\sum_{J''} N(J'')}. \quad (4.27)$$

Given this thermal distribution, we let the anion cloud at a given rotational temperature T_0 interact with the black body field. For this, we model the change on the relative populations with following differential rate equation

$$\frac{dp_{J''_i}}{dt} = -\left(\kappa_{i \rightarrow i+1}^{abs} + \kappa_{i \rightarrow i-1}^{em}\right) \cdot p_{J''_i} + \kappa_{i-1 \rightarrow i}^{abs} \cdot p_{J''_{i-1}} + \kappa_{i+1 \rightarrow i}^{em} \cdot p_{J''_{i+1}} \quad (4.28)$$

with the absorption and emission rates from equations 4.22 and 4.25 (see figure 4.4). $p_{J''_i}$ describes the initial population in level J''_i . The first term of this

4 Rotational quenching of molecular anions by ultra cold atoms

differential equation describes the depopulation of level J_i'' to the upper or lower states via photon absorption or emission. The last two terms describe the repopulation of level J_i'' due to absorption of a photon of a molecule in the lower state or the emission of a photon from a molecule being in the upper state.

For solving this system, we choose an upper limit of $J_{max}'' = 40$, setting zero for its Einstein coefficient. Figure 4.5 shows the solution of equation 4.28 as a benchmark of the former described model for the interaction of a molecular ensemble with black body radiation.

The left graph show the population distribution of the rotational levels for different scenarios. The red and the blue curves are calculated with equations 4.26 and 4.27. The blue curve is the distribution taken as the initial conditions for solving the coupled differential equation 4.28. The green curves show the redistribution of the rotational levels for different times. One sees that the differential equation converges for $t \rightarrow \infty$ to a Boltzmann distribution of 300 K.

The right graph shows the dynamical redistribution of single rotational levels from $J'' = 0$ to $J'' = 3$. At $t = 0$ the population distribution is a thermal one with $T = 20$ K. The different curves are the solution of equation 4.28.

In the former example, we have shown thermalization by initializing the rotational levels with a certain Boltzmann distribution at $T = 20$ K. We have also proven that regardless of the initial population distribution of the rotational levels (e.g all ions being in $J'' = 5$), the differential equation 4.28 ensures a final thermal distribution of the rotational levels at $T = 300$ K.

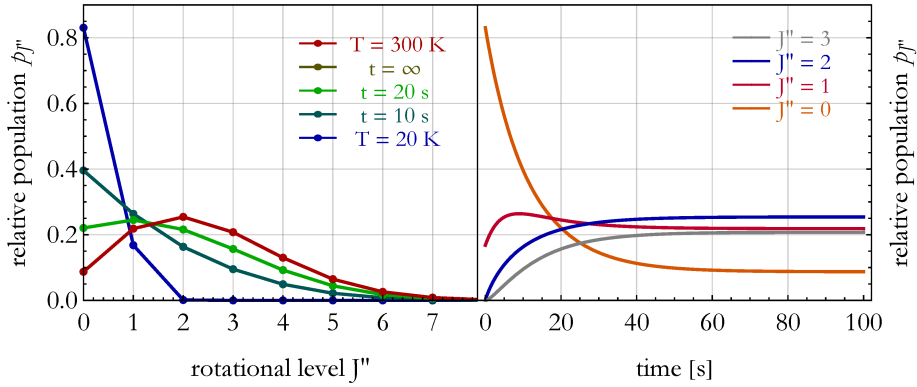


Figure 4.5: Benchmarking the model for black body redistribution.

Left: Rotational level distribution. The points show the values for different normalized level populations as a function of the rotational levels (lines are for the reader's optical help). The blue and the red distributions are calculated using Boltzmann statistics (equation 4.27). The green curves show the evolution of the population redistribution from 20 K to 300 K for different times (equation 4.28). For $t \rightarrow \infty$ the distribution converges to 300 K. Therefore, both distributions are not distinguishable on the graph.

Right: Dynamical redistribution of the first 4 rotational levels. At $t = 0$ the ions start with a Boltzmann distribution of $T = 20$ K. The black body field has a temperature of $T = 300$ K. The different curves show the solution of equation 4.28 for different rotational levels.

4.2 Rotational thermometry via state selective photodetachment

In this section, we report the observation of rotational cooling of trapped molecular anions OH^- by ultra cold Rb atoms in our hybrid trap.

For this aim, we estimate the effect for an OH^- ion cloud at different rotational temperatures interacting *at the same* time with i) a photodetachment laser (section 4.1.2) and ii) a black body radiation field (section 4.1.3). Based on this analysis we explain the method for rotational thermometry used in this work, called state selective photodetachment (section 4.2.1). We apply this method subsequently for measuring the rotational distribution of a trapped ion cloud after the interaction with: i) a buffer gas at room temperature (section 4.2.2) and ii) an ultra cold buffer gas (section 4.2.3).

4.2.1 State selective photodetachment

Let us first analyze the interaction of an OH^- ion cloud with a laser field. In contrast with section 3.2.2, in this section we take into account the internal structure of our ion. In our setup, the photodetachment process



occurs at a certain rate that depends on several experimental parameters: the laser frequency, its power, the ions rotational state J'' and the geometrical overlap between the ion cloud and the laser beam.

Since the OH^- photodetachment cross section is J'' -specific, it is important to first look at the dynamical change of the relative ion populations $p_{J''}(t)$ under the influence of a laser field. Thus, we assume that this dynamical change $dp_{J''}(t)/dt$ is proportional to the relative ion populations at a given time $p_{J''}(t)$. This can be modeled by means of the following differential equation [53, 52]:

$$\frac{dp_{J''}(t)}{dt} = -\sigma_{pd,J'',\nu} \cdot \iiint F_{\gamma}(x, y, z) \cdot n(x, y, z) \cdot p_{J''}(t) \, dx \, dy \, dz \quad (4.29)$$

with $p_{J''} \rightarrow$ ions relative population in J'' (equation 4.27),
 $\sigma_{pd,J'',\nu} \rightarrow$ absolute photodetachment cross section
for OH^- in J'' at the laser frequency ν ,
 $F_{\gamma}(x, y, z) \rightarrow$ photon flux density distribution,
 $n(x, y, z) \rightarrow$ ions geometrical distribution in space.

In order to solve the differential equation 4.29 we first work out the geometrical overlap integral by making following simplifications.

For the ion cloud spatial distribution we assume that: i) The ion cloud is very dilute and is at thermal equilibrium. Therefore, the ion cloud shape can be described by a single particle density distribution given only by the shape of the trapping potential. ii) The ion cloud shape is independent of the ions rotational level. With these assumptions, the integration in dz of this term

4 Rotational quenching of molecular anions by ultra cold atoms

yields unity times the projection of the 3D single-particle density distribution onto the (x,y) plane. This projection is called single-particle column density distribution $\rho(x, y)$.

For the photon flux density distribution we assume that: i) z is the laser's propagation direction and it is constant along this path. Therefore, the integration in dz yields the number of photons per second that go through the (x,y) plane. ii) the laser beam is much smaller in size than the ion cloud. In consequence, the geometrical dependency in x and y directions of the laser are negligible. A delta distribution at the point (x_γ, y_γ) models this geometrical distribution. With this assumptions we can write for the photon flux

$$F_\gamma(x, y, z) = \frac{P_\gamma}{h\nu} \delta(x - x_\gamma) \delta(y - y_\gamma). \quad (4.30)$$

with $P_\gamma \rightarrow$ laser beam power [W],
 $h\nu \rightarrow$ photon energy [J],
 $\delta(x; y) \rightarrow$ Dirac delta function [1/m],
 $x_\gamma, y_\gamma \rightarrow$ laser beam position relative to the ion cloud [m].

Setting equation 4.30 in 4.29, one can easily solve the overlap integral. Integrating the two remaining dimensions dx and dy yields the single particle column density $\rho(x_\gamma, y_\gamma)$ evaluated at the relative laser position (x_γ, y_γ) . Equation 4.29 become:

$$\frac{dp_{J''}}{dt} = - \underbrace{\sigma_{pd, J'', \nu} \cdot \frac{P_\gamma}{h\nu} \cdot \rho(x_\gamma, y_\gamma)}_{\kappa_{pd, \nu, J''}} \cdot p_{J''} \quad (4.31)$$

The photodetachment cross section can be estimated as shown in section 4.1.2 (see figure 4.3), yielding

$$\kappa_{pd, \nu, J''} = \frac{P_\nu}{h\nu} \cdot \rho(x_\gamma, y_\gamma) \cdot \sigma_{pd}^{abs} \cdot \sigma_{pd, \nu}^{rel}, \quad (4.32)$$

with the relative photodetachment cross section calculated with equation 4.16 and its absolute value ($\sigma_{abs, 15\ 108\ \text{cm}^{-1}} = 8, 5 \cdot 10^{-18}\ \text{cm}^2$) taken from [53]. In figure 4.6 a set of examples for photodetachment rates are plotted as a function of the ions rotational level for different photodetachment laser frequencies (marked in figure 4.3) and typical experimental values. Thereby we chose $P_\nu = 100\ \text{mW}$ and $\rho(x_\gamma, y_\gamma) = 10\ \text{ions/cm}^2$.

The solution to the differential equation 4.31 is an exponential function with the decay rate $\kappa_{pd, \nu, J''}$:

$$p_{J''}(t) = p_{J'', t=0} \cdot e^{-\kappa_{pd, \nu, J''} \cdot t} \quad (4.33)$$

with $p_{J'', 0}$ being the initial ions population in J'' . This is given given by equation 4.26 and 4.27 for the case of a thermal distribution.

4 Rotational quenching of molecular anions by ultra cold atoms

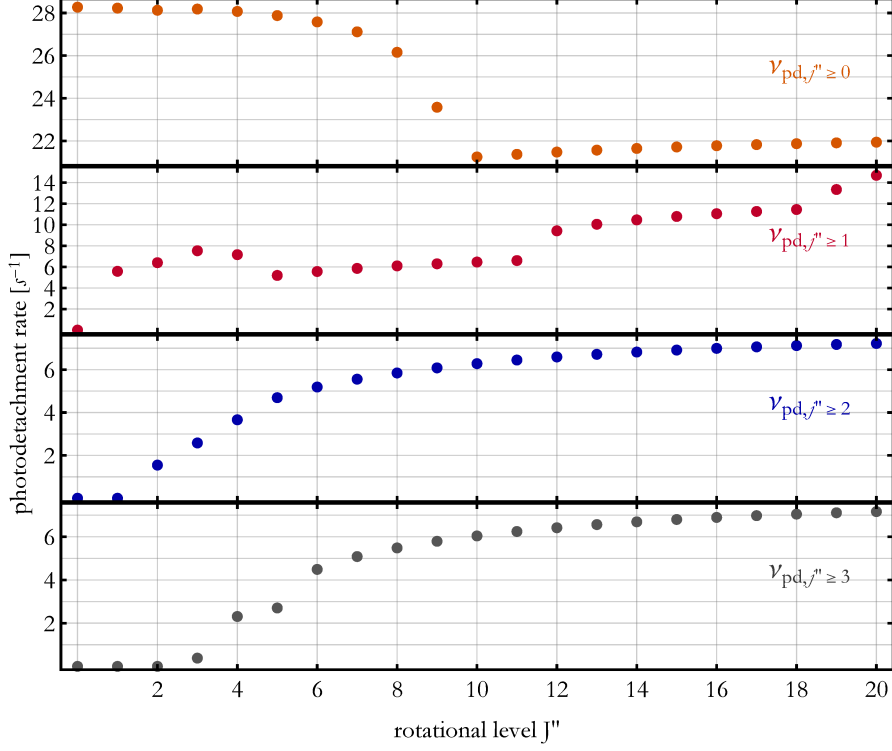


Figure 4.6: Photodetachment rates as a function of the rotational levels J'' . The values are estimated with equation 4.32 for the different photodetachment laser frequencies $\nu_{pd, J''}$ marked in figure 4.3. The chosen experimental values are $P_\nu = 100$ mW, $\rho = 10$ ions/cm² and $\sigma_{abs} = 8,5 \cdot 10^{-18}$ cm². The relative photodetachment cross sections as well as the chosen frequencies $\nu_{pd, J''}$ are shown in in figure 4.3.

Nevertheless, as described in section 4.1.3, the ions interact with black body radiation during the photodetachment process. In order to take this into account, we combine equations 4.28 and 4.31, yielding following set of coupled differential equations

$$\frac{dp_{J''}}{dt} = -\kappa_{bb}^{out} \cdot p_{J''} + \kappa_{bb}^{in} \cdot p_{J'' \pm 1} - \kappa_{pd, \nu_{pd, J''}} \cdot p_{J''}. \quad (4.34)$$

In this equation, κ_{bb}^{out} summarizes the depopulation rates of the rotational level J'' via absorption or emission of a photon due to black body interaction. Similarly, κ_{bb}^{in} sums up the repopulation of J'' from the neighboring rotational levels due to absorption of a black body photon from $J'' - 1$ or the emission of a photon from $J'' + 1$ (see equation 4.28 and figure 4.4). The loss rate due to photodetachment is written as $\kappa_{pd, \nu_{pd, J''}}$ (equation 4.32 and figure 4.6). The initial ion relative population in J'' are given by equation 4.26 and 4.27 for the case of a thermal distribution.

4 Rotational quenching of molecular anions by ultra cold atoms

In the experiment, the measurable quantity is the number of ions that remain trapped after interaction with the photodetachment laser. By normalizing this quantity by the number of ions detected without photodetachment laser, the experimental values can be compared with the sum of the different rotational populations calculated as

$$p_{total}(t) = \sum_{J''} p_{J''}(t) \quad (4.35)$$

with $p_{total}(t = 0) = 1$.

Figure 4.7 show the dynamical time evolution of different relative rotational populations (different colors) using the calculated rates shown in figure 4.4 and 4.3. Thereby equation 4.34 is solved numerically and the total relative population is calculated with equation 4.35 (green solid curve). Shown are the cases for three different initial rotational temperatures (from up to down: 20, 150 and 300 K calculated with 4.27) and two different photodetachment laser frequencies. In the left side of the figure, the case where all ions are detached ($J'' \geq 0$) is shown, whereas in the right side the case where only ions present in ($J'' \geq 2$) are detached is presented.

For the case of $\nu_{J'' \geq 0}$, one observes that the total decay rate does not depend on the initial rotational temperature, as expected from experimental observations [53]. Furthermore, for the case of the chosen experimental parameters, black body radiation does not play an important role in the ion losses since the photodetachment rates (figure 4.6) are at least one order of magnitude larger than the corresponding black body interaction rates (figure 4.4). The black dashed line represents an exponential fit to a sampling of the green curve (time evolution of the total relative population) for $t \leq 1/\kappa_{pd, \nu_{J''=0}}$. The fitted decay rate is $\kappa_{fit} = 28.1 \text{ s}^{-1}$, which is very close to the photodetachment rates of the first few rotational levels.

In contrast, for the case of $\nu_{J'' \geq 2}$ the losses on the total relative ion population depends critically on the ion's initial rotational temperature and is no longer described by a simple exponential decay. This arises from the fact that the photodetachment cross sections for the levels $J'' = 0$ and $J'' = 1$ at this wavelength are zero. Therefore, the level $J'' \geq 2$ populations are quickly photodetached at the initial period of photodetachment interaction time $t \leq 1/\kappa_{pd, \nu_{J''=2}}$. After a certain time $t \geq 5/\kappa_{pd, \nu_{J''=2}}$ less than 1% of the initial ion population at higher levels remains trapped the photodetachment process. Therefore, the second decay after this time is only given by the repopulation of level $J'' = 2$ from $J'' = 1$ due to black body radiation, since ions pumped up into this levels are immediately detached. This can be seen in figure 4.7 due to the fact that at later times, the loss curves of the total population (green) and of the population in $J'' = 1$ (red) decrease nearly parallel to each other.

As showed in equation 4.26, the colder the ions rotational temperature, the higher the relative population in the lower rotational levels. For the case of 300 K, the levels $J'' = 0$ and $J'' = 1$ mount to 30,6 % of the total ion population. If

4 Rotational quenching of molecular anions by ultra cold atoms

black body radiation was not acting on the molecular ions, all these ions would remain trapped after the photodetachment process. Nevertheless, due to black body interaction, after 5 s photodetachment interaction time just about 20 % of the total ion population remain in the trap. This means that 65 % of the ions that populated $J'' = 0$ and $J'' = 1$ remained trapped and 35 % of them were pumped up into $J'' = 2$ during this time due to black body radiation.

In contrast, at 150 K the levels $J'' = 0$ and $J'' = 1$ constitute 52,4 % of the total ion population. After 5 seconds photodetachment interaction time merely 32 % of the total ion population remains trapped, which is 1,6 times more ions than for the case of 300 K. In this case, also about 65% of the ions that populated $J'' = 0$ and $J'' = 1$ remain trapped.

For 20 K, 99,9 % of the total ion population is in $J'' = 0$ and $J'' = 1$ and the interaction with black body radiation plays a big role. Since the repopulation from $J'' = 1$ to $J'' = 2$ is in the same order of magnitude of the photodetachment decay rate $\kappa_{\nu, J=2}$, one observes that the population at $J = 2$ first increases and tends to an equilibrium given by the black body repopulation and the photodetachment process. Similarly, the population in $J'' = 1$ increases due to the repopulation from $J'' = 0$ and the emission from $J'' = 2$ due to black body interaction. Therefore, one observes at the initial times a non exponential decrease of the total population. After 5 seconds photodetachment interaction time more than 80 % of the total ion population remain trapped.

In conclusion, the lower the rotational temperature of an ion sample, the more ions remain trapped after the photodetachment process after a given time. Similar considerations can be made for the cases with other photon energies (e.g. $\nu_{J'' \geq 1}$ and $\nu_{J'' \geq 3}$ in figure 4.3).

Moreover, by setting the wavelength of the laser above a certain photodetachment threshold, one can *select* which ion's state populations remain trapped after the photodetachment process. In the example, ions in $J'' = 0, 1$ remain trapped. In this way, state selective photodetachment allows the preparation of well defined rotational state distributions. This is of special interest in the case of $\nu_{J'' \geq 1}$, since in this case molecular anions being in the absolute ground state can be prepared.

4 Rotational quenching of molecular anions by ultra cold atoms

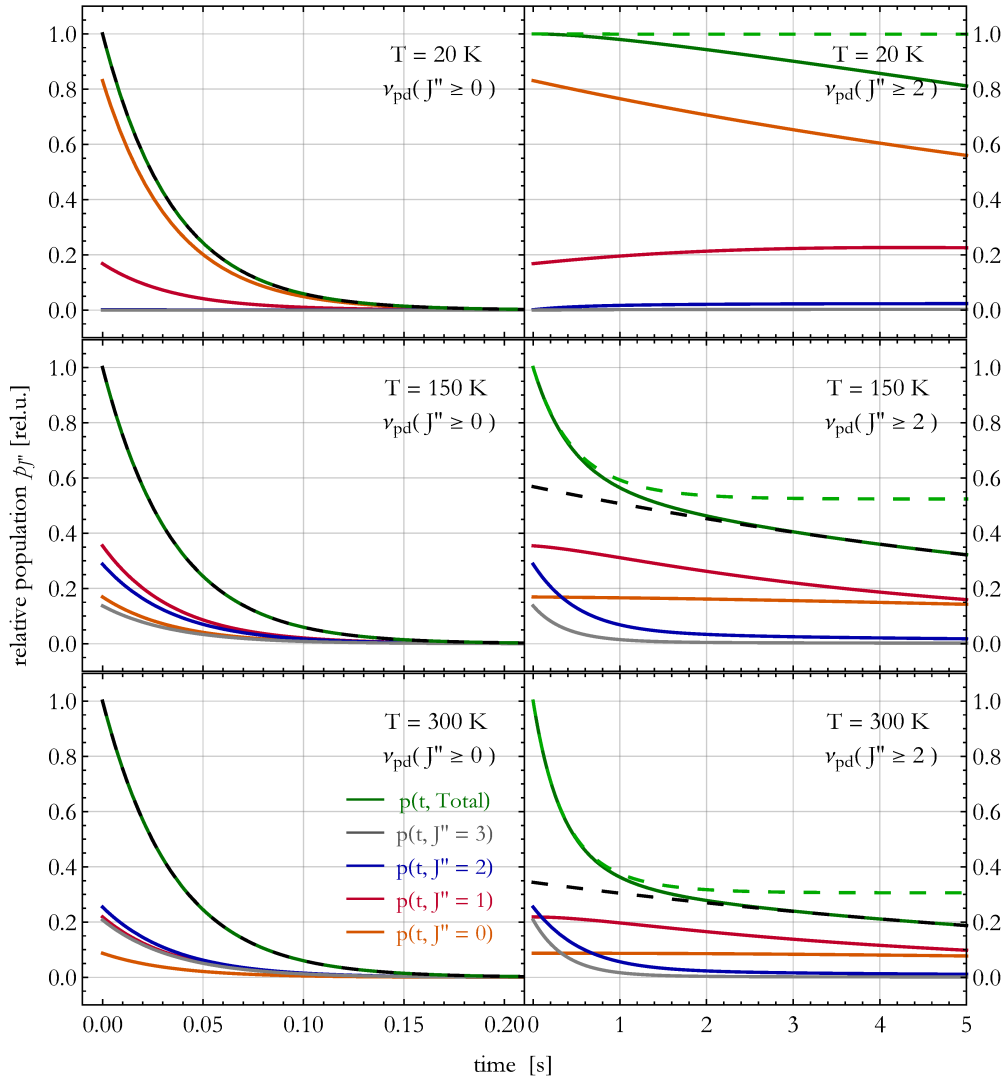


Figure 4.7: Time evolution of rotational level populations under the influence of different photodetachment laser wavelenghts and black body radiation. Thereby equation 4.34 is solved numerically for each level (different colors) and the total relative population is calculated with equation 4.35 (green curve). The individual decay rates used here are shown in figure 4.3 and figure 4.4. The green dashed curves show the case with photodetachment laser interaction only (no black body radiation). The black dashed curve corresponds to an exponential fit of the total relative population remaining for later time interactions. Its interpolation yields a good estimate of the initial population in $J = 0$ and $J = 1$.

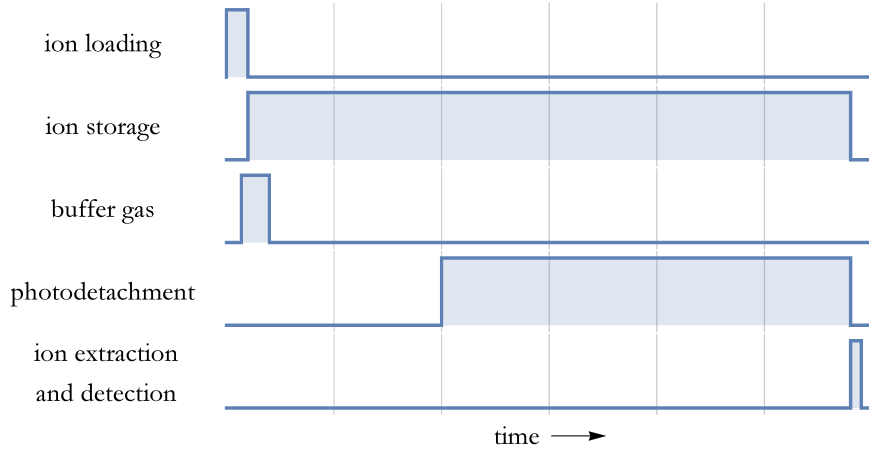
4.2.2 Room-temperature buffer gas: $\text{OH}^- + \text{He}$ 

Figure 4.8: Experimental cycle timings for photodetachment spectroscopy. During loading, the ions interact with a pulse of helium buffer gas at 295 K. The ions are stored in the trap for a fixed time set for all experimental runs. After pumping out the buffer gas, the photodetachment laser beam with frequency $\nu_{J''}$ is turned on for a given time period related to the end of the total ion storage time. Lastly, the remaining ions are extracted and counted. Times are not to scale.

In order to demonstrate rotational quenching of OH^- by ultra cold atoms (section 4.2.3), first we need to experimentally characterize the rotational state distribution of our trapped ion cloud *without* interaction with the ultra cold atoms. In this section we aim to describe such a characterization in our hybrid trap system. Here, we make use of the thermometry method called *state selective photodetachment* (section 4.2.1) for a trapped OH^- ion cloud that interacted only with He-buffer gas at room temperature. The sequence of such characterization experiment is performed as follows (figure 4.8).

The molecular ions are created and loaded into the octupole rf-trap as described in section 2.1.3. At the beginning of the trapping process, the ions interact with a He buffer gas pulse (≈ 250 ms) at room temperature (295 K). Once trapped, the ion cloud is cleaned out for O^- impurities, ensuring that only OH^- remains in the trap (section 2.1.4). Afterwards a photodetachment laser beam is shined into the clouds center (perpendicular to the trap) for a certain interaction time. The remaining ions are subsequently extracted and counted with a channeltron detector (section 2.1.4). This experimental run is repeated several times for different interaction times at a given laser frequency. The interaction time is shuffled after each experimental run in order to reduce systematic uncertainties. The laser power is monitored via a calibrated photo-diode for each experimental run.

4 Rotational quenching of molecular anions by ultra cold atoms

The experiment was performed for four different laser frequencies. They were chosen such that they are slightly below the first photodetachment threshold for a given J'' state (see figure 4.2). This neutralizes only the ions that are in a rotational state above the chosen threshold: ions in $J'' \geq 1$ are detached with $14\,724.4\text{ cm}^{-1}$, in $J'' \geq 2$ with $14\,658.1\text{ cm}^{-1}$ and in $J'' \geq 3$ with $14\,591.8\text{ cm}^{-1}$. Another laser frequency was chosen at $15\,104.2\text{ cm}^{-1}$ such that the laser neutralizes all ions. At this frequency, the photodetachment cross section does not depend on the internal temperature of the ion cloud [53].

The experimental data obtained is analyzed as follows. For correcting long time power fluctuations of the laser during this experiment we use the fact that the photodetachment decay rate is directly proportional to the photon flux (see equation 4.32). Consequently, for a fixed number of ions at $t = 0$, the number of surviving ions after the photodetachment process is the same whether they interacted with the laser at a certain power P for a certain time t or at a certain power P/k for a certain time $t * k$, with k being an arbitrary constant. Therefore the photodetachment interaction time t_{PD} can be rescaled as an effective interaction time with $t_{eff} = t_{PD} * P / P_{norm}$. Here t_{PD} is the time the laser was actually on, P is the measured laser power during this experimental run and P_{norm} is a normalizing laser power. Note that the normalizing term P_{norm} can be arbitrary chosen without changing the physics as long as it is in the same order of magnitude as P . We choose for this experiment $P_{norm} = P_{max}$, where P_{max} is the highest measured power in all runs.

The results are shown in figure 4.9. The points shown are obtained by binning the data for different effective time windows. The error bars are calculated as the statical error in each axis, i.e the standard deviation of the mean value divided by the square root of the number of experimental repetitions within one bin interval. The average detected number of ions, normalized to the average ion number detected at $t = 0$, is plotted as a function of the photodetachment interaction time for different laser frequencies (shown in different colors).

The solid lines represent a fit to the data using the solution for equation 4.35 with two free fit parameters: i) the initial rotational temperature of the ions T_0 (equation 4.26) and ii) the the column density (equation 4.32). The fit algorithms are programed to find the same fit parameters for all laser frequencies simultaneously.

In blue the data where all ions are subjected to photodetachment is shown. Here the laser frequency $\nu_{pd} = 15\,104.2\text{ cm}^{-1}$ is used, which is high enough for neutralizing ions in $J'' \geq 0$. As expected, the data points fit well to a simple exponential decay. This serves as a comparison between the decay rates caused by the photodetachment laser and the redistribution rates caused by the black body field. The orange curve shows the fit for $\nu_{pd} = 14\,724.4\text{ cm}^{-1}$. At the beginning of the photodetachment process, for short interaction times ($t \leq 300\text{ ms}$) a fast decay is observed. This decay is given by the neutralization of the ions being in $J'' \geq 1$ by the laser field. For later interaction times, almost all ions in $J'' \geq 1$ are already detached, meaning that the surviving ions are in $J'' = 0$. The slow decay for longer interaction times is given by the fact that

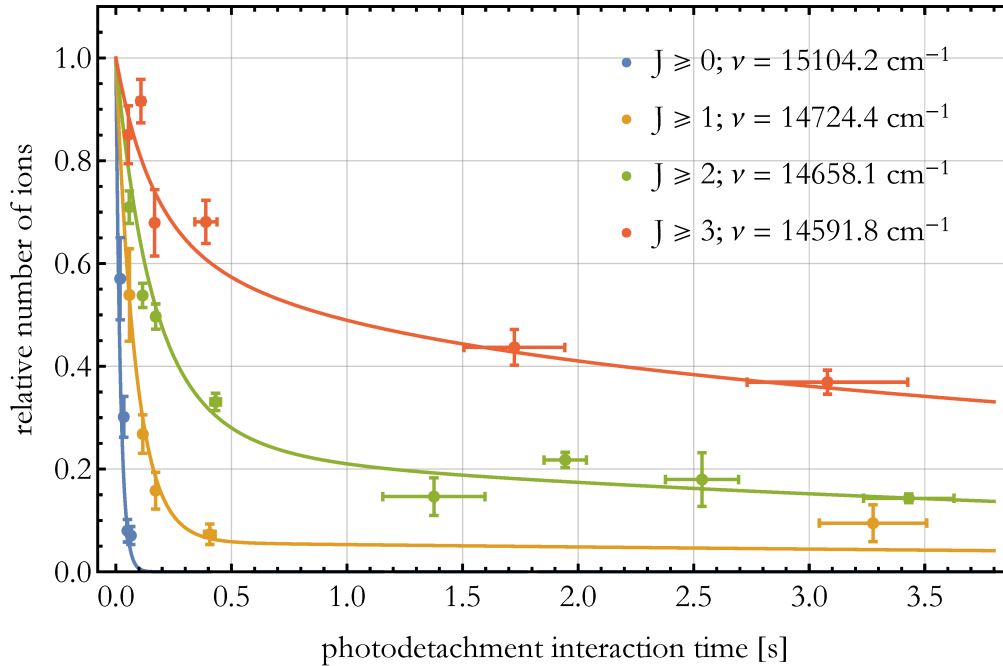


Figure 4.9: State selective photodetachment of OH^- . The ion cloud interacted with a He buffer gas at 295 K. Shown is the relative number of remaining ions in the trap as a function of the photodetachment interaction time for different PD laser frequencies. The points show the experimental data and the solid lines show a fit to the data using the solution for equation 4.35. The fit algorithm yielded a rotational temperature of 464 K and a column density of 18 cm^{-2} . The different colors code the laser frequencies used in the experiment.

ions in $J'' = 0$ are repopulated via black body radiation to $J'' = 1$ and are subsequently detached by the laser field. Similar observations are made for the lower frequencies $\nu_{pd} = 14\,658.1 \text{ cm}^{-1}$ (green curve) and $\nu_{pd} = 14\,591.8 \text{ cm}^{-1}$ (red curve). The fast decay for short interaction times is given by the neutralization of the ions in $J'' \geq 2$ and $J'' \geq 3$ respectively, and a slow decay for long interaction times given by the re-population due to black body field.

Since the ions interacted with a buffer gas at room temperature ($T = 295 \text{ K}$), it is expected that the rotational energy of the sample thermalizes with the buffer gas. Nevertheless, the fitted temperature $T_0 = 464 \text{ K}$ is much higher as this expected value. This can have several reasons:

- Incomplete thermalization with the buffer gas pulse.
- Rotational heating due to rf heating or background collisions.
- Temperature of black body field inside the trap higher as the room temperature due to heating of the rf wires.

- Errors in the determination of the photodetachment cross section energy dependence.

Regardless of the rotational temperature distribution found in this characterization, state selective neutralization of the molecular anion OH^- is demonstrated to be a reliable method for the measurement of the rotational distribution of our atom cloud. Furthermore, this measurement serves as a reference for comparing this results with the ones obtained after the interaction of the molecular anion OH^- with an ultra cold cloud of atoms.

A remarkable note is that state selective photodetachment allows the preparation of internal absolute ground state molecular anions, even if the initial rotational temperature of the ion cloud is at room temperature.

4.2.3 Ultra cold buffer gas: $\text{OH}^- + \text{Rb}$

In this section, rotational quenching of molecular anions by ultra cold atoms is experimentally demonstrated in our hybrid trap system. For this aim, we apply again the thermometry method *state selective photodetachment* (section 4.2.1) for a trapped OH^- ion cloud that interacted in a first stage with a He-buffer gas at room temperature (section 4.2.2) and afterwards with the ultra-cold cloud of Rb atoms. The sequence of this experiment is schematically shown in figure 4.10 and is performed as follows.

The preparation and trapping procedure of the OH^- cloud into the rf octupole trap is similar as in section 4.2.1. After loading, the ions are stored for a few seconds in the radio frequency trap in order to pump out the remaining He buffer gas. In order to detach O^- impurities from the ion trap, the atoms cooling laser is on during this time. Thereafter, when the main chamber reaches a pressure of $\approx 10^{-8}$ mbar, the atoms are loaded into the darkSPOT by switching on the re-pumper laser (section 2.2.3). In this way the atom and anion clouds are overlapped for a given interaction time. In order to monitor the optical density of the atom cloud after each experimental run, a non-resonant absorption imaging of the atom cloud is made (section 2.2.3). This imaging procedure is made immediately after the set atom-ion interaction time and lasts about one second. Subsequently, state selective photodetachment is performed by turning on the photodetachment laser at a given frequency. The surviving ions are extracted and detected. The data obtained is analyzed as already explained in section 4.2.1.

In figure 4.11, the relative number of ions is plotted as a function of the photodetachment interaction time. In this particular case, the photodetachment procedure was done at a laser frequency of $\nu_{pd} = 14\,658.1 \text{ cm}^{-1}$ after 4 different interaction times of the atom-ion clouds. This laser frequency neutralizes only ions being in $J'' \geq 2$. The points show the measured data and the solid lines the fitted curves to the experimental data. The fitting procedure was done in all cases with the ions initial rotational temperature (equation 4.26) and the column density (equation 4.32) as free fitting parameters.

The photodetachment procedure with 0 seconds atom-ion interaction time was

4 Rotational quenching of molecular anions by ultra cold atoms

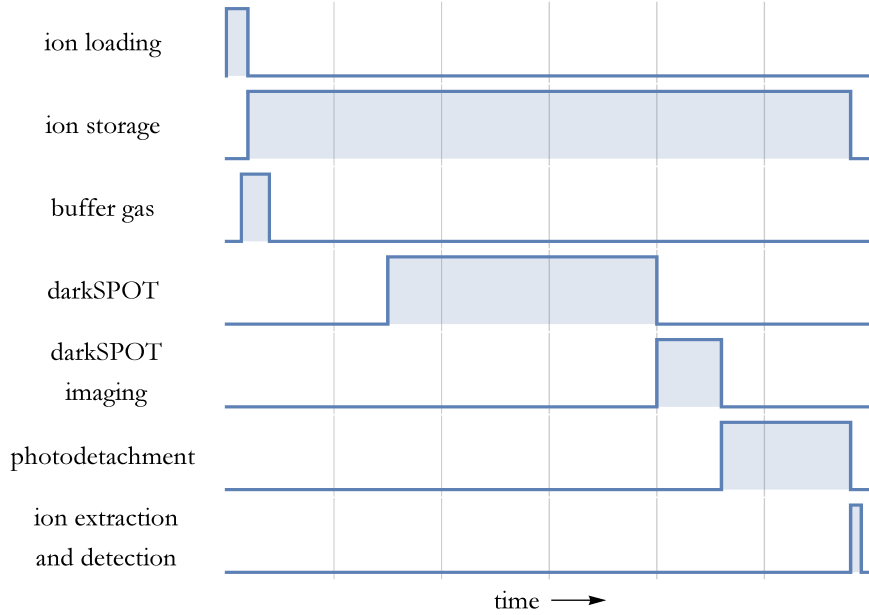


Figure 4.10: Experimental cycle timings for rotational quenching.

During loading, the ions interact with a pulse of helium buffer gas at 295 K. The ions are stored in the trap for a fixed time set for all experimental runs. After pumping out the buffer gas, rubidium atoms are loaded in the darkSPOT. After a certain interaction time, a detuned-absorption image of the atom cloud is made. Thereafter the photodetachment laser beam with frequency $\nu_{j''}$ is turned on for a given time period related to the end of the total ion storage time. Lastly, the remaining ions are extracted and counted. Times are not to scale.

shown in previous section (see figure 4.9) and serves as a control measurement. In figure 4.11 one clearly observes that, the longer the ions interacted with the ultra cold atoms, the higher is the relative number of ions that remain trapped. As discussed in section 4.2.1 (see right graphs, green curves in figure 4.7), this effect can only be explained by rotational cooling: the lower the rotational temperature of the molecular anion sample at the beginning of the photodetachment process, the more ions remain trapped. Furthermore, the longer the atom-ion interaction time, the more collisions between them and consequently the lower the rotational temperature due to rotational quenching of the molecular anions by the ultra cold atom cloud. In total, one observes a decrease of about 72% in the rotational temperature after 5 seconds atom-ion interaction time. The main limitation in our system for reaching lower temperatures are the ion losses mainly caused by associative detachment (section 3.1.1).

In conclusion, we observed a clear effect on the rotational quenching of the molecular anions via inelastic collisions with the ultracold Rb atoms. Further-

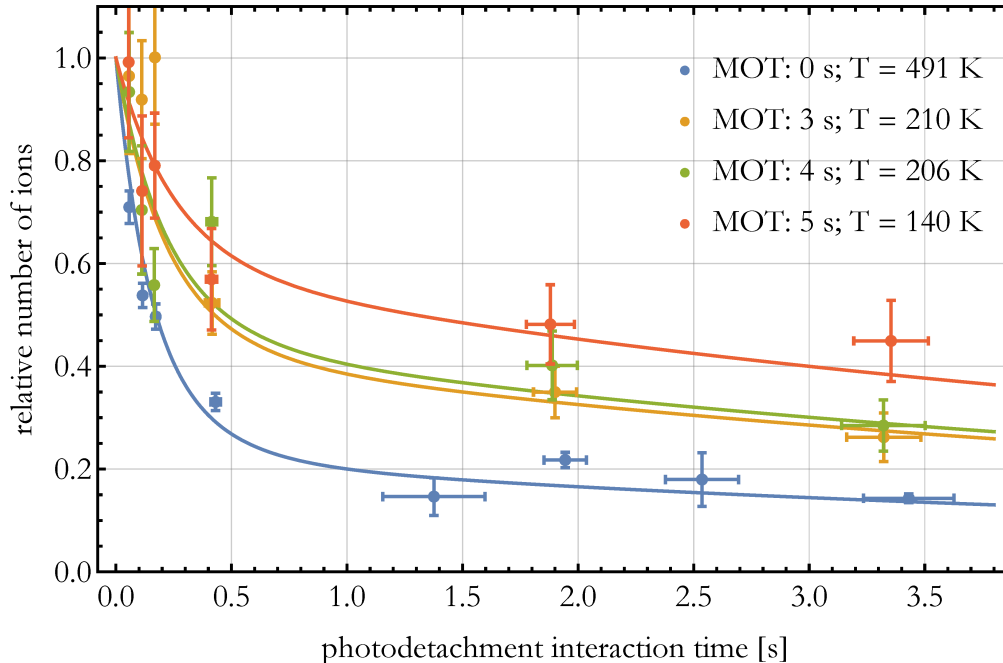


Figure 4.11: Experimental demonstration of rotational quenching in OH^- by ultra cold Rb atoms. The observed relative number of ions is plotted as a function of the photodetachment interaction time for different atom-ion interaction times (different colors). The photodetachment laser frequency chosen is $\nu_{pd} = 14\,658.1\text{ cm}^{-1}$, which neutralizes ions in $J'' \geq 2$ (see right green curves on figure 4.7). The longer the ions interacted with the Rb cloud, the higher is the observed fraction of surviving ions after photodetachment. This effect can only be explained by rotational quenching of the OH^- sample by collisions with Rb, as discussed in section 4.2.1.

more, in our hybrid trap it is possible to combine the two methods presented in this chapter (state selective photodetachment and rotational quenching) for the preparation of different rotational state distributions of the molecular anions. For instance, by choosing the laser frequency at $\nu_{J \geq 1}$, internal absolute ground state molecular anions can be prepared. Since these ions were also subject to sympathetic cooling of their external degrees of freedom as shown in chapter 3, the molecular anions prepared by this means are not only in their absolute electronic ro-vibrational ground state, but are also transitionally cold. This state preparation schemes can help for instance to investigate whether the chemical reaction paths of the system $\text{OH}^- + \text{Rb}$ depend on the rotational state of the molecular anion. An experiment in this direction is currently being prepared. Our results have direct implications for the prospects on achieving lower temperatures of anionic clouds, as will be discussed in the outlook of this dissertation.

5 Conclusion and Outlook

5.1 Conclusion

During the course of this doctoral work a novel hybrid atom-ion trap has been developed for the investigation of atom-ion collision dynamics. The HAITrap combines an octupole radio frequency trap for ions and a dark-spontaneous force optical trap (darkSPOT) for rubidium atoms. The overlap of the OH^- and Rb clouds was successfully implemented as the atom-ion system to be studied in the HAITrap. It was observed that collisions of trapped ions with ultracold atoms sympathetically cooled both the translational as well as the rotational degrees of freedom of OH^- .

Several key steps were needed to achieve sympathetic cooling of the $\text{OH}^- + \text{Rb}$ system. The first one was to control the system's chemical reactions that lead to unavoidable losses of the stored ions. It was shown, that it is possible to increase the number of elastic collisions by increasing the dark state fraction of the internal state distribution of the atom cloud in the darkSPOT.

Furthermore, a theoretical framework for the elastic atom-ion collision dynamics inside the HAITrap was presented. The outcomes of this model allowed the development of a clear experimental strategy to avoid radio frequency induced collisional heating, not only in the HAITrap but also for arbitrary trap geometry configurations. Based on these outcomes, further key components in the experiment were i) the use of a multipole ion trap and ii) locating the ultracold buffer gas inside the ion trap, such that atom-ion collisions take place only near the rf-field-free region of the ion trap. In this way, the high mass ratio of the system ($m_a/m_i = 5$) no longer acts as a limitation for sympathetic cooling, as was believed a few years ago. This also opens the possibility not only to cool down the ions but also to further investigate exotic (non-thermal) energy distributions in rf traps.

In the case of kinetic sympathetic cooling, two different thermometry methods for estimating the final ions' temperature within some constraints for each method were used. Since OH^- is not directly detectable via optical means, the thermometry methods used in this work are destructive and are based on the intrinsic ion dynamics inside a trap.

The first thermometry method used in the experiment was electron photodetachment as a tool for making indirect tomographic images of the ion cloud. From these images the ion cloud spatial distribution was obtained. Its standard deviation correlates with the square root of the ions temperature in axial trapping direction. This fact was qualitatively demonstrated by numerical simulations. 1D tomographic images were taken after the ions interacted with two

5 Conclusion and Outlook

different buffer gases: helium at 295 K and localized rubidium at $\approx 300 \mu\text{K}$. It was observed that the standard deviation of the ions spatial distribution was smaller after the interaction with rubidium as compared to that with helium. Assuming a harmonic trapping potential and that the ions thermalize with the helium buffer gas at room temperature, the comparison of both spatial distributions provides a rough estimate of the ions temperature to be $72 \pm 26 \text{ K}$ after interaction with Rb. However, these results have to be interpreted very carefully, because the methods show big statistical uncertainties as most of the ions are lost during the cooling process due to reactive collisions. Only a low number of ions are detected after these interactions. In spite of this, photodetachment tomography provided a clear evidence on sympathetic cooling.

The second thermometry method to prove kinetic sympathetic cooling was based on measuring the distribution of the ion's time of flight (ToF) after extraction from the ion trap to the detector. Based on numerical simulations and a one dimensional analysis for the ion extraction dynamics from the trap, it was found that the width of the ToF distribution correlates with the square root of the ions temperature in the trap at the moment of extraction. Although this correlation remains the same regardless of the potential landscape at the moment of extraction, it is of advantage to choose an extraction potential landscape that results on symmetrical ToF distributions. From an experimental point of view, a key ingredient for applying this method was to use a single ion detection scheme with high time resolution and to make sure that the ion detector is not saturated. Since every detected ion contributed to the final ToF distribution, this method was found to be more efficient in providing reliable statistics than photodetachment tomography. It allowed systematic measurements of the ions' ToF distribution for different configurations. It was systematically observed that higher atom cloud density and longer interaction time of ions with the atom cloud, the narrower the ToF width was. This narrowing was attributed to sympathetic cooling of the ions. For a rough estimation of the final temperature of the ions, some assumptions had to be made. First, the trapping potential in axial direction is harmonic. Second, the ToF width after the ions interacted with helium at room temperature provides a measure for the ToF distribution of ions at 300 K. In this way, the lowest temperature observed was estimated to be in the order of $35 \pm 5 \text{ K}$. Since this model is based on a one-dimensional extraction scheme, it demands a careful interpretation. However, the results obtained already provide an intuitively reliable approximation of the cooling effect observed.

Despite the constraints of both thermometry methods, the results indicate that the temperatures achieved in the system are comparable with those of cryogenic traps.

An additional observation by means of ToF thermometry was the emergence of non-thermal ion distributions in the trap. From numerical simulations it was observed that a thermal distribution, which has a Gaussian shape in phase space, is "imaged" onto the ToF distribution also with a Gaussian shape. This is a consequence of a special chosen extraction potential landscape, in which the

5 Conclusion and Outlook

ions ToF depends linearly on both the trapped ions axial position as well as the ions axial velocity. It was observed experimentally that this is true for ions that interacted with helium at room temperature. However, deviations from a Gaussian ToF distribution were measured after the ions interacted with the Rubidium buffer gas. In the last case, the resulting ToF distributions are better described by a Tsallis probability function. These deviations can be attributed to the emergence of non-thermal distributions, which are predicted by the theoretical model.

In the HAITrap it was possible to observe rotational quenching of the molecular anion OH^- via collisions with the ultracold rubidium buffer gas. For this aim, a model for the rotational structure of OH^- , its interaction with photons from a laser field and from the surrounding black body field was introduced. The rotational thermometry method applied in the experiment was based on this model. It takes advantage of the fact that the OH^- photodetachment cross section σ_{PD} depends on the photon energy as well as on the rotational state of the ion. Thereby σ_{PD} is mainly characterized by an energy threshold behavior $E_{\gamma,PD}$: when the photon's energy is below this threshold, it is not able to detach the anion's electron ($\sigma_{PD} = 0$), whereas for a photon's energy above this threshold the cross section scales with the photon energy as $\sigma_{PD} \propto (E_{\gamma}^{\rho})$. Furthermore, the higher the ions rotational level is, the less photon energy is needed to detach the electron from the anion. Thus, by choosing laser frequencies slightly below the energy thresholds for the first rotational states, it was possible to select the rotational levels that allow photodetachment. Assuming a Boltzmann distribution for the anions' rotational state population, the lower the ions' rotational temperature, the higher is the fraction of ions that populate the lower rotational levels. Therefore, after the photodetachment process at a laser frequency below an energy threshold, the fraction of ions remaining in the trap correlates with the rotational temperature of the ions.

State selective photodetachment was applied in the experiment for two different buffer gas configurations, similar to the one adopted for kinetic sympathetic cooling. For the case of helium at room temperature as a buffer gas, we performed photodetachment for four different laser frequencies. These were chosen to include the first four rotational levels of OH^- . As expected from the photodetachment model, a fast decay for short ion-laser interaction times and a slow decay for long ion-laser interaction times was observed. The fast decay was attributed to the neutralization of the anions in the rotational states with non-zero photodetachment cross section at the corresponding laser frequency. The slow decay was attributed to the neutralization of the anions that are being repopulated via black body radiation from lower to higher rotational states, which consequently are again accessible to the photodetachment laser. The fit to the obtained experimental data using the coupled differential equations model provided a value for the ions temperature of 464 K, which is unfortunately beyond the expected room temperature value. The reasons for this discrepancy requires further investigation but can be mainly attributed to an incomplete thermalization of the rotational states with the helium buffer gas pulse. An interesting

5 Conclusion and Outlook

observation from rotational state selective photodetachment is that it allows the preparation of ro-vibrational ground state molecular anions, regardless of the initial rotational temperature of the ion cloud.

For the case of rubidium as an ultra-cold buffer gas, photodetachment for one laser frequency as a proof of principle was performed. The chosen laser frequency neutralized ions present in the rotational states $J'' \geq 2$. It was observed that the longer the ions interacted with the Rb cloud, the higher is the fraction of ions remaining in the trap after photodetachment. This clear trend can only be explained by rotational quenching of the OH^- sample by collisions with Rb. Specifically, 5 seconds atom-ion interaction time led to a decrease of the rotational temperature of about 72%.

As an overall assessment, it can be concluded that i) the reported findings in the experiment validate the theoretical predictions regarding the prospects of sympathetic cooling for an atom-ion system with a high mass ratio as well as the emergence of non-thermal distributions; ii) for the first time direct experimental proof of sympathetic cooling of molecular anions in their external and internal degrees of freedom simultaneously was presented; iii) the combination of rotational state selective photodetachment and sympathetic cooling allowed the preparation of kinetically cold samples of OH^- in their ro-vibrational ground state.

These findings could be beneficial for many research areas, and it is hoped that they will further motivate several other experimental groups to pursue a similar approach to achieve cooling of anionic species.

5.2 Outlook

The prospects of the experimental as well as the theoretical results are very vast. Therefore, in this section the outlook of this dissertation shall be discussed in three different areas.

Improvements on the theoretical model for elastic collision dynamics inside radio frequency traps.

The theoretical model provided steady state energy distributions for a single ion. Nevertheless, dynamical understanding of the cooling process is required, describing how the ion energy distribution evolves in time from a thermal to its final steady state (non-thermal) distribution. Furthermore, the model should be extended to include unavoidable deconfinement effects in the experiment. For instance, static axial confinement of the ions leads to radial deconfinement, which could lead to an enhanced rf-induced collisional heating.

As inferred from the observations, the ions attain temperatures where Coulomb interaction between the ions cannot be neglected anymore. The theoretical model should therefore be extended to include Coulomb interaction as a heating effect in the cooling process. Such effects were already discussed for Paul trap configurations [13], but it is still an open question which cooling parameters would be influenced by Coulomb interaction of ions inside higher order rf traps.

Improvements on the current HAITrap's experimental setup.

In order to prevent the saturation of the channeltron ion detector in the setup, the number of ions detected per experimental cycle was limited. One of the most important improvements in the HAITrap's experimental setup would be therefore to install a more efficient ion detection scheme.

The simplest solution to fix this problem would be to replace the channeltron for a micro-channel plate (MCP) with a high time resolution for single ion counting. For this, an improved wavelet counting algorithm would be required, since in such a detector the simultaneous arrival of two or more ions would produce a higher peak signal rather than separated peaks.

A more elegant solution is offered by a technique called spatial map imaging developed by the group of Prof. R. Wester [131]. An ion imaging spectrometer would have to be developed that fits around the rf ion trap, such that the ions are extracted in radial direction rather than in axial direction. The extracted ions are projected onto a position sensitive detector and the fluorescence of the ion cloud can be imaged using a CCD camera. This would allow for measurements of the density distribution of the trapped ions in a single-cycle experiment. Using this approach, the dynamics of the cooling process can be investigated in more detail, and cooling of the trapped ions can be optimized.

Future perspectives.

The main limitation for sympathetic cooling in the $\text{OH}^- + \text{Rb}$ system was the loss of ions due to chemical reactions. Nevertheless, the disadvantage for one field can be an advantage for another. Here, this is the case in the field of cold chemistry. Open chemical reaction channels in this system were studied already in an early stage of the experiment [15]. Currently, an improved experiment is being performed in the HAITrap to carefully measure the reaction collision cross sections of $\text{OH}^- + \text{Rb}$ as a function of the internal state distribution of the atoms. This will provide conclusive results and would test the models available in the literature for the computation of potential energy surfaces of this system [105, 106].

For the future prospects of sympathetic cooling, in order to reach lower temperatures of anionic clouds one would have to choose an atom-ion system that does not show open reaction channels. For OH^- this would be possible by using a potassium MOT or any alkali and alkaline earth atoms (except Cs) in a dipole trap [132]. A dipole trap for rubidium atoms is currently being set up [62]. However, for any other neutral species this would require a whole new laser system for the neutral particle chosen.

For a further use of rubidium as an ultra-cold buffer gas, there are several interesting anionic candidates for sympathetic cooling. The first choice would be the use of hydrated water clusters $\text{OH}^- (\text{H}_2\text{O})_n$ with $n = 1 - 2$. Such molecular anions can be produced efficiently in the ion source. Furthermore, their electron affinities are 3 eV and 3.8 eV respectively, making associative detachment less probable to occur. However, it is still a possibility that the additional water molecules may cluster to the RbOH product. Moreover, this anionic molecule would be of great interest from the chemistry point of view since these possible reaction channels are unknown and could be studied experimentally in the HAITrap as a function of the size of the anionic clusters. Additionally, the study of the internal structure of such molecules is of huge importance since it is directly linked to the structure of water itself. A review article cited more than 40 distinct models for the description of water molecules, indicating that no single model is able to explain all of its properties [133, 134]. For the study of the vibrational structure of such clusters, Raman-terahertz spectroscopy could be applied as a method for probing the frequency and strength of the cluster motions [135, 136]. This would be of special interest if the ionic water clusters are prepared as a cold sample.

A further anion of interest would be the anionic molecule C_2^- . These kind of ions can also be created in the ion source by choosing the right seed gas. Its electron affinity is 3.8 eV, thus it would not interact with the cooling lasers of the rubidium MOT, and would have no reactive channels open with Rb. Consequently, it would be a perfect candidate for studying the experimental limits of sympathetic cooling in the HAITrap. This anion is not only relevant for its abundance in the interstellar space, but it is one of the candidates for the not yet achieved laser cooling of negative particles [35]. Sympathetic cooling of this anion could offer the required pre-cooling schemes for the application of

5 Conclusion and Outlook

laser cooling in negative ion systems [37].

The use of such anions will allow the extension of the information obtained on collisional cooling to systems with more internal degrees of freedom, to apply *forced sympathetic cooling* as proposed in [24], and to explore the significance of inelastic collisions for other ions. Efficient cooling of only one anionic species will allow for sympathetically cool any other negatively charged species such as anions, electrons or antiprotons. In the distant future it would also be interesting to experimentally investigate a proposed laser cooling scheme for OH^- [36].

A Bibliography

- [1] John Weiner, Vanderlei S. Bagnato, Sergio Zilio, and Paul S. Julienne. Experiments and theory in cold and ultracold collisions. *Rev. Mod. Phys.*, 71, 1999. URL <https://link.aps.org/doi/10.1103/RevModPhys.71.1>.
- [2] Lincoln D Carr, David DeMille, Roman V Krems, and Jun Ye. Cold and ultracold molecules: science, technology and applications. *New Journal of Physics*, 11(5):055049, 2009. URL <http://stacks.iop.org/1367-2630/11/i=5/a=055049>.
- [3] Bernhard Roth and Stephan Schiller. Sympathetically cooled molecular ions: from principles to first applications. arXiv e-print 0812.1154, Institut fur Experimentalphysik Dusseldorf, 2008. URL <http://arxiv.org/abs/0812.1154>.
- [4] Stefan Willitsch, Martin T. Bell, Alexander D. Gingell, and Timothy P. Softley. Chemical applications of laser- and sympathetically-cooled ions in ion traps. *Phys. Chem. Chem. Phys.*, 10, 2008. URL <http://dx.doi.org/10.1039/B813408C>.
- [5] W. Ketterle, D. S. Durfee, and D. M. Stamper-Kurn. Making, probing and understanding bose-einstein condensates. *ArXiv e-prints*, 1999. URL <https://arxiv.org/abs/cond-mat/9904034>.
- [6] Harold J Metcalf and Peter Straten. *Laser cooling and trapping of neutral atoms*. Wiley Online Library, 2007.
- [7] Dieter Gerlich. Ion-neutral collisions in a 22-pole trap at very low energies. *Physica Scripta*, page 256, 1995. URL <http://stacks.iop.org/1402-4896/1995/i=T59/a=035>.
- [8] Peter F Sta anum, Klaus Høj bjerre, Peter S Skyt, Anders K Hansen, and Michael Drewsen. Rotational laser cooling of vibrationally and translationally cold molecular ions. *Nature Physics*, 6(4):271–274, 2010. URL <https://www.nature.com/articles/nphys1604>.
- [9] E. S. Shuman, J. F. Barry, and D. DeMille. Laser cooling of a diatomic molecule. *Nature*, 467(7317):820–823, 10 2010. URL <http://dx.doi.org/10.1038/nature09443>.
- [10] Roland Wester. Radiofrequency multipole traps: tools for spectroscopy and dynamics of cold molecular ions. *Journal of Physics B: Atomic, Molecular and Optical Physics*, 42(15):154001, 2009. URL <http://iopscience.iop.org/article/10.1088/0953-4075/42/15/154001>.

A Bibliography

- [11] Oleg P. Makarov, R. Côté, H. Michels, and W. W. Smith. Radiative charge-transfer lifetime of the excited state of $(\text{NaCa})^+$. *Phys. Rev. A*, 67, 2003. URL <http://link.aps.org/doi/10.1103/PhysRevA.67.042705>.
- [12] Eric R. Hudson. Method for producing ultracold molecular ions. *Phys. Rev. A*, 79, 2009. URL <https://doi.org/10.1103/PhysRevA.79.032716>.
- [13] Steven J. Schowalter, Alexander J. Dunning, Kuang Chen, Prateek Puri, Christian Schneider, and Eric R. Hudson. Blue-sky bifurcation of ion energies and the limits of neutral-gas sympathetic cooling of trapped ions. *Nature Communications*, 7:12448, Nov 2016. URL <https://www.nature.com/articles/ncomms12448>.
- [14] Oskar Asvany and Stephan Schlemmer. Numerical simulations of kinetic ion temperature in a cryogenic linear multipole trap. *International Journal of Mass Spectrometry*, 2009. URL <http://www.sciencedirect.com/science/article/pii/S1387380608004338>.
- [15] J. Deiglmayr, A. Göritz, T. Best, M. Weidemüller, and R. Wester. Reactive collisions of trapped anions with ultracold atoms. *Phys. Rev. A*, 86:043438, Oct 2012. doi: 10.1103/PhysRevA.86.043438. URL <http://link.aps.org/doi/10.1103/PhysRevA.86.043438>.
- [16] Stefan Willitsch, Martin T. Bell, Alexander D. Gingell, Simon R. Procter, and Timothy P. Softley. Cold reactive collisions between laser-cooled ions and velocity-selected neutral molecules. *Phys. Rev. Lett.*, 100, 2008. URL <http://link.aps.org/doi/10.1103/PhysRevLett.100.043203>.
- [17] A. Härter and J. Hecker Denschlag. Cold atom-ion experiments in hybrid traps. *ArXiv e-prints*, 2013. URL <http://arxiv.org/abs/1309.5799>.
- [18] Stefan Willitsch. Ion-atom hybrid systems. *ArXiv e-prints*, 2014. URL <http://arxiv.org/abs/1401.1699>.
- [19] Michal Tomza, Krzysztof Jachymski, Rene Gerritsma, Antonio Negretti, Tommaso Calarco, Zbigniew Idziaszek, and Paul S. Julienne. Cold hybrid ion-atom systems, 2017. URL <https://arxiv.org/abs/1708.07832>.
- [20] Ralph G. DeVoe. Power-law distributions for a trapped ion interacting with a classical buffer gas. *Phys. Rev. Lett.*, 102, 2009. URL <http://link.aps.org/doi/10.1103/PhysRevLett.102.063001>.
- [21] Christoph Zipkes, Lothar Ratschbacher, Carlo Sias, and Michael Köhl. Kinetics of a single trapped ion in an ultracold buffer gas. *New Journal of Physics*, 13, 2011. URL <http://stacks.iop.org/1367-2630/13/i=5/a=053020>.
- [22] Marko Cetina, Andrew T. Grier, and Vladan Vuletić. Micromotion-induced limit to atom-ion sympathetic cooling in paul traps. *Phys.*

A Bibliography

- Rev. Lett.*, 109, 2012. URL <http://link.aps.org/doi/10.1103/PhysRevLett.109.253201>.
- [23] Kuang Chen, Scott T. Sullivan, and Eric R. Hudson. Neutral gas sympathetic cooling of an ion in a paul trap. *Phys. Rev. Lett.*, 112, 2014. URL <http://link.aps.org/doi/10.1103/PhysRevLett.112.143009>.
- [24] Bastian Höltkemeier, Pascal Weckesser, Henry López-Carrera, and Matthias Weidemüller. Buffer-gas cooling of a single ion in a multi-pole radio frequency trap beyond the critical mass ratio. *Phys. Rev. Lett.*, 116:233003, Jun 2016. doi: 10.1103/PhysRevLett.116.233003. URL <http://link.aps.org/doi/10.1103/PhysRevLett.116.233003>.
- [25] Bastian Höltkemeier, Pascal Weckesser, Henry López-Carrera, and Matthias Weidemüller. Dynamics of a single trapped ion immersed in a buffer gas. *Phys. Rev. A*, 94:062703, Dec 2016. doi: 10.1103/PhysRevA.94.062703. URL <https://link.aps.org/doi/10.1103/PhysRevA.94.062703>.
- [26] Winthrop W. Smith, Oleg P. Makarov, and Jian Lin. Cold ion neutral collisions in a hybrid trap. *Journal of Modern Optics*, 52, 2005. URL <https://doi.org/10.1080/09500340500275850>.
- [27] Christoph Zipkes, Stefan Palzer, Carlo Sias, and Michael Kohl. A trapped single ion inside a bose-einstein condensate. *Nature*, 464, 2010. URL <http://dx.doi.org/10.1038/nature08865>.
- [28] I. Sivarajah, D. S. Goodman, J. E. Wells, F. A. Narducci, and W. W. Smith. Evidence of sympathetic cooling of Na^+ ions by a Na magneto-optical trap in a hybrid trap. *Phys. Rev. A*, 86:063419, Dec 2012. doi: 10.1103/PhysRevA.86.063419. URL <https://link.aps.org/doi/10.1103/PhysRevA.86.063419>.
- [29] K. Ravi, . Lee, A. Sharma, G. Werth, and S.A. Rangwala. Cooling and stabilization by collisions in a mixed ion-atom system. *Nat Commun*, 3, 2012. URL <http://dx.doi.org/10.1038/ncomms2131>.
- [30] S. Dutta, R. Sawant, and S. A. Rangwala. Collisional cooling of light ions by cotrapped heavy atoms. *Phys. Rev. Lett.*, 118:113401, Mar 2017. doi: 10.1103/PhysRevLett.118.113401. URL <https://link.aps.org/doi/10.1103/PhysRevLett.118.113401>.
- [31] Shinsuke Haze, Mizuki Sasakawa, Ryoichi Saito, Ryosuke Nakai, and Takashi Mukaiyama. Cooling dynamics of a single trapped ion via elastic collisions with small-mass atoms. *Phys. Rev. Lett.*, 120, 2018. URL <https://link.aps.org/doi/10.1103/PhysRevLett.120.043401>.
- [32] Ludovic Biennier, Sophie Carles, Daniel Cordier, Jean-Claude Guillemin, Sebastien D. Le Picard, and Alexandre Faure. Low temperature reaction

A Bibliography

- kinetics of $\text{cn}^- + \text{hc3n}$ and implications for the growth of anions in titan's atmosphere. *Icarus*, 227, 2014. URL <http://www.sciencedirect.com/science/article/pii/S0019103513003825>.
- [33] Thomas J. Millar, Catherine Walsh, and Thomas A. Field. Negative ions in space. *Chemical Reviews*, 117(3), 2017. URL <https://pubs.acs.org/doi/abs/10.1021/acs.chemrev.6b00480>.
- [34] Alban Kellerbauer and Jochen Walz. A novel cooling scheme for antiprotons. *New Journal of Physics*, 8, 2006. URL <http://stacks.iop.org/1367-2630/8/i=3/a=045>.
- [35] Pauline Yzombard, Mehdi Hamamda, Sebastian Gerber, Michael Doser, and Daniel Comparat. Laser cooling of molecular anions. *Phys. Rev. Lett.*, 114, 2015. URL <https://link.aps.org/doi/10.1103/PhysRevLett.114.213001>.
- [36] Ming-jie Wan, Duo-hui Huang, You Yu, and Yun-guang Zhang. Laser cooling of the oh^- molecular anion in a theoretical investigation. *Phys. Chem. Chem. Phys.*, 19, 2017. URL <http://dx.doi.org/10.1039/C7CP04393G>.
- [37] G. Cerchiari, A. Kellerbauer, M. S. Safronova, U. I. Safronova, and P. Yzombard. Ultracold anions for high-precision antihydrogen experiments. *Phys. Rev. Lett.*, 120:133205, Mar 2018. doi: 10.1103/PhysRevLett.120.133205. URL <https://link.aps.org/doi/10.1103/PhysRevLett.120.133205>.
- [38] C. Meyer, A. Becker, K. Blaum, C. Breitenfeldt, S. George, J. Göck, M. Grieser, F. Grussie, E. A. Guerin, R. von Hahn, P. Herwig, C. Krantz, H. Kreckel, J. Lion, S. Lohmann, P. M. Mishra, O. Novotný, A. P. O'Connor, R. Repnow, S. Saurabh, D. Schwalm, L. Schweikhard, K. Spruck, S. Sunil Kumar, S. Vogel, and A. Wolf. Radiative rotational lifetimes and state-resolved relative detachment cross sections from photodetachment thermometry of molecular anions in a cryogenic storage ring. *Phys. Rev. Lett.*, 119, 2017. URL <https://link.aps.org/doi/10.1103/PhysRevLett.119.023202>.
- [39] H. T. Schmidt, G. Eklund, K. C. Chartkunchand, E. K. Anderson, M. Kamińska, N. de Ruelle, R. D. Thomas, M. K. Kristiansson, M. Gatchell, P. Reinhed, S. Rosén, A. Simonsson, A. Källberg, P. Löfgren, S. Mannervik, H. Zettergren, and H. Cederquist. Rotationally cold oh^- ions in the cryogenic electrostatic ion-beam storage ring desiree. *Phys. Rev. Lett.*, 119, 2017. URL <https://link.aps.org/doi/10.1103/PhysRevLett.119.073001>.
- [40] G. Gabrielse, A. Khabbaz, D. S. Hall, C. Heimann, H. Kalinowsky, and W. Jhe. Precision mass spectroscopy of the antiproton and proton using simultaneously trapped particles. *Phys. Rev. Lett.*, 82, 1999. URL <https://link.aps.org/doi/10.1103/PhysRevLett.82.3198>.

A Bibliography

- [41] Jean-Luc Le Garrec, B. R. Rowe, J. L. Queffelec, J. B. A. Mitchell, and David C. Clary. Temperature dependence of the rate constant for the $\text{cl} + \text{ch}_3\text{br}$ reaction down to 23 k. *The Journal of Chemical Physics*, 107, 1997. URL <https://doi.org/10.1063/1.474431>.
- [42] Daniel Hauser, Seunghyun Lee, Fabio Carelli, Steffen Spieler, Olga Lakhmanskaya, Eric S. Endres, Sunil S. Kumar, Franco Gianturco, and Roland Wester. Rotational state-changing cold collisions of hydroxyl ions with helium. *Nat Phys*, 11, 2015. URL <http://dx.doi.org/10.1038/nphys3326>.
- [43] Anna T. Göritz. Wechselwirkung zwischen Ionen und kalten Atomen. Master's thesis, Albert Ludwigs Universität Freiburg, 2011.
- [44] S. S. Kumar, D. Hauser, R. Jindra, T. Best, S. Roucka, W. D. Geppert, T. J. Millar, and R. Wester. Photodetachment as a destruction mechanism for cn^- and c_3n^- anions in circumstellar envelopes. *The Astrophysical Journal*, 776(1):25, 2013. URL <http://iopscience.iop.org/article/10.1088/0004-637X/776/1/25/meta>.
- [45] Wolfgang Ketterle, Kendall B. Davis, Michael A. Joffe, Alex Martin, and David E. Pritchard. High densities of cold atoms in a dark spontaneous-force optical trap. *Phys. Rev. Lett.*, 70, 1993. URL <https://link.aps.org/doi/10.1103/PhysRevLett.70.2253>.
- [46] Lewis M. Branscomb. Photodetachment cross section, electron affinity, and structure of the negative hydroxyl ion. *Phys. Rev.*, 148:11–18, Aug 1966. doi: 10.1103/PhysRev.148.11. URL <http://link.aps.org/doi/10.1103/PhysRev.148.11>.
- [47] T. E. H. Walker, P. M. Dehmer, and J. Berkowitz. Rotational band shapes in photoelectron spectroscopy: Hf and df. *The Journal of Chemical Physics*, 59(8):4292–4298, 1973. doi: <http://dx.doi.org/10.1063/1.1680624>. URL <http://scitation.aip.org/content/aip/journal/jcp/59/8/10.1063/1.1680624>.
- [48] H. Hotop, T. A. Patterson, and W. C. Lineberger. High resolution photodetachment study of oh^- and od^- in the threshold region 7000–6450 Å. *The Journal of Chemical Physics*, 60(5):1806–1812, 1974. doi: <http://dx.doi.org/10.1063/1.1681279>. URL <http://scitation.aip.org/content/aip/journal/jcp/60/5/10.1063/1.1681279>.
- [49] F. Breyer, P. Frey, and H. Hotop. High resolution photoelectron spectrometry of negative ions: Rotational transitions in laser-photodetachment of oh^- , sh^- , sd^- . *Zeitschrift für Physik A Atoms and Nuclei*, 300, 1981. URL <http://dx.doi.org/10.1007/BF01412609>.
- [50] P. A. Schulz, Roy D. Mead, and W. C. Lineberger. Rotational intensities in photodetachment and photoionization. *Phys. Rev. A*, 27:2229–2232,

A Bibliography

- Apr 1983. doi: 10.1103/PhysRevA.27.2229. URL <https://link.aps.org/doi/10.1103/PhysRevA.27.2229>.
- [51] Jim R. Smith, Joseph B. Kim, and W. C. Lineberger. High-resolution threshold photodetachment spectroscopy of oh^- . *Phys. Rev. A*, 55:2036–2043, Mar 1997. doi: 10.1103/PhysRevA.55.2036. URL <http://link.aps.org/doi/10.1103/PhysRevA.55.2036>.
- [52] S. Trippel, J. Mikosch, R. Berhane, R. Otto, M. Weidemüller, and R. Wester. Photodetachment of cold oh^- in a multipole ion trap. *Phys. Rev. Lett.*, 97, 2006. URL <https://link.aps.org/doi/10.1103/PhysRevLett.97.193003>.
- [53] P. Hlavenka, R. Otto, S. Trippel, J. Mikosch, M. Weidemüller, and R. Wester. Absolute photodetachment cross section measurements of the o^- and oh^- anion. *The Journal of Chemical Physics*, art. 061105, 2009. URL <http://scitation.aip.org/content/aip/journal/jcp/130/6/10.1063/1.3080809>.
- [54] Fabienne Goldfarb, Cyril Drag, Walid Chaibi, Sophie Kröger, Christophe Blondel, and Christian Delsart. Photodetachment microscopy of the p, q, and r branches of the $\text{oh}^-(v=0)$ to $\text{oh}^-(v=0)$ detachment threshold. *The Journal of Chemical Physics*, 122, 2005. URL <https://doi.org/10.1063/1.1824904>.
- [55] L. Gonzalez-Sanchez, M. Tacconi, E. Bodo, and F. A. Gianturco. Ionic interactions and collision dynamics in cold traps: rotational quenching of $\text{OH}^- (^1\Sigma^+)$ by $\text{Rb}(2s)$. *The European Physical Journal D*, 49, 2008. URL <https://doi.org/10.1140/epjd/e2008-00148-5>.
- [56] L. González-Sánchez, F. Carelli, F.A. Gianturco, and R. Wester. Computing rotational energy transfers of OD^-/OH^- in collisions with Rb: isotopic effects and inelastic rates at cold ion-trap conditions. *New Journal of Physics*, 17, 2015. URL <http://iopscience.iop.org/article/10.1088/1367-2630/17/12/123003/meta>.
- [57] L. González-Sánchez, F. Carelli, F.A. Gianturco, and R. Wester. Collisional state-changing of OH^- rotations by interaction with Rb atoms in cold traps. *Chemical Physics*, 462, 2015. URL <https://doi.org/10.1016/j.chemphys.2015.05.027>.
- [58] H López, B Höltkemeier, J Glässel, P Weckesser, M Weidemüller, T Best, E Endres, and R Wester. Sympathetic cooling of oh^- ions using ultracold rb atoms in a dark spot. *Ion Traps for Tomorrows Applications*, 189, 2015. URL <https://arxiv.org/abs/1507.06575>.
- [59] Bastian Höltkemeier. Sympathetic cooling of ions in a hybrid atom ion trap. *PHD thesis, Ruprecht Karls Universität Heidelberg*, 2016.

A Bibliography

- [60] Bastian Höltkemeier, Julian Glässel, Henry López-Carrera, and Matthias Weidemüller. A dense gas of laser-cooled atoms for hybrid atom–ion trapping. *Applied Physics B*, 123, 2017. URL <https://doi.org/10.1007/s00340-016-6624-4>.
- [61] Julian Glässel. Saturation absorption imaging of a high-density rubidium dark spot. *Master thesis, Ruprecht Karls Universität Heidelberg*, 2014.
- [62] Annika Tebben. Laser system of a 87-rubidium optical dipole trap. *Bachelor thesis, Ruprecht Karls Universität Heidelberg*, 2015.
- [63] Stefan F. Paul. Optimization of the ion storage in a hybrid atom-ion-trap. *Bachelor thesis, Ruprecht Karls Universität Heidelberg*, 2015.
- [64] Pascal M. Weckesser. Sympathetic cooling of ions in radio frequency traps. *Master thesis, Ruprecht Karls Universität Heidelberg*, 2015.
- [65] Ji Luo. Rotational temperature of ions via photodetachment. *Master thesis, Karlsruhe Institute of Technology*, 2016.
- [66] Gerrit Helge Anders. Photodetachment tomography and spectroscopy of oh- inside a radiofrequency atom-ion-trap. *Bachelor thesis, Ruprecht Karls Universität Heidelberg*, 2016.
- [67] Tobias Heldt. Thermometry of anions in an octupole atom-ion-trap. *Bachelor thesis, Ruprecht Karls Universität Heidelberg*, 2017.
- [68] Nina Beier. A versatile anion source for studying atom-ion collisions. *Bachelor thesis, Ruprecht Karls Universität Heidelberg*, 2017.
- [69] Simone Götz. *A high density target of ultracold atoms and momentum resolved measurements of ion-atom collisions*. PhD thesis, Universität Heidelberg, 2012.
- [70] The nobel prize in Physics 1986. Nobel media ab 2014 web, 2018. URL https://www.nobelprize.org/nobel_prizes/physics/laureates/1989/index.html.
- [71] Hans G. Dehmelt. Experiments with an isolated subatomic particle at rest. *Nobel Media AB 2014*, 1989. URL https://www.nobelprize.org/nobel_prizes/physics/laureates/1989/dehmelt-lecture.pdf.
- [72] Wolfgang Paul. Electromagnetic traps for charged and neutral particles. *Rev. Mod. Phys.*, 62, 1990. URL <https://link.aps.org/doi/10.1103/RevModPhys.62.531>.
- [73] Emile Mathieu. Le mouvement vibratoire d'une membrane de forme elliptique. *Mathématiques pures et appliquées*, 1868. URL http://sites.mathdoc.fr/JMPA/PDF/JMPA_1868_2_13_A8_0.pdf.

A Bibliography

- [74] Dieter Gerlich. Inhomogeneous rf fields: A versatile tool for the study of processes with slow ions. *Advances in Chemical Physics*, 2007. URL <https://onlinelibrary.wiley.com/doi/pdf/10.1002/9780470141397.ch1>.
- [75] David L. Osborn, David J. Leahy, Douglas R. Cyr, and Daniel M. Neumark. Photodissociation spectroscopy and dynamics of the $N_2O_2^-$ anion. *The Journal of Chemical Physics*, 104(13):5026–5039, 1995. doi: <http://dx.doi.org/10.1063/1.471132>. URL <http://scitation.aip.org/content/aip/journal/jcp/104/13/10.1063/1.471132>.
- [76] Christian Greve. Creation of charged water clusters and storage in a bipolar rf multipole ion trap. *Master thesis, Albert Ludwigs Universität Freiburg*, 2009.
- [77] R. Otto, J. Xie, J. Brox, S. Trippel, M. Stei, T. Best, M. R. Siebert, W. L. Hase, and R. Wester. Reaction dynamics of temperature-variable anion water clusters studied with crossed beams and by direct dynamics. *Faraday Discuss.*, 157, 2012. URL <http://dx.doi.org/10.1039/C2FD20013A>.
- [78] WC Wiley and Ii H McLaren. Time-of-flight mass spectrometer with improved resolution. *Review of Scientific Instruments*, 26(12):1150–1157, 1955. URL <https://aip.scitation.org/doi/abs/10.1063/1.1715212>.
- [79] Ronald M. Jones, Dieter Gerlich, and Scott L. Anderson. Simple radio frequency power source for ion guides and ion traps. *Review of Scientific Instruments*, 68, 1997. URL <http://scitation.aip.org/content/aip/journal/rsi/68/9/10.1063/1.1148297>.
- [80] Ronald M. Jones and Scott L. Anderson. Simplified radio-frequency generator for driving ion guides, traps, and other capacitive loads. *Review of Scientific Instruments*, 71, 2000. URL <http://scitation.aip.org/content/aip/journal/rsi/71/11/10.1063/1.1318914>.
- [81] D. Manura and D. Dahl. *Simion 8 Manual*. SIMION (R) 8.0, User Manual (Scientific Instrument Services, Inc. Ringoes, NJ 08551), 2008. URL <http://simion.com/>.
- [82] John Moore, Christopher Davis, and Michael Coplan. *Building Scientific Apparatus*. Cambridge University Press, 2009.
- [83] Steven Chu. Nobel lecture: The manipulation of neutral particles. *Nobel Media AB 2014*, 1997. URL http://www.nobelprize.org/nobel_prizes/physics/laureates/1997/chu-lecture.html.
- [84] Claude Cohen-Tannoudji. Nobel lecture: Manipulating atoms with photons. *Nobel Media AB 2014*, 1997. URL https://www.nobelprize.org/nobel_prizes/physics/laureates/1997/cohen-tannoudji-lecture.html.

A Bibliography

- [85] William D. Phillips. Nobel lecture: Laser cooling and trapping of neutral atoms. *Nobel Media AB 2014*, 1997. URL https://www.nobelprize.org/nobel_prizes/physics/laureates/1997/phillips-lecture.html.
- [86] Wolfgang Ketterle. Nobel lecture: When atoms behave as waves: Bose-einstein condensation and the atom laser. *Nobel Media AB 2001*, 2001. URL http://www.nobelprize.org/nobel_prizes/physics/laureates/1997/chu-lecture.html.
- [87] Bastian Höltkemeier. 2d mot as a source of a cold atom target. *Diploma thesis, Ruprecht Karls Universität Heidelberg*, 2011.
- [88] Daniel A Steck. Rubidium 85 d line data. <http://steck.us/alkalidata/>, 85, 2013. URL <http://steck.us/alkalidata/>.
- [89] WooJin Kwon, Jae-yoon Choi, and Yong-il Shin. Calibration of saturation absorption imaging of ultracold atom clouds. *Journal of the Korean Physical Society*, 61, 2012. URL <http://dx.doi.org/10.3938/jkps.61.1970>.
- [90] G. Reinaudi, T. Lahaye, Z. Wang, and D. Guéry-Odelin. Strong saturation absorption imaging of dense clouds of ultracold atoms. *Opt. Lett.*, 32, 2007. URL <http://ol.osa.org/abstract.cfm?URI=ol-32-21-3143>.
- [91] Lene Vestergaard Hau, B. D. Busch, Chien Liu, Zachary Dutton, Michael M. Burns, and J. A. Golovchenko. Near-resonant spatial images of confined bose-einstein condensates in a 4-dee magnetic bottle. *Phys. Rev. A*, 58, 1998. doi: 10.1103/PhysRevA.58.R54. URL <https://link.aps.org/doi/10.1103/PhysRevA.58.R54>.
- [92] IUPAC. *Compendium of chemical terminology - Gold book*. Blackwell Scientific Publications, Oxford, 2014. URL <https://doi.org/10.1351/goldbook>.
- [93] George Gioumousis and D. P. Stevenson. Reactions of gaseous molecule ions with gaseous molecules. v. theory. *The Journal of Chemical Physics*, 29, 1958. URL <https://doi.org/10.1063/1.1744477>.
- [94] Langevin. Annales de chimie et de physique. *Ann. Chim. Phys*, 5, 1905.
- [95] Fujii T. *Fundamentals of ion Chemistry*. 2015. URL https://doi.org/10.1007/978-1-4899-7588-1_2.
- [96] P. Ausloos and S. Lias. *Structure/Reactivity and Thermochemistry of ions*. 1986.
- [97] Lothar Ratschbacher, Christoph Zipkes, Carlo Sias, and Michael Kohl. Controlling chemical reactions of a single particle. *Nat Phys*, 8, 2012. URL <http://dx.doi.org/10.1038/nphys2373>.

A Bibliography

- [98] Yuan-Pin Chang, Karol Długołęcki, Jochen Küpper, Daniel Rösch, Dieter Wild, and Stefan Willitsch. Specific chemical reactivities of spatially separated 3-aminophenol conformers with cold Ca^+ ions. *Science*, 342, 2013. URL <http://science.sciencemag.org/content/342/6154/98>.
- [99] Tomas Sikorsky, Ziv Meir, Ruti Ben-Shlomi, Nitzan Akerman, and Roei Ozeri. Spin-controlled atom-ion chemistry. *Nature Communications*, 9, 2018. URL <https://www.nature.com/articles/s41467-018-03373-y>.
- [100] D. DeMille. Quantum computation with trapped polar molecules. *Phys. Rev. Lett.*, 88, 2002. URL <https://link.aps.org/doi/10.1103/PhysRevLett.88.067901>.
- [101] Felix H. J. Hall and Stefan Willitsch. Millikelvin reactive collisions between sympathetically cooled molecular ions and laser-cooled atoms in an ion-atom hybrid trap. *Phys. Rev. Lett.*, 109:233202, Dec 2012. doi: 10.1103/PhysRevLett.109.233202. URL <https://link.aps.org/doi/10.1103/PhysRevLett.109.233202>.
- [102] Stefan Schmid, Arne Härter, and Johannes Hecker Denschlag. Dynamics of a cold trapped ion in a bose-einstein condensate. *Phys. Rev. Lett.*, 2010. URL <https://link.aps.org/doi/10.1103/PhysRevLett.105.133202>.
- [103] Christoph Zipkes, Stefan Palzer, Lothar Ratschbacher, Carlo Sias, and Michael Köhl. Cold heteronuclear atom-ion collisions. *Phys. Rev. Lett.*, 105:133201, Sep 2010. doi: 10.1103/PhysRevLett.105.133201. URL <https://link.aps.org/doi/10.1103/PhysRevLett.105.133201>.
- [104] Andrew T. Grier, Marko Cetina, Fedja Oručević, and Vladan Vuletić. Observation of cold collisions between trapped ions and trapped atoms. *Phys. Rev. Lett.*, 102:223201, Jun 2009. doi: 10.1103/PhysRevLett.102.223201. URL <https://link.aps.org/doi/10.1103/PhysRevLett.102.223201>.
- [105] Jason N. Byrd, H. Harvey Michels, John A. Montgomery, and Robin Côté. Associative detachment of rubidium hydroxide. *Phys. Rev. A*, 88:032710, Sep 2013. doi: 10.1103/PhysRevA.88.032710. URL <https://link.aps.org/doi/10.1103/PhysRevA.88.032710>.
- [106] Milaim Kas, Jerome Loreau, Jacques Lievin, and Nathalie Vaeck. Ab initio study of reactive collisions between $\text{Rb}(2s)$ or $\text{Rb}(2p)$ and $\text{OH}^-(^1\sigma^+)$. *The Journal of Chemical Physics*, 144, 2016. URL <http://scitation.aip.org/content/aip/journal/jcp/144/20/10.1063/1.4950784>.
- [107] F. G. Major and H. G. Dehmelt. Exchange-collision technique for the rf spectroscopy of stored ions. *Phys. Rev.*, 170, 1968. URL <https://journals.aps.org/pr/abstract/10.1103/PhysRev.170.91>.

A Bibliography

- [108] I. Rouse and S. Willitsch. Superstatistical energy distributions of an ion in an ultracold buffer gas. *Phys. Rev. Lett.*, 118:143401, Apr 2017. doi: 10.1103/PhysRevLett.118.143401. URL <https://link.aps.org/doi/10.1103/PhysRevLett.118.143401>.
- [109] T. Best, R. Otto, S. Trippel, P. Hlavenka, A. von Zastrow, S. Eisenbach, S. Jezouin, R. Wester, E. Vigr en, M. Hamberg, and W. D. Geppert. Absolute photodetachment cross-section measurements for hydrocarbon chain anions. *The Astrophysical Journal*, 742, 2011. URL <http://stacks.iop.org/0004-637X/742/i=2/a=63>.
- [110] R. Otto, P. Hlavenka, S. Trippel, J. Mikosch, K. Singer, M. Weidem uller, and R. Wester. How can a 22-pole ion trap exhibit ten local minima in the effective potential? *Journal of Physics B: Atomic, Molecular and Optical Physics*, 42(15):154007, 2009. URL <http://stacks.iop.org/0953-4075/42/i=15/a=154007>.
- [111] Sourav Dutta and S. A. Rangwala. Cooling of trapped ions by resonant charge exchange, Apr 2018. URL <https://link.aps.org/doi/10.1103/PhysRevA.97.041401>.
- [112] Ziv Meir, Tomas Sikorsky, Ruti Ben-shlomi, Nitzan Akerman, Yehonatan Dallal, and Roei Ozeri. Dynamics of a ground-state cooled ion colliding with ultracold atoms. *Phys. Rev. Lett.*, 117, 2016. URL <https://link.aps.org/doi/10.1103/PhysRevLett.117.243401>.
- [113] A. K. Hansen, O. O. Versolato, L. Klosowski, S. B. Kristensen, A. Gingell, M. Schwarz, A. Windberger, J. Ullrich, J. R. Crespo L opez-Urrutia, and M. Drewsen. Efficient rotational cooling of coulomb-crystallized molecular ions by a helium buffer gas. *Nature*, 508, 2014. URL <http://dx.doi.org/10.1038/nature12996>.
- [114] E.S. Endres, G. Egger, S. Lee, O. Lakhmanskaya, M. Simpson, and R. Wester. Incomplete rotational cooling in a 22-pole ion trap. *Journal of Molecular Spectroscopy*, 332, 2017. URL <http://www.sciencedirect.com/science/article/pii/S0022285216303629>. Molecular Spectroscopy in Traps.
- [115] Wade G. Rellergert, Scott T. Sullivan, Steven J. Schowalter, Svetlana Kotochigova, Kuang Chen, and Eric R. Hudson. Evidence for sympathetic vibrational cooling of translationally cold molecules. *Nature*, 495(7442): 490–494, March 2013. ISSN 0028-0836. doi: 10.1038/nature11937. URL <http://dx.doi.org/10.1038/nature11937>.
- [116] S. Jyothi, Tridib Ray, Sourav Dutta, A. R. Allouche, Romain Vexiau, Olivier Dulieu, and S. A. Rangwala. Photodissociation of trapped rb_2^+ : Implications for simultaneous trapping of atoms and molecular ions. *Phys. Rev. Lett.*, 117, 2016. URL <https://link.aps.org/doi/10.1103/PhysRevLett.117.213002>.

A Bibliography

- [117] Rico Otto, Alexander von Zastrow, Thorsten Best, and Roland Wester. Internal state thermometry of cold trapped molecular anions. *Physical Chemistry Chemical Physics*, 15(2):612–618, 2013. URL <http://pubs.rsc.org/-/content/articlehtml/2013/cp/c2cp43186f>.
- [118] Wolfgang Demtröder. *Molekülphysik - Theoretische Grundlagen und experimentelle Methoden*. Oldenbourg Verlag Oldenbourg, 2. auflage edition, 2013.
- [119] John M Brown and Alan Carrington. *Rotational spectroscopy of diatomic molecules*. Cambridge University Press, 2003.
- [120] J D Rudmin, L P Ratliff, J N Yukich, and D J Larson. Structure of the photodetachment cross section in a magnetic field: an experiment with oh^- . *Journal of Physics B: Atomic, Molecular and Optical Physics*, 29, 1996. URL <http://stacks.iop.org/0953-4075/29/i=24/a=004>.
- [121] S. Gewurtz, H. Lew, and P. Flainek. The electronic spectrum of hf^+ . *Canadian Journal of Physics*, 53(11):1097–1108, 1975. doi: 10.1139/p75-139. URL <http://dx.doi.org/10.1139/p75-139>.
- [122] J.P. Maillard, J. Chauville, and A.W. Mantz. High-resolution emission spectrum of oh in an oxyacetylene flame. *Journal of Molecular Spectroscopy*, 63(1):120 – 141, 1976. ISSN 0022-2852. doi: [https://doi.org/10.1016/0022-2852\(67\)90139-7](https://doi.org/10.1016/0022-2852(67)90139-7). URL <http://www.sciencedirect.com/science/article/pii/0022285267901397>.
- [123] J.A. Coxon and S.C. Foster. Radial dependence of spin-orbit and λ -doubling parameters in the $x\ 2\ \pi$ ground state of hydroxyl. *Journal of Molecular Spectroscopy*, 91(1):243 – 254, 1982. ISSN 0022-2852. doi: [http://dx.doi.org/10.1016/0022-2852\(82\)90043-1](http://dx.doi.org/10.1016/0022-2852(82)90043-1). URL <http://www.sciencedirect.com/science/article/pii/0022285282900431>.
- [124] Jinchun Xie and Richard N. Zare. Selection rules for the photoionization of diatomic molecules. *The Journal of Chemical Physics*, 93(5):3033–3038, 1990. doi: <http://dx.doi.org/10.1063/1.458837>. URL <http://scitation.aip.org/content/aip/journal/jcp/93/5/10.1063/1.458837>.
- [125] Eugene P. Wigner. On the behavior of cross sections near thresholds. *Phys. Rev.*, 73, 1948. URL <http://link.aps.org/doi/10.1103/PhysRev.73.1002>.
- [126] Thomas F O’Malley. Effect of long-range final-state forces on the negative-ion photodetachment cross section near threshold. *Physical Review*, 137 (6A):A1668, 1965. URL <https://journals.aps.org/pr/abstract/10.1103/PhysRev.137.A1668>.
- [127] Paul C. Engelking. Strong electron-dipole coupling in photodetachment of molecular negative ions: Anomalous rotational thresholds. *Phys. Rev. A*, 26, 1982. URL <http://link.aps.org/doi/10.1103/PhysRevA.26.740>.

A Bibliography

- [128] Bruce K Janousek, Albert H Zimmerman, Kenneth J Reed, and John I Brauman. Electron photodetachment from aliphatic molecular anions. gas-phase electron affinities of methoxyl, tert-butoxyl, and neopentoxyl radicals. *Journal of the American Chemical Society*, 100(19):6142–6148, 1978. URL <https://pubs.acs.org/doi/abs/10.1021/ja00487a030>.
- [129] W. C. Lineberger and Benjamin W. Woodward. High resolution photodetachment of s^- near threshold. *Phys. Rev. Lett.*, 25:424–427, Aug 1970. doi: 10.1103/PhysRevLett.25.424. URL <http://link.aps.org/doi/10.1103/PhysRevLett.25.424>.
- [130] H. Hönl and F. London. Über die intensitäten der bandenlinien. *Zeitschrift für Physik*, 33, 1925. URL <https://doi.org/10.1007/BF01328367>.
- [131] Martin Stei, Johannes Von Vangerow, Rico Otto, Aditya H. Kelkar, Eduardo Carrascosa, Thorsten Best, and Roland Wester. High resolution spatial map imaging of a gaseous target. *The Journal of Chemical Physics*, 138(21):214201, Jul 2013. URL <https://aip.scitation.org/doi/full/10.1063/1.4807482>.
- [132] Milaim Kas, Jerome Loreau, Jacques Lievin, and Nathalie Vaeck. Ab initio study of the neutral and anionic alkali and alkaline earth hydroxides: Electronic structure and prospects for sympathetic cooling of oh-. *The Journal of Chemical Physics*, 146, 2017. URL <https://doi.org/10.1063/1.4983627>.
- [133] Martin Chaplin. Water structure and science, 2018. URL http://www1.lsbu.ac.uk/water/water_structure_science.html.
- [134] Bertrand Guillot. A reappraisal of what we have learnt during three decades of computer simulations on water. *Journal of Molecular Liquids*, 101(1):219 – 260, 2002. ISSN 0167-7322. doi: [https://doi.org/10.1016/S0167-7322\(02\)00094-6](https://doi.org/10.1016/S0167-7322(02)00094-6). URL <http://www.sciencedirect.com/science/article/pii/S0167732202000946>. Molecular Liquids. Water at the New Millenium.
- [135] Janne Savolainen, Saima Ahmed, and Peter Hamm. Two-dimensional raman-terahertz spectroscopy of water. *Proceedings of the National Academy of Sciences*, 110(51):20402–20407, 2013. ISSN 0027-8424. doi: 10.1073/pnas.1317459110. URL <http://www.pnas.org/content/110/51/20402>.
- [136] Keith Johnson. Terahertz vibrational properties of water nanoclusters relevant to biology. *Journal of Biological Physics*, 38, 2011. URL <https://www.ncbi.nlm.nih.gov/pmc/articles/PMC3285730/>.

Acknowledgments

Es war schwierig genug, Wörter zu finden, um diese Dissertation zu schreiben. Es fehlt mir aber noch schwieriger, die richtigen Wörter zu finden, um meine Dankbarkeit zu den Personen auszudrücken, die diese Dissertation ermöglicht haben.

Mein Dank gilt zunächst Herrn Prof. Dr. Matthias Weidemüller, mein Doktorvater. Mathias, es war mir eine Ehre, meine Doktorarbeit in deiner Gruppe schreiben zu dürfen. Ich habe mich damals sehr gefreut, als ich deine Zusage für eine Doktorstelle bei der HAITrap Gruppe bekommen habe! Das Projekt hatte mich bereits damals fasziniert, und das tut es heute noch mehr. Es waren 5 Jahren intensiver Arbeit, die sich gelohnt hat. Ich habe unglaublich viel gelernt und wir haben zusammen ein sehr schönes Projekt nach vorne gebracht. Ich habe unsere zahlreichen Gespräche auf wissenschaftlicher und persönlicher Ebene sehr wertgeschätzt. Vielen Dank für deine ausgezeichnete Betreuung!

Des Weiteren möchte ich mich bei Herrn Prof. Dr. Andreas Wolf für Ihre hilfsbereite Betreuung als Zweitgutachter bedanken. Herr Wolf, Ich habe Ihre wissenschaftliche Arbeit immer sehr bewundert. Insbesondere hat uns Ihre Arbeit zu OH^- sehr geholfen, die Ergebnisse der HAITrap zu interpretieren. Aus dem Grund hat es mich sehr gefreut, dass Sie sich bereit erklärt haben, diese Doktorarbeit zu begutachten. Vielen Dank!

Ferner danke ich Herrn Prof. Roland Wester. Roland, du warst immer bereit, uns bei dem Projekt mit deiner freundlichen Hilfe und Ideengebung zu unterstützen. Es hat mich immer wieder gewundert, wie kreativ du an technischem und wissenschaftlichem Problematiken reagiert hast. Vielen Dank!

An dieser Stelle möchte ich bei mich bei allen meinen Kollegen der HAITrap Gruppe bedanken: Basti, Jonas, Dome, Eric, Jan und Saba, sowie bei allen ehemaligen Studenten die an dieses Projekt beigetragen haben: Mils, Tobi, Nina, Gerrit, Ji, Pascalito, Oktupaul, Annikita und Don Julio. Ich bedanke mich, mit einfachen Wörter aber von tiefsten Herzen, zu euch allen!!! Es ist ein Geschenk des Lebens, so eine Vielfalt an interessante, kluge und gleichzeitig lustige Leute begegnen zu haben. Jeder von Euch weiß ganz genau, wie tief ihr in meinem Herzen gewachsen seid. Danke für eure Rückhalt, Geduld und Hilfsbereitschaft. Danke, dass ihr mit eure Durchsicht und hilfreichen Anregungen mich bei der Bearbeitung meiner Dissertation geholfen habt. Danke, danke, danke!

Ich möchte mich auch bei der Leute in den Werkstätten unseres Instituts be-

A Bibliography

denken. Ich bewundere eure Arbeit. Ich konnte immer bei jedem mechanischen oder elektronischen Problem bei euch eine Lösung finden. Vielen Dank!

Mein ganz besonderer Dank gilt meiner Familie und Freunde. Steffen, ich danke dir besonders für deine Freundschaft und den emotionalen Rückhalt über die Dauer meines gesamten Studiums.

Natalie, danke für dein liebevolles Verständnis und jahrelangen Rückhalt. Du, Heiko und das Baby, das bald kommen wird, sind eine Quelle von Kraft und Mut. Gracias Hermosalie por todo el apoyo que me has dado, no solo este tiempo sino durante todos estos años. Tu sí sabes lo agradecido que estoy contigo! Les amo mucho!

Ich danke meine Eltern Lauro und Cecilia und meine Geschwister Vero und Carlos, die mir mein Studium durch ihre Unterstützung ermöglicht haben. Carlitos, tu has sido una pieza importante para mi desarrollo. Gracias por estar, aun que ausente, siempre presente! Vero y Jan, desde que llegué a Alemania han sido mi base y punto de apoyo. Es obvio que sin ustedes, todo esto habría sido imposible. Gracias por apoyarme incondicionalmente durante todo este tiempo! Mama, tu apoyo, tu cariño y tu dulzura me han inspirado siempre. Eres mi mama pues! Gracias por ser tan linda conmigo y con mi familia! Sobre todo, sin tu ayuda en el último lapso de mi doctorado, esto habría sido imposible. Y para cerrar con broche de oro, Papa! Sin tí nada de esto habría sido posible. Tu me diste la fuerza para empezar este camino, y mira a dónde he llegado. Definitivamente no hay palabras suficientes para agradecerte todo lo que has hecho por mi. Gracias papa!